

Inorganic Salt Nanofibers as Templates for the Formation of Oxide Nanotubes

Von dem Fachbereich Chemie der Universität Hannover

zur Erlangung des Grades einer

DOKTORIN DER NATURWISSENSCHAFTEN

Dr. rer. nat.

genehmigte Dissertation

von

M. Ing. Lirong Ren

Geboren am 07.01.1976, in Shandong, China

2004

Inorganic Salt Nanofibers as Templates for the Formation of Oxide Nanotubes

Thesis
for the degree of Doctor of Science
-Dr. rer. nat.-

Institute of Physical Chemistry and Electrochemistry
University of Hanover

Lirong Ren

Hanover, October 2004

Vorgelegt dem Promotionsausschuß am: 06.10.2004

Tag des öffentlichen Kolloquiums: 17.11.2004

Gutachter der Dissertation: Prof. Dr. Jürgen Caro

Prof. Dr. Peter Behrens

Dedicated to
Prof. Dr. Yan Zhang

Kurzfassung

Unter Ausnutzung von Nanofasern aus einem Tetraamminplatin- oder Hexaammincobalt-salz als strukturdirigierende Strukturen werden SiO_2 und TiO_2 Nanoröhren in einem Sol-Gel-Prozess hergestellt. Zwei Routen für das Wachstum der Nanoröhren werden in dieser Untersuchung angewendet.

In einer generellen Wachstumsroute, d. h. durch Bildung der $[\text{Pt}(\text{NH}_3)_4](\text{HCO}_3)_2$ Nanofasern und anschließendes Beschichtung und Kalzination, werden platinhaltige SiO_2 Nanoröhren mit Größen im Bereich von 100 nm zum 2 μm (Durchmesser) und bis zu 10 μm Länge erhalten. Der innere Querschnitt der Pt-haltigen Nanoröhren ist rechteckig. Die Pt Teilchen bilden sich während der Kalzination bei 500 °C innerhalb der Röhre und in den porösen Wänden der Röhren. Nanodrähte aus Pt werden innerhalb von SiO_2 Nanoröhren mit Durchmessern unter 50 nm beobachtet. Die Synthese von Pt-haltigen TiO_2 Nanoröhren (300 - 400 nm im Durchmesser) ist ebenfalls mit dieser generellen Wachstumsroute möglich. Aufgrund der hoch-dispergierten Pt-Nanoteilchen innerhalb der TiO_2 -Wände kristallisiert das amorphe TiO_2 -Material bei der Kalzination bei 500 °C direkt ohne die Bildung von Anatase zum Rutile. Mit Nanofasern von $[\text{Co}(\text{NH}_3)_6](\text{HCO}_3)(\text{CO}_3)\cdot 2\text{H}_2\text{O}$ als Templat werden uniforme SiO_2 Nanoröhren (100 - 200 nm im Durchmesser), die mit Ketten von Co Nanopartikeln gefüllt sind, erhalten. Der Querschnitt der Co-haltigen Nanoröhren ist rhomboedrisch. Die Co-Nanopartikeln sind in Nanoröhren, deren innere Durchmesser kleiner als 100 nm sind, zu einzelnen Ketten arrangiert.

Bei der kontrollierten Wachstumroute wird das Metallalkoid als Schutzagenz verwendet, um die Aggregation zwischen den einzelnen $[\text{Pt}(\text{NH}_3)_4](\text{HCO}_3)_2$ Nanofasern zu vermeiden. Mit Tetraethylorthosilikat als Schutzschicht werden gleichmäßig dünne (100 - 200 nm) und ultralange (bis zu 40 μm) Pt-haltige SiO_2 Nanoröhren erhalten. Mit Tetrabutylorthotitanat bilden sich Pt-haltige TiO_2 Nanoröhren, die dünner als 100 nm und länger als 6 μm sind. Für diese ist zu erwarten, dass sie elektrische Leitfähigkeitsmessung besser kontaktiert werden können.

Die Elektronenmikroskopie und die Röntgenbeugung sind die hauptsächlichen Werkzeuge, welche für die Probencharakterisierung in dieser Arbeit eingesetzt wurden.

Stichwörter: Oxid-Nanoröhren, Templat, Nanofasern, Sol-gel Prozess

Abstract

Using nanofibers of aminoplatinum or aminocobalt compound as templates, SiO₂ and TiO₂ nanotubes have been prepared in a sol-gel process. Two growth routes were employed in this study.

With the general growth route, i.e. at first the formation of [Pt(NH₃)₄](HCO₃)₂ nanofibers and the subsequent coating and calcination processes, Pt-containing SiO₂ nanotubes in the range of 100 nm – 2 μm in diameter and up to 10 μm in length can be obtained. The cross-sections of the Pt-containing nanotubes are rectangular. The Pt particles formed during the calcination at 500 °C are dispersed within the tube and inside the tube wall. Continuous Pt nanowires are observed inside SiO₂ nanotubes with diameters below 50 nm. The synthesis of Pt-containing TiO₂ nanotubes (300 – 400 nm in diameter) in a high yield have been realized with the general growth route. With the highly dispersed Pt clusters inside the TiO₂ wall, the amorphous TiO₂ crystallized into rutile when calcined at 500 °C without the formation of anatase. Using nanofibers of [Co(NH₃)₆](HCO₃)(CO₃)·2H₂O as templates, uniform SiO₂ nanotubes (100 – 200 nm in diameter) filled with chains of Co nanoparticles were obtained. The cross-sections of the Co-containing nanotubes are rhombohedral. Co nanoparticles are arranged into single chains in nanotubes with inner diameters less than 100 nm.

The controlled growth route was based on the employment of metal alkoxides as capping agents in order to suppress the aggregations of intermediate nanofibers of [Pt(NH₃)₄](HCO₃)₂. With tetraethyl orthosilicate as the capping agent, uniformly thick (100 - 200 nm) and ultralong (up to 40 μm) Pt-containing SiO₂ nanotubes were achieved. By employing tetrabutyl orthotitanate as the capping agent, Pt-containing TiO₂ nanotubes with diameters below 100 nm and lengths above 6 μm have been prepared, which might be better contacted with electrodes for electronic conductivity measurement.

Electron microscopy and X-ray diffraction are main tools for sample characterisation in this work.

Keywords: oxide nanotubes, template, nanofibers, sol-gel process

Acknowledgement

The present work was carried out in sequence at the Institute of Applied and Physical Chemistry, University of Bremen from September 2001 to April 2002, and at the Institute of Physical Chemistry and Electrochemistry, University of Hanover from May 2002 to October 2004.

Firstly of all, I wish to express my deepest gratitude to my supervisor Dr. Michael Wark for his invaluable guidance and support throughout this work. I also wish to thank Prof. Dr. Jürgen Caro for his valuable comments and assistance.

My sincere thanks go to all my dear colleagues at the Institute of Physical Chemistry, University of Hanover. In particular, I wish to thank Dr. Xiaobo Yang for performing the XRD measurements and invaluable comments on the manuscript. I also would like to thank Dr. Armin Feldhoff for his valuable assistance on the electron microscopy. In addition, I would like to thank Kordula Majoni, Kerstin Janze, Yvonne Gabbey and Dipl.-Chem. Alexandra Kleinert for their continuous support and collaboration.

I would like to thank all colleagues at the Institute of Applied and Electrochemistry, University of Bremen, especially Dr. Peter Prochnow, Dipl.-Chem. Yücel Altindag, Karsten Koblitz, Ute Melville, for their precious help to me at the beginning of my PhD study.

I wish to convey my warmest thanks to Dr. Frank Krumeich at ETH, Zürich, for his powerful help on recording the electron micrographs. I wish to thank Dr. Claus H. Rüscher and Dr. Jürgen Köpcke at Institute of Mineralogy, University of Hanover, for their valuable collaboration on the IR, TG and EDXS measurements. My thanks also go to Dr. Jiri Rathousky at Heyrovsky Institute of Physical Chemistry in Prague for the N₂ adsorption measurement.

I would like to express my thanks to Dr. Michael Wiebecke and Dr. Rudolf Wartchow at the Institute of Inorganic Chemistry, University of Hanover, for their cooperation on the crystal structure analyses.

As for the financial support, I am indebted to the Deutsche Forschungsgemeinschaft (DFG).

Finally, my sincerest appreciation goes to my parents and friends for their continuous support and encouragement during my study abroad.

List of Publications

(resulting from this thesis)

1. **L. Ren**, Y. Hou, M. Wark, *One-Dimensional Alignment of Cobalt Nanoparticles inside Silica Nanotubes*, *Advanced Materials*, submitted.
2. **L. Ren**, A. Feldhoff, M. Wark, *Controlled Growth of Pt-containing Silica Nanotubes with High Aspect Ratios*, *Chemistry of Materials*, submitted.
3. F. Krumeich, M. Wark, **L. Ren**, H.-J. Muhr, R. Nesper, *Electron Microscopy Characterization of Silicon Dioxide Nanotubes*, *Zeitschrift für Anorganische und Allgemeine Chemie* **2004**, 630, 1054-1058.
4. J. Zygmunt, F. Krumeich, H.-J. Muhr, R. Nesper, **L. Ren**, M. Wark, *Silica Nanotubes: Template-Assisted Syntheses and Characterisation*, *Zeitschrift für Anorganische und Allgemeine Chemie*, **2002**, 628, 2189.
5. **L. Ren**, U. Melville, M. Wark, *Metal Salts as Structure-directing Agents for SiO₂ and TiO₂ Nanotubes Containing High Amounts of Encapsulated Metal*, *Frontiers of Solid State Chemistry*, World Scientific Publishing Co. Ltd.: Singapore, **2002**, 441.

Abbreviations

AAO	Anodized Aluminum Oxide
BJH	Barrett-Joyner-Halenda
CNT	carbon nanotube
BET	Brunauer-Emmett-Teller
Co salt	$[\text{Co}(\text{NH}_3)_6]\text{HCO}_3\text{CO}_3 \cdot 2\text{H}_2\text{O}$
Co template	Template nanofibers of $[\text{Co}(\text{NH}_3)_6]\text{HCO}_3\text{CO}_3 \cdot 2\text{H}_2\text{O}$
DEG	Diethylene Glycol
DLVO	Derjaguin, Landau, Verwey and Overbeek
DTA	Differential Thermal Analysis
DTG	Derivative Thermogravimetry
EDXS	Energy Dispersive X-ray Spectrometry
HRTEM	High Resolution Transmission Electron Microscopy
IPDS	Imaging Plate Diffractometer System
IR	Infrared
MFs	Micrometer-thick Fibers
NFs	Nanometer-thick Fibers, Nanofibers
NTs	Nanotubes
Pt salt	$[\text{Pt}(\text{NH}_3)_4](\text{HCO}_3)_2$
Pt template	Template nanofibers of $[\text{Pt}(\text{NH}_3)_4](\text{HCO}_3)_2$
PDF	Powder Diffraction File
PVP	Poly(vinyl pyrrolidone)
RT	Room Temperature
SAED	Selected Area Electron Diffraction
SEM	Scanning Electron Microscopy
SFB	Stöber, Fink and Bohn
STEM	Scanning Transmission Electron Microscopy
TBOT	Tetrabutyl Orthotitanate
TEOS	Tetraethyl Orthosilicate
TEM	Transmission Electron Microscopy
TG	Thermogravimetry
1D	One-dimensional

XRD

X-ray Diffraction

0D

Zero-dimensional

Table of contents

1 Introduction	1
2 Crystal growth and sol-gel process	6
2.1 Crystallography	6
2.1.1 Anisotropy	6
2.1.2 Morphology and habit	6
2.1.3 Crystal formation	7
2.1.3.1 Nucleation	8
2.1.3.2 Growth	8
2.1.4 Defects	9
2.2 Sol-gel process	11
2.2.1 Sol-gel precursors	11
2.2.2 Hydrolysis and condensation	12
2.2.3 Influence of reaction conditions	13
2.2.3.1 pH value	13
2.2.3.2 Temperature	13
2.2.3.3 Water/Alkoxide ratio	14
2.2.3.4 Solvent	14
2.2.4 Stability of sols	14
2.2.5 Monodisperse spheres	17
2.2.6 Sol-gel process of transition metal alkoxides	18
2.2.6.1 Low electronegativity	18
2.2.6.2 Unsaturated coordination	18
2.2.6.3 Molecular complexity	19
2.2.6.4 Alkyl chain length	19
3 Experimental	20
3.1 Synthesis	20

3.1.1 Oxide nanotubes with templates of $[\text{Pt}(\text{NH}_3)_4](\text{HCO}_3)_2$	20
3.1.1.1 Chemicals	20
3.1.1.2 SiO_2 nanotubes	20
3.1.1.3 TiO_2 nanotubes	22
3.1.2 SiO_2 nanotubes with templates of $[\text{Co}(\text{NH}_3)_6]\text{HCO}_3(\text{CO}_3)\cdot 2\text{H}_2\text{O}$	24
3.1.2.1 Chemicals	24
3.1.2.2 Preparation of $[\text{Co}(\text{NH}_3)_6]\text{HCO}_3(\text{CO}_3)\cdot 2\text{H}_2\text{O}$	24
3.1.2.3 Synthesis of Co-containing SiO_2 nanotubes	25
3.1.2.4 Factors influencing the morphology of product	25
3.2 Characterization	26
3.2.1 X-ray diffraction	26
3.2.2.1 X-ray powder diffraction	26
3.2.2.2 X-ray single-crystal diffraction	29
3.2.2 Electron Microscopy	30
3.2.2.1 Scanning Electron Microscopy	30
3.2.2.2 Transmission Electron Microscopy	32
3.2.2.3 Scanning Transmission Electron Microscopy	33
3.2.3 Thermogravimetric analysis	34
3.2.4 Infrared spectroscopy	35
3.2.5 N_2 adsorption	36
4 Oxide nanotubes with templates of $[\text{Pt}(\text{NH}_3)_4](\text{HCO}_3)_2$	41
4.1 General growth of oxide nanotubes	41
4.1.1 Pt templates	41
4.1.1.1 Electron Microscopy	42
4.1.1.2 X-ray Diffraction	44
4.1.1.3 Formation of the needle-shaped Pt templates	45
4.1.2 SiO_2 nanotubes	46
4.1.2.1 Electron Microscopy	46

4.1.2.2 X-ray Diffraction	52
4.1.2.3 Thermogravimetric analysis and Infrared spectroscopy	53
4.1.2.4 Coating process	56
4.1.3 TiO ₂ nanotubes	58
4.1.3.1 Microstructures of TiO ₂ nanotubes	58
4.1.3.2 Influences of reaction parameters	61
4.1.3.3 Discussion	64
4.2 Growth mechanism of templates of [Pt(NH ₃) ₄](HCO ₃) ₂	68
4.2.1 Influences of different parameters on the morphology	68
4.2.1.1 Temperature and rate of ethanol addition	68
4.2.1.2 Morphology dependence on the salt concentration in the mother solution	70
4.2.1.3 Bundles of nanofibers observed at ethanol/water of 1:1	72
4.2.2 Discussion of formation mechanism of Pt templates	74
4.3 Controlled growth of Pt-containing oxide nanotubes	77
4.3.1 SiO ₂ nanotubes with high aspect-ratios	77
4.3.1.1 Strategy for the controlled growth	77
4.3.1.2 Monodisperse SiO ₂ nanotubes with high aspect ratios	77
4.3.1.3 Influencing factors on the morphology	83
4.3.1.4 Discussion	85
4.3.2 Controlled growth of TiO ₂ nanotubes with high aspect-ratios	89
4.3.2.1 Morphology	89
4.3.2.2 Discussion	89
4.4 Summary	91
5 Oxide nanotubes with templates of [Co(NH₃)₆](HCO₃)(CO₃)·2H₂O	93
5.1 Preparation of [Co(NH ₃) ₆](HCO ₃)(CO ₃)·2H ₂ O via ion-exchange	93
5.1.1 Single crystal X-ray Diffraction	93
5.1.2 Powder X-ray Diffraction	95

5.2 Co templates	96
5.2.1 Results	96
5.2.2 Discussion	98
5.3 SiO ₂ nanotubes with Co templates	98
5.3.1 X-ray diffraction	99
5.3.2 Electron Microscopy	102
5.3.2.1 Scanning Electron Microscopy	102
5.3.2.2 Transmission Electron Microscopy	103
5.3.2.3 Scanning Transmission Electron Microscopy and Electron Dispersive X-ray Spectroscopy	105
5.3.3 Thermal Analysis	108
5.3.4 Infrared Spectroscopy	109
5.4 Influences of various parameters on the morphology	110
5.4.1 Results	110
5.4.2 Discussions	112
5.5 Summary	113
6 Conclusions and outlook	115
References	117

1 Introduction

The discovery of carbon nanotubes (CNT) by Iijima in 1991 [1] in conjunction with outstanding physical and chemical properties of this kind of novel materials has aroused enormous interests in the scientific community. Up to now immense efforts have been undertaken worldwide to optimize the synthesis, to characterize the structure, and to determine the properties of the CNTs. In addition to multi-walled CNTs, it was also possible to produce single-walled CNTs consisting of only one concentric graphite-type layer by co-vaporizing carbon and transition metals [2-3]. Various potential applications of CNTs have been proposed, for example, as gas detectors [4-5], as field emitters [6-8], as tips for scanning-probe microscopy [9], and as quantum wires [10]. Depending on the method of preparation which controls the degree of graphitization, the helicity and the diameter, CNTs may behave as metallic, insulating or semiconducting nanowires. In addition measurements of Young's modulus show that single nanotubes are stiffer than commercial carbon fibres [11].

Spurred by the wide and highly promising application potentials of CNTs, tubular variants of other materials, also of great interests to scientists, have been created in a variety of chemical compositions and by different manners. Non-carbon nanotubes (NTs) exist from metals, like Au [12] and Te [13], nitrides [14], sulfides [15] and a number of metal oxides, like V_2O_5 , SiO_2 , TiO_2 , ZrO_2 , and MgO . An overview on oxide NTs was recently published by Patzke et al. [16].

SiO_2 NTs have attracted particular attention due to the widespread applications of SiO_2 materials in many fields. Above all, it is well known that SiO_2 materials are extensively employed to support metal catalysts, e.g. Co/SiO_2 catalyst in Fischer-Tropsch synthesis [17-20]. The increased surface area of SiO_2 materials with a tubular structure in the nanometer regime could lead to unpredictable improvements regarding the catalytic effects. Meanwhile biochemically modified SiO_2 nanoparticles have shown excellent enzymatic activities and detection capacities due to their large surface areas for the enzyme immobilization [21]. In addition, strong photoluminescence was observed in SiO_2 NTs, hence applications as light

emitters in optical nanodevices were suggested [22].

SiO₂ NTs have been prepared mainly via a template method combined with the sol-gel technique. Due to the ability of sols to condensate on preformed morphologies, the generated SiO₂ NTs represent replicas of the template structures. For example, silica NTs with tube diameter below 10 nm were created with templates like cylindrical micelles of alkyl ammonium salts [23] or self-assembled fibrillar peptides [24]. In the dimension of 30 - 40 nm, uniform silver nanowires serving as template were homogeneously coated with silica shells [25-26]. Recently, it was proved that a fibrous metal oxide, V₃O₇ • H₂O, could also act as the template to get silica NTs of 50 - 300 nm in diameter [27]. Moreover, the inner walls of a nanoporous anodic aluminum oxide membrane were explored to act as the template to generate pure SiO₂ NTs with adjustable dimensions [22,28-29]. For these above-mentioned methods the templates were necessarily removed to generate hollow and pure silica structures, either by chemical dissolution of the inorganic templates [25-29], or by a simple calcination of the organic ones [23-24].

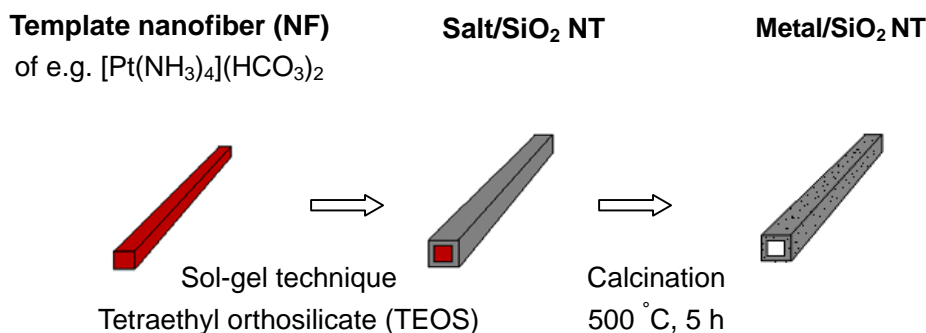
Among the metal oxides used for the formation of hollow fibers, semiconducting TiO₂ is prevalent due to the wealth of its application, e.g., for catalysis [30-32], photocatalysis [33-35], as dye-sensitized solar cells [36], gas-sensors [37]. The nanostructure of a material appears to play a critical role in determining physical properties. For example, compared with a thin film electrode made of titania nanoparticles, a TiO₂ nanowire electrode possesses a twofold higher photocurrent density [38]. The formation of such hollow TiO₂ fibers leads to increased surface areas compared to filled fibers, and hence enhances the effectiveness of the material in a number of applications. For example, a film of TiO₂ nanotubes (22 nm, inner diameter) prepared by anodization exhibits an ultrahigh sensitivity (10⁴, conductivity change) to hydrogen (1000 ppm) [39,40].

TiO₂ NTs can be prepared with varying structures and sizes following different synthesis routes. The most popular synthesis route involves usually the assistance of anodized aluminum oxide (AAO) membranes, either by directly synthesis, i.e. preparing TiO₂ NTs with different titanium precursors in sol-gel process [41-43] or by indirect synthesis, i.e. using a polymer mold as intermediate material and depositing TiO₂ electrochemically [44]. The TiO₂ NTs prepared in this way possess wall thicknesses in the range of 30-50 nm, while their outer diameter depends

on the pore size of the AAO membrane, which is generally in the range of 70-200 nm. Special templates, other than AAO, have been employed in combination with sol-gel methods, like organogel (dibenzo-30-crown-10-appended cholesterol gelator) [45], poly(L-lactide) fibers [46]. As proved several times, the presence of a template is not a prerequisite for the synthesis of TiO₂ NTs. After being treated with NaOH and the subsequent washing with de-ionized water, TiO₂ with anatase or rutile structure was converted to a tubular structure with multiple shells, characterizing a much smaller size: 9 - 10 nm in diameter and 50 - 200 nm in length [47-49]. Another important synthesis route is the anodic oxidation of titanium in analogy to the way to prepare an AAO membrane [39]. In these cases, the TiO₂ NTs up to some 10 μm long and exhibiting outer diameters of 100 - 200 nm have been formed while the actual wall thickness depends on the synthesis conditions applied.

Another fascinating aspect of NTs are the interior cavities, which could be used to incorporate metals for applications, e.g. in catalysis, as nanosensors, in separation. The procedures to fill nanotubes may be classified in three groups: (a) filling of pre-synthesized nanotubes by a wet-chemical method, which leads selectively to a decoration of the internal surface [50], (b) the physical method, where capillarity forces induce the filling of a molten material [51-52], and (c) evaporation by arc discharge in an inert atmosphere [53]. In addition, it is noteworthy to mention that Ga-filled MgO single crystalline NT was prepared by a liquid metal-assisted route and was suggested for application as wide-range nanothermometer [54].

Several years ago, an alternative metal-salt-nanofiber template method was firstly established in our group to form SiO₂ and TiO₂ NTs [55-58]. One typical synthetic procedure is drawn in Scheme 1.1. At first template nanofibers (NFs) of amino-metal compounds, e.g. [Pt(NH₃)₄](HCO₃)₂, are prepared by solvent modification. Afterwards those NFs are coated with tetraethyl orthosilicate (TEOS). The subsequent calcination at 500 °C reduces the metal ions to metal clusters, which enter the porous walls of the NTs. In case of a Pt salt to TEOS or tetrabutyl orthotitanate (TBOT) ratio of 1:5, which is the optimum to obtain exclusively NTs, a Pt content of 40 wt.% in the tubes is obtained. In general, the obtained NTs mostly show close ends, although in Scheme 1.1 an open NT was drawn for clarity.



Scheme 1.1 Illustration of the synthetic procedure of metal-filled SiO_2 NTs by use of metal-salt-NF template method

Compared with other studies mentioned above, this novel metal-salt-NF template method is advantageous since it realizes the filling of metals as well as the fabrication of NTs simultaneously in an elegant and sufficient way. The easily achievable high amount of metal filling can provide many potential applications to the oxide NTs. For the thus-synthesized silica NTs, gas adsorption and catalytic properties different from those of ordinarily supported Pt- SiO_2 catalysts prepared by aqueous impregnation method [59] are expected, since a large amount of Pt particles are free-standing inside the tubes and, thus, more accessible to the reactants. For thus-synthesized titania NTs [55] the doping by Pt metals could improve the conductivity of semiconductor titania, rendering this kind of NTs potential application as nanoelectronics. Besides, it is well known that Pt-doped TiO_2 often shows a high photocatalytic activity for various oxidation processes [60-63]. It is suggested that, on the one hand, platinum deposited on TiO_2 could trap photo-generated electrons and subsequently increase the photo-induced electron transfer rate at the interface. Furthermore, the Pt particles could also provide catalytic sites where mechanistic pathways different from those on naked TiO_2 are enabled [60,61,63]. A promising observation with respect to anisotropic electric conductivity is the formation of continuous Pt nanowires inside the thus-synthesized silica NTs, which mostly is found in very thin NTs [64]. Recently, this template method was also applied to synthesize alumina and silica-alumina NTs filled with Pt particles, the latter may exhibit characteristic acidic properties [65].

However, based on this metal-salt-NF template method, only Pt-filled SiO₂ NTs have been repetitively produced, which still show a broad size distribution of 0.1 - 2 μm in diameter. For preparation of TiO₂ NTs, it was difficult to repeat even the only one successful batch, the productivity of which was actually very low.

In this dissertation, great efforts were made to prepare SiO₂ and TiO₂ NTs with monodispersity and high aspect ratio by this template method. In addition to the Pt salt, i.e. [Pt(NH₃)₄](HCO₃)₂, further metal salts were explored for one-dimensional growth and to act as templates for the NT formation. Characterizations of the samples were made mainly by Scanning Electron Microscopy (SEM), Transmission Electron Microscopy (TEM), X-ray Diffraction (XRD), Thermogravimetric Analysis (TGA) and Infrared (IR) spectroscopy.

2 Crystal growth and sol-gel process

This chapter is divided into two parts, (i) fundamentals of crystallography and (ii) sol-gel process respectively.

2.1 Crystallography

At first several terms in the field of crystallography are introduced, including anisotropy, morphology and habit. Then crystal growth is described in detail in combination with growth rates of different types of faces. At last defects as an important part of crystallography are simply described, especially screw dislocations.

2.1.1 Anisotropy

A crystal is a three-dimensional periodic ordering of atoms, ions or molecules. There are seven crystal systems: triclinic, monoclinic, orthorhombic, tetragonal, trigonal, hexagonal and cubic. If different values of a physical property are observed in different directions, this phenomenon is called anisotropy [1]. Except the isotropic cubic crystals, anisotropy is characteristic of all other crystal systems.

2.1.2 Morphology and habit

Morphology is the study of the external boundary of a crystal, built up of crystal faces and edges [1]. The abundance of characteristic faces and, at least in ideal circumstances, the regular geometric forms (morphology) displayed externally by crystals result from the fact that crystals internally possess a crystal structure. The relationship between crystal structure and morphology may be summarized as: a) Every crystal face lies parallel to a set of lattice planes; parallel crystal faces correspond to the same set of planes; b) Every crystal edge is parallel to a set of lattice lines.

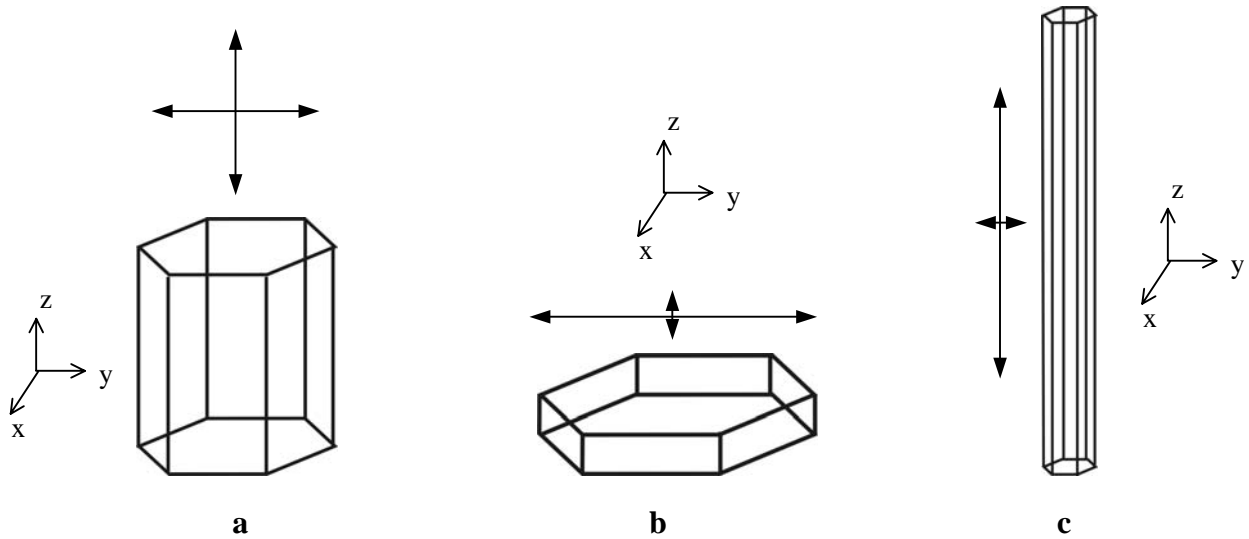


Figure 2.1 The three basic habits: a) equant, b) planar or tabular, c) prismatic or acicular with the relative growth rates in different directions shown by arrows [1].

In morphology, the term “habit” is especially used to describe the relative sizes of the faces of a crystal. There are three fundamental types of habit: equant, planar or tabular, and prismatic or acicular (needle-shaped) as shown in Figure 2.1. The three basic types of crystal habit may be understood in terms of the relative growth rates of the prism (z direction) and pinacoid faces (x or y direction).

The morphology of a crystal can be interpreted from a thermodynamic point of view. The work spent to create reversibly and isothermally a unit area of a new surface is called specific surface free energy [2]. The more closely packed the given crystal face, the smaller is the density of the unsaturated bonds and thus its specific surface free energy. When considering the equilibrium of a crystal with its ambient phase (vapor, solution or melt), there exists obviously a morphology which is the most favorable in the sense that the surface energy of such a crystal is the minimal one at the given crystal volume.

2.1.3 Crystal formation

It is easier to understand the morphology of a crystal if the formation and growth of crystals are considered. Crystals grow from supersaturated solutions, supercooled melts and vapors. The

formation of a crystal may be considered in two steps.

2.1.3.1 Nucleation

Nucleation is the congregation of a few atoms to form a three-dimensional periodic array, called nucleus, which already shows faces, although it is only a few unit cells in size [1].

The classical theory of nucleation is also called the fluctuation theory of nucleation. In a homogeneous molecular system, there are two kinds of local density deviations from the normal state, called homophase and heterophase fluctuations [2]. Homophase fluctuations reflect the density deviations in the given phase. Due to the small sizes of clusters formed in this kind of density deviations, the chemical potential of the new phase is larger than that of the bulk phase, so the clusters are “lifeless”. Instead, heterophase fluctuations would lead to a visible transition to another phase. For these fluctuations to happen, the sizes of the clusters must exceed a critical value. In other words, the system should overcome an activation barrier whose height is given by the work of formation of the critical nuclei.

2.1.3.2 Growth

The process of growth of crystals takes place at the crystal-ambient phase interface where the latter can be a vapor, melt or solution. Obviously, the equilibrium structure of this interface, or in other words its roughness, determines the crystal shape on one hand and the mechanism of growth and in turn its rate of growth on the other [1].

The growth of the nucleus, and then of the crystal, is characterized by a parallel displacement of its faces, called the rate of crystal growth [1]. Generally, the crystal faces are divided into three groups: flat (F), stepped (S) and kinked (K) surfaces depending on whether they are parallel to at least two densest rows of atoms, one densest row of atoms or are not parallel to any densest rows of atoms at all, respectively [2]. As shown in Figure 2.2, typical examples of F, S and K faces are in turn the (100), (110) and (111) faces of NaCl crystal. For a kinked face that intersects all densest rows of atoms and offers kink sites with much higher density than flat and stepped faces, the number of the unsaturated bonds reaches its highest value and so is the specific surface free energy of the face. Therefore, the kinked face will grow faster

than the latter. Then at a supersaturation state small enough to prevent 2D nucleation, the rate of growth in a direction normal to the particular faces will be highest for the kinked faces, smaller for the stepped faces and zero for the flat faces. It follows that the kinked faces should disappear first, followed by the stepped faces and finally the crystal will be enclosed during growth by the flat faces only and will cease to grow at all at a supersaturation small enough.

In conclusion, the actual crystal faces which eventually enclose the crystal depend on the ratios of the growth rates of the various faces, the slower-growing ones becoming more prominent than those that grow more rapidly. Those faces, which do eventually develop, generally have low Miller indices (flat faces) and are often densely populated with atoms [1].

In addition, it should also be noted that the rate of crystal growth is a characteristic, anisotropic property of a crystal, affected by temperature, pressure, and degree of saturation of the solution [1].

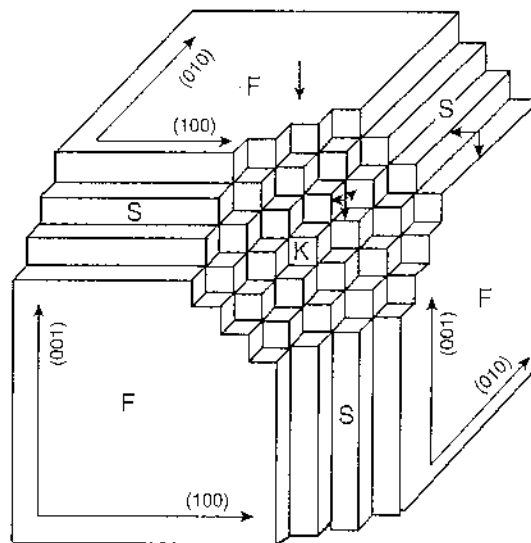


Figure 2.2 A schematic representation of a NaCl crystal illustrating F, S and K faces. The long arrows give the directions of the densest rows of atoms or the directions of the first neighbor bonds [2].

2.1.4 Defects

According to their dimensionality, individual defects can be categorized to point, line and plane

defects. The type of line defect forms along a line, the line of dislocation. One type of line defects is called screw dislocation. In the region of the line of dislocation, the crystal does not consist of neatly stacked lattice planes, but of an arrangement of atoms that repeat through the structure in a helical manner (screw dislocation).

Screw dislocations play an important role in crystal growth. The deposition of atoms on a step of the helix is always energetically favorable, and these steps persist during the growth of the crystal, permanently. As shown in Figure 2.3, a growth hillock is formed. Whiskers or ultrathin needle crystals often form with the screw dislocation parallel to the needle axis. They display remarkable mechanical properties. For example, the breaking strength of a NaCl-whisker of $1\ \mu\text{m}$ diameter is as high as $110\ \text{kPmm}^{-2}$.

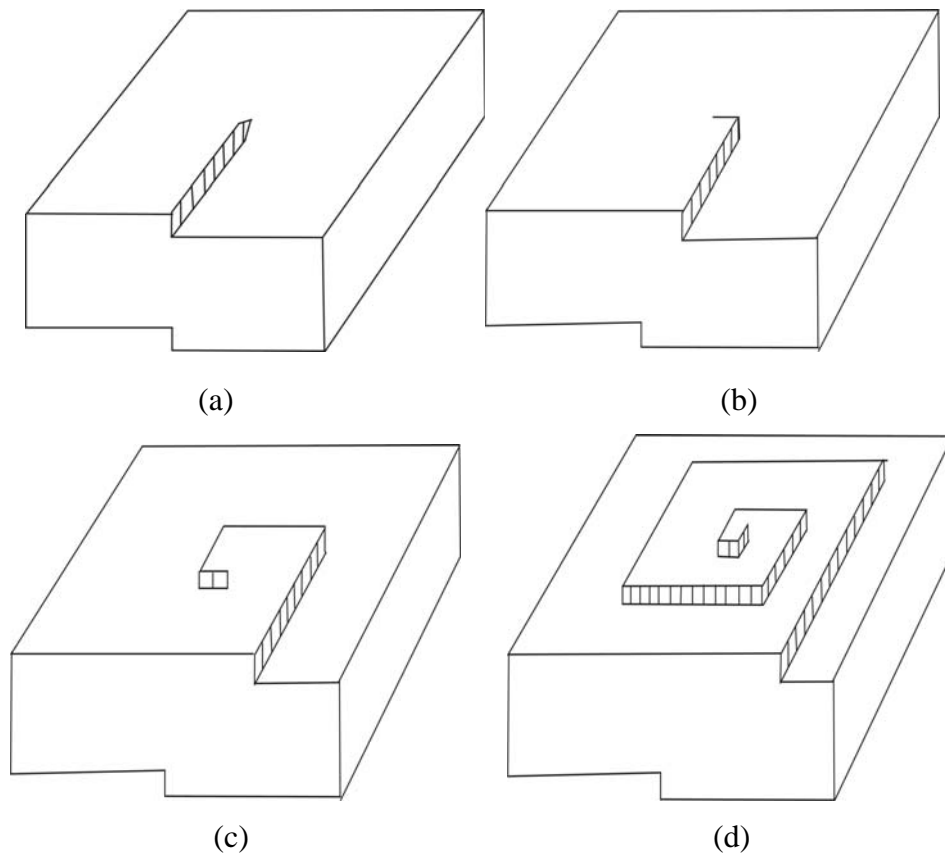


Figure 2.3 Consecutive stages from (a) to (d) of the formation of a growth pyramid around an emergency point of a single screw dislocation. The side faces of such pyramids represent in fact vicinal surfaces. Their slopes are proportional to the supersaturation [2].

At the end of the introduction of crystallography, several points can be emphasized here that the growth of needle-shaped crystal could be explained either by the minimum surface free energy of crystal faces from the thermodynamic view, or by the relative rate of growth of different crystal faces from the kinetics. The amino-metallic compounds employed as templates for the growth of nanotubes must have a habit to grow into needles with a thickness in the nanometer regime. In addition, screw dislocation should greatly contribute to the one-dimensional growth of the templates that were used in this study.

2.2 Sol-gel process

Sol-gel derived materials may be advantageous over materials by other preparation methods. For the preparation of catalysts, for example, they offer a unique means of producing high surface area materials that are otherwise unattainable from conventional ceramic processing methods at high temperature [3,4].

In sections 2.2.1 to 2.2.3, a general overview about sol-gel process is given by introducing the sol-gel precursors, the reactions of precursors, and the influences of different reaction conditions. Afterwards, two important aspects in the sol-gel chemistry, also relevant to the present work, are covered, including the stability of sols in section 2.2.4 and the production of SiO₂ spheres in section 2.2.5. At last, section 2.2.6 is especially dedicated to the sol-gel process of transition metal precursors, which is important for the synthesis of TiO₂ nanotubes.

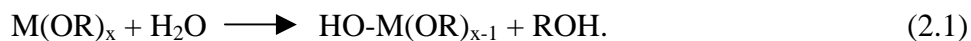
2.2.1 Sol-gel precursors

Metal alkoxides, M(OR)_x, are popular precursors in the sol-gel process. The most thoroughly studied example is tetraethyl orthosilicate (TEOS), Si(OC₂H₅)₄, which was also employed as the precursor of SiO₂ in this study. The sol-gel process for the synthesis of metal oxides from metal alkoxide precursors is composed of five stages: precursor reaction solution, sol or gel formation, aging, drying and sintering. The first step in the process means hydrolysis and condensation of precursors.

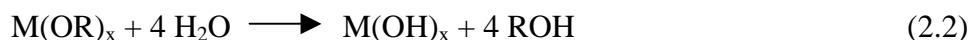
The ligands or groups bound to the metal will change the reactivity of the species during the hydrolysis and condensation. The general trend for the hydrolysis of metal alkoxides is that larger and more extensively branched R groups give slower hydrolysis (or condensation) rates [5]. Based on this reason, tetrabutyl orthotitanate (TBOT), $\text{Ti}(\text{OBu})_4$, was used as the precursor of TiO_2 in this study, instead of $\text{Ti}(\text{OEt})_4$.

2.2.2 Hydrolysis and condensation

The hydrolysis of metal alkoxides occurs by the nucleophilic attack of the oxygen in a water molecule on the M atom in both acid- and base-catalyzed systems [5]:

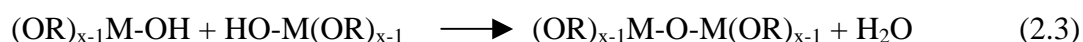


Depending on the amount of water and the catalyst present, hydrolysis may go to completion,

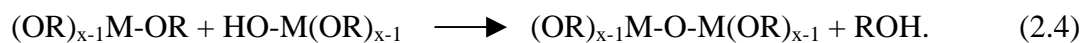


or stop while the metal is only partially hydrolyzed, $\text{M}(\text{OR})_{4-n}(\text{OH})_n$.

Two hydrolyzed monomers can link together to form a dimer in a condensation reaction eliminating a water molecule,



or one hydrolyzed monomer can react with an alkoxide group from another monomer eliminating an alcohol,



After a dimer is formed, it hydrolyzes more easily than the monomer and thus the rate of condensation between the dimer and monomer is faster than the condensation between monomers. Hence, the growth of these materials occurs preferentially by the addition of monomers to oligomers,



In this manner a three-dimensional network of $-\text{M-O-M}-$ is formed, with the degree of polymerization and rate of growth controlled by reaction conditions (section 2.2.3).

In our study, $\text{M} = \text{Ti}$ or Si , $x = 4$ and $\text{R} = -\text{CH}_2\text{CH}_2\text{CH}_2\text{CH}_3$ for Ti , or $-\text{CH}_2\text{CH}_3$ for Si .

2.2.3 Influence of reaction conditions

The rates of hydrolysis and condensation of metal alkoxides in the sol-gel process are influenced by a range of reaction conditions, including pH value, temperature, water/alkoxide ratio and solvent.

2.2.3.1 pH value

Above pH 7, condensation occurs preferentially between weakly acidic species that tend to be protonated (monomers) and strongly acidic species that are deprotonated (clusters). Therefore growth occurs primarily by monomer-cluster aggregation. The acidity of a silanol depends on the other substituents on the silicon atom. When basic OR and OH are replaced with OSi, the reduced electron density on Si increases the acidity of the protons on the remaining silanols [6].

Since dissolution and redistribution reactions provide a source of monomers required for reaction-limited monomer-cluster growth, the polymerization process is equivalent to nucleation and growth, and leads to compact and nonfractal near-equilibrium structures [5]. This process is also called Ostwald ripening, i.e. particles grow by the dissolution of smaller particles and deposition of soluble silica on larger particles.

Below pH 7, the rate of hydrolysis increases and the rates of condensation and dissolution decrease. The predominant growth mechanism changes from monomer-cluster to cluster-cluster with decreasing pH and increasing time of reaction. Consequently, weakly branched structures predominate in the final particles.

In this study, the sol-gel processes were carried out under basic conditions (pH = 8 - 9) so that the basic aminometallic compounds were stable. Therefore, the growth of particles could follow the rules of Ostwald ripening.

2.2.3.2 Temperature

When temperature increases, both the rates of hydrolysis and condensation increase, leading to a decrease of the gelation time. In addition, due to the greater solubility of silica at higher temperatures, larger sizes of particles form especially during the Ostwald ripening process above pH 7, whereby particles grow in size and decrease in their number since highly soluble small particles dissolve and reprecipitate on larger, less soluble nuclei [5].

For the synthesis of TiO₂ NTs, temperature must be drastically reduced in order to retard the rates of hydrolysis and condensation of TBOT, while it is not critical for TEOS due to its much slower rates. The comparison between the reaction rates of TEOS and TBOT will be further elaborated in section 2.2.6.

2.2.3.3 Water/alkoxide ratio

Increasing the value of water/alkoxide ratio r causes an increase in the hydrolysis and dissolution rates, both of which promote the formation of more compact structures. There is also a general trend: acid-catalyzed hydrolysis with low H₂O:Si ratios (< 4) produces weakly branched “polymeric” sols, whereas base-catalyzed hydrolysis with a large r (> 20) produces highly condensed “particulate” sols. Intermediate conditions produce structures intermediate to these extremes [5].

In the designed base-catalyzed reaction system of this study, the water/alkoxide ratio was rather high (> 100), therefore, highly condensed sols were produced.

2.2.3.4 Solvent

In the sol-gel process solvents are added traditionally to prevent liquid-liquid phase separation between water and the metal alkoxide at the initial stages of the hydrolysis reaction. In addition, by controlling the concentrations of silicate and water, solvents can also influence the gelation kinetics.

Solvents can be classified as polar or nonpolar and as protic or aprotic according to their solvating power. The nucleophilicity of anion and electrophilicity of cation can be influenced by the solvating power of solvents. For example, protic solvent molecules that form hydrogen bonds with hydroxyl ions at base-catalyzed conditions reduce the catalytic activity and, consequently, retard both hydrolysis and condensation. Moreover, polar solvents (e.g. water or alcohol) are normally used to solvate polar silicate species used in the sol-gel process [5].

Being a protic and polar solvent, ethanol is chosen as the solvent for our reaction system.

2.2.4 Stability of sols

The stability and flocculation of sols is the most extensively studied aspect of colloidal chemistry.

The flocculation of dispersions is a consequence of attractive forces holding particles together when they collide. If the particles repel each other sufficiently and if they are small enough, they bounce apart on collision, and the dispersion is stable.

An outstanding theory to explain the mechanisms of stability of sols was formulated by Derjaguin, Landau, Verwey and Overbeek and is now denoted by the acronym “DLVO” theory. The basic idea of the theory is that the stability of a dispersion is determined by the sum of attractive and repulsive forces between individual particles. The mutual attraction of particles is a consequence of the dispersion forces, often called London-van der Waals forces, and the mutual repulsion of particles is a consequence of the interaction of the electrical double layers surrounding each particle [7]. The London-van der Waals forces result from transitory dipole-transitory dipole interactions, which produce the long-range attraction between colloidal particles. The double layer is illustrated schematically in Figure 2.4. In the Stern layer, the potential drops linearly through the tightly bound layer of water and counterions. Beyond the Helmholtz plane or in the Gouy layer, the counterions diffuse freely. In DLVO theory, the repulsive barrier depends on two types of ions that construct the double layer: charge-determining ions that control the charge on the surface of the particle and counterions that are in solution in the vicinity of the particle and act to screen the charges of the potential determining ions.

According to DLVO theory, as the concentration of counterions increases till a certain value, the double-layer repulsion is reduced to the point that the net interparticle potential is attractive and the colloid will coagulate immediately. The stability of the colloid correlates closely with the magnitude of the zeta-potential which is defined as the potential of the slip plane that separates the region of fluid that moves with the particle from the region that flows freely. Roughly speaking, stability requires a repulsive potential $\geq 30 - 50$ mV.

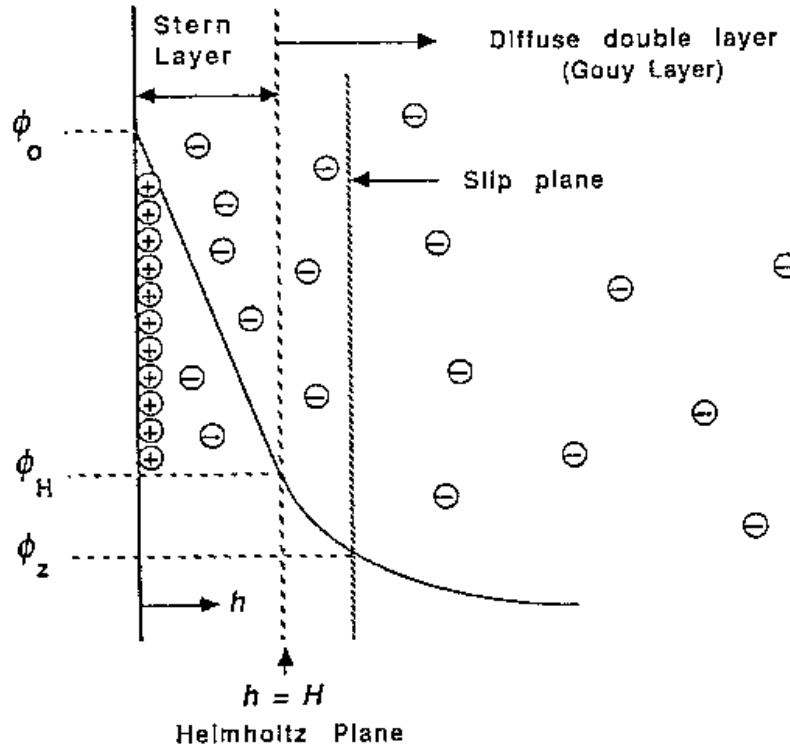
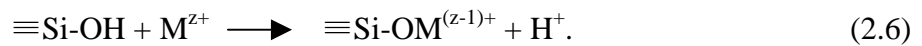


Figure 2.4 Electrical double layer [5].

The DLVO theory can successfully explain the stabilities of most of the sols including that of titania. In the case of silica sol, however, its stability does not conform to the DLVO theory, since it is apparently stabilized by a layer of adsorbed water that prevents coagulation even at the isoelectric point (the pH at which zeta-potential is 0. For silica, it is within pH 1.5 - 4.5, depending on the extent of condensation of the silicate species). To destabilize an aqueous silica sol, it is necessary to reduce the degree of hydration, for example, by adding salt to the sol to undergo ion exchange between an unhydrolyzed cation of M^{z+} and the hydrated SiOH,



So the removal of hydrated SiOH decreases the stability of the colloid [8]. That is also the mechanism responsible for the coating process of SiO_2 on the nanofibers of aminometallic compounds.

2.2.5 Monodisperse spheres

For preparations of monodisperse silica spheres, a widely used method was developed by Stöber, Fink and Bohn (SFB) [9]: alcohol, ammonia, and water are mixed, then TEOS is added, resulting in visible opalescence within ca. 10 minutes. The ratio of water to TEOS, r , is typically more than 20, and the pH is very high. Both of these factors promote condensation and favor the formation of compact structures. A general trend for preparation of SFB spheres is that smaller particles and narrower size distributions are obtained with smaller alcohols as solvent.

The mechanism for the growth of monodisperse particles is generally explained by the theory of LaMer and Dinegar [10] as illustrated in Figure 2.5. At first, the supersaturation of the hydrous oxide, $\text{Si}(\text{OH})_4$, is increased continuously till the critical concentration of nucleation, c_N , is reached. During the extremely rapid nucleation process, the precipitation of particles reduces the supersaturation below the point c_0 , where further nucleation is unlikely. At last, on the existing nuclei the growth continues until the concentration is reduced to the equilibrium solubility, c_s . According to this theory, a single particle size can be achieved if the nucleation happens in a single burst of nuclei, whereas a range of sizes results if new nuclei form during the growth period.

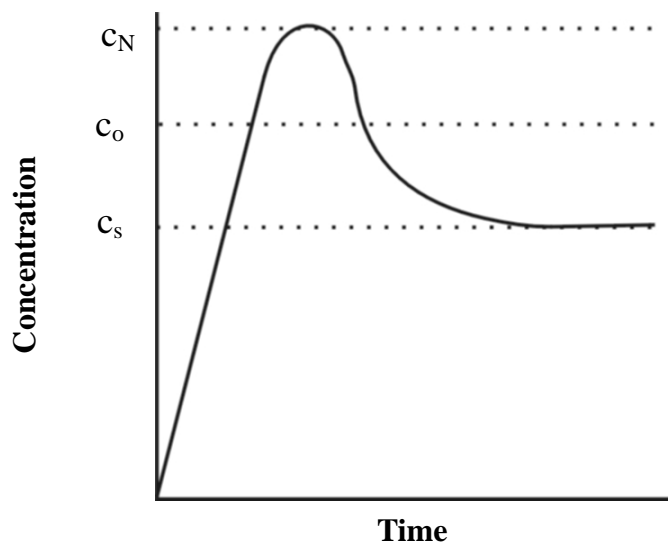


Figure 2.5 Illustration of concentration of precipitating species before and after nucleation [10].

2.2.6 Sol-gel process of transition metal alkoxides

Transition metal alkoxides, $M(OR)_z$, especially those of the d^0 transition metals (Ti, Zr), are widely used as molecular precursors for glasses and ceramics. Several factors distinguish transition metal alkoxides from silicon alkoxides ($Si(OR)_4$), the most commonly used precursors in sol-gel process.

2.2.6.1 Low electronegativity

Compared with silicon, the lower electronegativity of transition metals (Si 1.7, Ti 1.3, Zr 1.7) causes them to be more electrophilic and thus less stable toward hydrolysis, condensation, and other nucleophilic reactions [11]. Values of positive partial charge, $\delta(M)$, of several transition metal alkoxides are listed in Table 2.1 where they are compared to $\delta(Si)$. It is apparent that the values of $\delta(M)$ in all these transition metal alkoxides are higher than $\delta(Si)$.

At pH 7, a rough estimate of the minimum hydrolysis rate constant for $Ti(OR)_4$ is $k_h = 10^{-3} M^{-1}s^{-1}$ [12], more than five orders of magnitude larger than that for $Si(OR)_4$. The situation of condensation rates is similar, with $k_c(Si(OEt)_4) = 10^{-4} M^{-1}s^{-1}$ [13] and $k_c(Ti(OEt)_4) = 30 M^{-1}s^{-1}$ [14].

Table 2.1 Positive partial charge $\delta(M)$ for metals in various alkoxides [11]

Alkoxide	Zr(OEt) ₄	Ti(OEt) ₄	Nb(OEt) ₅	Ta(OEt) ₅	VO(OEt) ₃	W(OEt) ₆	Si(OEt) ₄
$\delta(M)$	+0.65	+0.63	+0.53	+0.49	+0.46	+0.43	+0.32

2.2.6.2 Unsaturated coordination

Transition metals often exhibit several stable coordinations. When coordinatively unsaturated, they tend to expand their coordination via olation, oxolation, alkoxy bridging, or other nucleophilic association mechanisms [11]. For example, transition metal alkoxides dissolved in nonpolar solvents often form oligomers via alkoxy bridging. In polar solvents such as alcohol, either alkoxy bridging or alcohol association can occur. In comparison, for $Si(OR)_4$ with a saturated coordination, neither oligomerization nor alcohol association is observed.

2.2.6.3 Molecular complexity

Another factor that influences reaction kinetics is the extent of oligomerization (molecular complexity) of the metal alkoxides. The molecular complexity increases with the atomic size of the metal within a particular group. Moreover it also depends on the alkoxide ligand: for example, $\text{Ti}(\text{OEt})_4$ exhibits an oligomeric structure, whereas $\text{Ti}(\text{OPr}^i)_4$ remains monomeric [15].

The influence of molecular complexity on the hydrolysis kinetics can be reflected from the solvent effect: $\text{Ti}(\text{OEt})_4$ dissolved in EtOH exhibits an oligomeric structure, and hydrolysis results in precipitation of monosized particles. $\text{Ti}(\text{OPr}^i)_4$ dissolved in Pr^iOH is monomeric and hydrolysis results in rapid precipitation of a polydisperse product [15]. Therefore, starting from a particular alkoxide, the kinetics and resulting structure can be controlled by appropriate choice of solvent [11].

2.2.6.4 Alkyl chain length

The size and electron-providing or -withdrawing characteristics of the organic ligand also affect the hydrolysis and condensation kinetics [5]. For a series of titanium n-alkoxides, the hydrolysis rate decreases with the alkyl chain length [12], consistent with the steric effect expected for an associative S_N reaction mechanism. In addition, Livage et al. show a trend of decreasing δ (Ti) with alkyl chain length that should also contribute to slower kinetics [11].

Concerning the synthesis of TiO_2 nanotubes by sol-gel process in this study, TBOT is employed as the precursor due to its long alkyl chain length. Nevertheless, the low electronegativity and unsaturated coordination of Ti atom in the alkoxide still result in a high reactivity, which requires that it has to be handled with strict control of moisture and conditions of hydrolysis and condensation in order to prepare homogeneous sols or gels rather than precipitates.

3 Experimental

In section 3.1, the synthetic processes of a variety of oxide NTs filled with metal nanoparticles, mainly involving SiO₂ NT filled with Pt, TiO₂ NT filled with Pt and SiO₂ NT filled with metallic Co, are described in sequence. The corresponding methods of characterization are introduced in section 3.2.

3.1 Synthesis

3.1.1 Oxide nanotubes with templates of [Pt(NH₃)₄](HCO₃)₂

Using [Pt(NH₃)₄](HCO₃)₂ as structure-directing agent for sols of metal alkoxides, including tetraethyl orthosilicate (TEOS) and tetrabutyl orthotitanate (TBOT), oxide NTs have been prepared. Two synthesis routes were employed and correspondingly nanotubes with two different appearances were produced.

3.1.1.1 Chemicals

[Pt(NH₃)₄](HCO₃)₂ (Chempur)

Tetraethyl orthosilicate (TEOS, > 98%, p.a., Merck)

Tetrabutyl orthotitanate (TBOT, p.a., Merck)

Diethyleneglycol (DEG)

Ammonia solution (concentrated) (p.a., Merck)

Ammonia solutions (20 °C, pH values: 10, 10.40 and 10.64) (preparation: take 1 mL, 3 mL and 7.5 mL concentrated ammonia separately and dilute them to 100 mL with distilled water)

3.1.1.2 SiO₂ nanotubes

a) General growth of SiO₂ nanotubes

In a typical experiment 10 mL ethanol were dropped into a solution (called mother liquid) of 0.0049 g (0.0125 mmol) [Pt(NH₃)₄](HCO₃)₂ dissolved in 1 mL ammonia solution (20 °C, pH 10).

Along with the adding of ethanol, the mother liquid turned from a transparent colourless solution to a white cloudy suspension containing $[\text{Pt}(\text{NH}_3)_4](\text{HCO}_3)_2$ fibers, to which 14 μL TEOS (optimised molar ratio of template:TEOS = 1:5) were added. During the whole process the system was kept under vigorous stirring of 300 rpm. The reaction was completed after stirring for 12 h and then the product of template-filled silica NTs was achieved. After being dried mostly in air and collected for calcination at 773 K (heating rate: 5 K/min) for 5 h in air, the product was converted to metal-filled silica NTs.

b) Study on the formation mechanism of Pt templates

In order to study the formation mechanism of template fibers of $[\text{Pt}(\text{NH}_3)_4](\text{HCO}_3)_2$, variations of different parameters, including temperature, rate of ethanol addition, Pt concentration in the mother liquid and ratio of ethanol to water were carried out according to the following Table 3.1. The ammonia solution used in this study has a pH value of 10.

Table 3.1 Experimental parameters of the study on the formation mechanism of the Pt templates

Temperature	Rates of ethanol addition mL/min	Pt concentration mol/L	Ethanol/water ratio
Effect of temperature and rates of ethanol addition			
20 °C	0.5	0.0125 (0.0048g Pt salt + 1mL ammonia*)	10:1
0 °C	0.5	0.0125 (0.0048g Pt salt + 1mL ammonia)	10:1
0 °C	10	0.0125 (0.0048g Pt salt + 1mL ammonia)	10:1
Effect of salt concentration in mother solution			
0 °C	0.5	0.0125 (0.0048g Pt salt + 1mL ammonia)	10:1
0 °C	0.5	0.003 (0.0048g Pt salt + 4 mL ammonia)	10:1
0 °C	0.5	0.001 (0.0048g Pt salt + 10 mL ammonia)	10:1
Effect of ethanol/water ratio			
0 °C	0.5	0.0125 (0.0048g Pt salt + 1mL ammonia)	1:1, 1:2 and 10:1

*Ammonia indicates ammonia solution.

c) Controlled growth of SiO₂ nanotubes

Optimised procedures of synthesis

Under a stirring rate of 300 rpm, 0.0125 mmol [Pt(NH₃)₄](HCO₃)₂ were dissolved in 1 mL ammonia solution (20 °C, pH 10), then 0.7 mL ethanol were added into the solution. Afterwards the system was kept inside an ice bath (ca. 0 °C) for at least 8 min, then 14 µL TEOS were added into it and stirred for 2 minutes. With increased stirring rate of 1000 rpm, 0.1 mL ethanol were injected rapidly into the mixture and 2 minutes later the stirring rate was decreased to 300 rpm and 10 mL ethanol were added at a rate of 0.5 mL/min into the reaction system. Monodisperse and ultralong template-filled SiO₂ NTs were achieved after at most 4 hours of stirring.

Factors influencing the morphology of the product

The following two groups of samples were prepared for understanding the relationship between the reaction parameters and the morphology of the product.

Group A:

The rate of addition of 10 mL ethanol was varied as 0.25 mL/min (**A_{0.25}**), 0.5 mL/min (**A_{0.5}**) or 2 mL/min (**A₂**). All the other parameters were kept constant.

Group B:

The process of injecting 0.1 mL ethanol at 1000 rpm was omitted. The 10 mL ethanol were directly added at rates of 0.25 mL/min (**B_{0.25}**), 0.5 mL/min (**B_{0.5}**) or 2 mL/min (**B₂**). Other parameters were kept constant.

3.1.1.3 TiO₂ nanotubes

a) General growth of TiO₂ nanotubes

Optimised procedures of synthesis

At 20 °C, 0.0048 g [Pt(NH₃)₄](HCO₃)₂ were dissolved in 1 mL ammonia solution (pH 10.40, 20 °C). After that, 10 mL ethanol were droply added into the salt solution to form a fluffy suspension, which was afterwards soaked inside a cooling bath (around -30 °C), made by mixing ethanol and liquid N₂. Meanwhile, a solution of 43 µL TBOT, 43 µL DEG and 5 mL ethanol was prepared and cooled in the same bath. The typical molar ratio of the reactants, i.e. Pt salt and

TBOT, was kept at 1:10. Liquid N₂ was supplied continuously to keep the bath at -30 °C. One hour later, the solution of TBOT was dropped slowly into the suspension of the template. The resultant mixture was kept at -30 °C for 3 h and then warmed up naturally by stopping the addition of liquid N₂. After 12 h, the sample of template-filled TiO₂ NTs in the general growth route was achieved. The whole process was carried out with a stirring rate of 300 rpm.

Without washing, the opalescent sample was dried in air, scraped from the glass plate and calcined in a Muffel furnace. Two different conditions were applied for the heating treatment: in one case at 500 °C for 5 h with a heating rate of 5 °C/min and in the other case at 700 °C for 5 h with a heating rate of 5 °C/min.

Influences of reaction parameters on the synthesis

The following experiments were carried out to study the effects of reaction parameters on the morphology of the products. Here, the molar ratio of Pt to TBOT was always kept at 1:10.

Table 3.2 Experimental parameters of the TiO₂ samples

pH value of ammonia solution 20 °C	Cooling conditions	DEG / TBOT mol/mol
Role of cooling		
10.40	-70 °C for 3 h	7:1
10.40	-30 °C for 3 h	7:1
10.40	-20 °C for 3 h	7:1
Role of pH value of ammonia solution		
10.00	-30 °C for 3 h	7:1
10.40	-30 °C for 3 h	7:1
10.64	-30 °C for 3 h	7:1
Role of DEG / TBOT molar ratio		
10.40	-30 °C for 3 h	0
10.40	-30 °C for 3 h	7:1
10.40	-30 °C for 3 h	14:1

b) Controlled growth of TiO₂ nanotubes

At 20 °C, 0.0048 g (0.0125 mmol) of [Pt(NH₃)₄](HCO₃)₂ were dissolved in 1 mL ammonia solution (pH 10.40, 20 °C) forming a mother solution to which 0.6 mL ethanol was then added. After cooling the mother solution at -30 °C for 2 minutes, a solution obtained by mixing 22 µL TBOT, 22 µL DEG and 10 mL ethanol, already being cooled at -30 °C for 10 minutes, was slowly dropped into it. During the process, the initially transparent solution turned into a white suspension. The resulting mixture was kept at -30 °C for 3 h and then warmed up naturally in air. After 12 h, the sample of template-filled TiO₂ NTs by controlled growth was achieved. The whole procedure was carried out with a stirring rate of 300 rpm.

A drop of the sample was deposited on a sample holder of SEM. After evaporation of the solvent, the sample holder was heated at 500 °C for 5 h with a heating rate of 5 °C/min.

3.1.2 SiO₂ nanotubes with templates of [Co(NH₃)₆](HCO₃)(CO₃)·2H₂O

3.1.2.1 Chemicals

Hexaammine cobalt(III) chloride, [Co(NH₃)₆]Cl₃ (Aldrich)

Amberlite IRA-402 (Cl form, strong base, Fluka)

NaHCO₃ (p.a., Merck)

AgNO₃ (p.a., Merck)

65% HNO₃ (p.a., Riedel-de Haen)

Tetraethyl orthosilicate (TEOS, > 98%, p.a., Merck)

Ammonia solution (p.a., Merck) (pH value: from 10 to 11.06)

3.1.2.2 Preparation of [Co(NH₃)₆](HCO₃)(CO₃)·2H₂O

At first, a certain amount of ion-exchange resin of Amberlite IRA-402, having been soaked in distilled water longer than 2 h, was filled inside a glass colume (24 mmϕ × 160 mm L). Then a saturated NaHCO₃ aqueous solution was used to rinse the resin till all the effluent consists of only HCO₃⁻. Exchange completeness of Cl⁻ by HCO₃⁻ was proven using binary testing agents of

0.5 M AgNO₃ and 2 M HNO₃. 0.2 g [Co(NH₃)₆](Cl)₃ were dissolved in 20 mL distilled water and then slowly passed through the completely HCO₃⁻ replaced ion-exchanger. The purity of effluent, i.e. the [Co(NH₃)₆](HCO₃)(CO₃)·2H₂O aqueous solution, was also examined using the binary testing agents of AgNO₃ and HNO₃ solution.

For the preparation of powdered products, large amount of ethanol was poured into the [Co(NH₃)₆](HCO₃)(CO₃)·2H₂O aqueous solution, the resultant fluffy light orange precipitates by a glass filter (ROBU, Por. 5, pore size: 1 – 1.6 μm) with the assistant of water vacuum pump. The precipitates were washed with ethanol for several times and dried in air.

3.1.2.3 Synthesis of Co-containing SiO₂ nanotubes:

In a typical procedure, 0.0044 g powder of [Co(NH₃)₆](HCO₃)(CO₃)·2H₂O was dissolved in 1 mL ammonia solution (pH = 10.64, 20 °C). Afterwards 10 mL ethanol was dropped into the solution and consequently fluffy precipitates appeared. Then 28 μL TEOS (molar ratio of TEOS to Co is 10:1) was added. The whole reaction was carried out at room temperature and at a stirring rate of 300 rpm. After 12 h stirring, the light orange product was desiccated in air. After the calcination at 400 °C for 5 h, hollow silica NTs were obtained. Either air or H₂ was used as the calcination atmosphere.

3.1.2.4 Factors influencing the morphology of product

The following experiments were carried out to study the effects of reaction parameters (Table 3.3) on the morphology of products. In all experiments, 28 μL TEOS was added. Hence the molar ratio of Co to TEOS was kept at 1:10.

Table 3.3 Experimental parameters of the samples using Co templates

Concentration g/mL	pH of ammonia solution 20 °C	Rate of ethanol addition mL/min	Sample name
Effect of concentration of template salt			
0.0011 (0.0044g Co salt in 4 mL ammonia*)	10.64	1.67	A1
0.0022 (0.0044g Co salt in 2 mL ammonia)	10.64	1.67	A2
0.0088 (0.0044g Co salt in 0.5 mL ammonia)	10.64	1.67	A3
Effect of pH value			
0.0022 (0.0044g Co salt in 2 mL ammonia)	10.00	1.67	A4
0.0022 (0.0044g Co salt in 2 mL ammonia)	10.64	1.67	A2
0.0022 (0.0044g Co salt in 2 mL ammonia)	11.06	1.67	A5
Effect of rate of precipitation			
0.0022 (0.0044g Co salt in 2 mL ammonia)	10.64	1.67	A2
0.0022 (0.0044g Co salt in 2 mL ammonia)	10.64	0.67	A6

* Ammonia indicates ammonia solution.

3.2 Characterization

In the following all methods of characterization of the samples are described, including the working principle, the sample preparation, and the operative conditions of measurements.

3.2.1 X-ray diffraction

X-ray diffraction is an extremely important technique in the field of material characterization to obtain the constitutional and structural information from crystalline materials. Single-crystal X-ray diffraction requires single crystals of appropriate size (at least 10 to 100 μm in length) and is easier to solve structures of crystals than powder technique. However, the latter one can determine the constituents of a mixture of crystalline solid phases.

3.2.2.1 X-ray powder diffraction

a) Working principle

X-rays are high-energy electromagnetic radiation with wavelengths ranging from about 1 to

10000 pm. The X-rays used to determine crystal structures usually have wavelengths of 50 – 250 pm. When an X-ray beam is incident on a crystalline material, reflections (or diffractions) occur due to the interaction between the incident beam and the periodically aligned atoms. This scattering process is schematically illustrated in Figure 3.1.

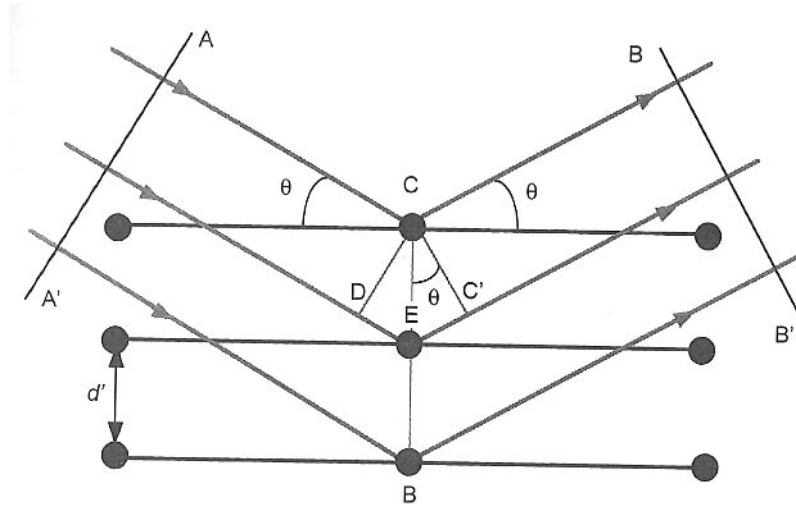


Figure 3.1 Diffraction of X-rays by a crystal.

The waves scattered by each atom will reinforce in certain directions and cancel in others. The scattering from a given family of planes will only be strong if the X-rays reflected by each plane arrive at the detector in phase. This leads to a relationship known as Bragg's law [1]

$$n\lambda = 2d \sin \theta \quad (3.1)$$

where λ is the wavelength of the X-ray, d is the lattice spacing of the reflecting plane, and θ is the diffraction angle. The integer n is known as the order of the corresponding reflection. Note that the angle of deviation of the X-ray is 2θ from its initial direction. This is fairly restrictive for a single crystal since, for a given λ , even if the detector is set at the correct 2θ for a given d spacing within the crystal, there will be no diffracted intensity unless the crystal is properly aligned to both the incident beam and the detector. The essence of the powder diffraction technique is to illuminate a large number of crystallites, so that a substantial number of them are in the correct orientation to diffract X-rays into the detector.

A set of parallel lattice planes is represented by the Miller indices (hkl), which are defined as

the smallest integral multiples of the reciprocals of the plane intercepts on the axes. A given θ value is correspondent to a set of parallel lattice planes (hkl). In the case of a set of equivalent lattice planes, the Miller indices are placed in braces, $\{hkl\}$.

Experimentally, a powder diffraction peak is characterized by three sets of parameters: peak position, peak intensity and peak shape profile [2]. The position of the peak is determined by equation 3.1. The intensity of the peak is determined by the coherent interference of the individual atoms that decorate the crystal lattice. The peak profile depends on the type of radiation beams used and the exact experimental setup.

For the approximation of the average grain size D , the well-know Scherrer equation is commonly employed

$$D = \frac{K\lambda}{\beta_L \cos \theta} \quad (3.2)$$

where β_L is the full-width-at-half-maximum of the peak profile. The coefficient K has been found to be around 0.9 [3]. The accuracy of Scherrer equation depends on the precise shape of the grains and the grain size distribution [1].

b) Sample preparation and operation conditions

To avoid unwanted artefacts, the preparation of samples is an important consideration in powder diffraction experiments. One issue is that preferred orientation should be avoided. The grains of a sample may tend to align, especially if they have a needle or platelike morphology, so that reflections in certain directions are enhanced relative to others. Various measures such as mixing the powder with an inert material chosen to randomise the grains or pouring the sample sideways into the flat plate sample holder are in common use. A related issue is that a specimen in a diffractometer must be sufficiently powdered. It may be necessary to grind or sieve the sample, especially in the case of strongly absorbing materials.

Most commercially available diffractometers employ the Bragg-Brentano parafocusing geometry. This reflection mode uses a flat plate sample holder lying tangent to the focusing circle. With this arrangement, the divergent beam from the anode/monochromator is “focused”

into the receiving slit in front of the detector and thus yields peaks [3]. The principle advantages of the reflection mode are that firstly a large sample area can be irradiated and the high intensity thereby produced allows fast scan rates, and secondly no adsorption correction has to be made if an “infinitely” thick sample is used. The disadvantages of this reflection mode are that a larger sample volume is required and that the preparation of a flat sample tends to increase preferred orientation.

In this study, the powder XRD patterns of samples were recorded on a Philips PW 1729 Spectrometer (Bragg-Brentano parafocusing geometry, $\lambda = 1.5418 \text{ \AA}$, Voltage = 35 kV, Current Intensity = 40 mA) in collaboration with Dr. Xiaobo Yang at the Institute of Physical Chemistry, University of Hanover. The instrument was equipped with a fixed divergence slit and a scintillation counter. Since the samples were needle-like, the preferred orientation is inevitable. The intensity data were measured by step scanning in the 2θ range between 10° and 100° , with a 2θ step size of 0.05° and a measuring time of 2 or 5 seconds per point.

3.2.2.2 Single-crystal X-ray diffraction

a) Working principle

The fundamental principle of X-ray single-crystal diffraction is based on the Bragg's law. In practice, a single crystal is installed on a diffractometer and data are collected under computer-controlled operation. From these data the fractional coordinates describing the positions of the atoms within the cell, some characteristics of their thermal motion, the cell dimensions, the crystal system, the space group symmetry, the number of formula units per cell, and a calculated density can be obtained.

b) Sample preparation and operation conditions

For single-crystal X-ray diffraction, a big crystal of $[\text{Co}(\text{NH}_3)_6]\text{HCO}_3\text{CO}_3 \cdot 2\text{H}_2\text{O}$ was selected from the dry powders precipitated from the aqueous solution of the cobalt salt with a large amount of ethanol.

The XRD measurement of the single crystal was carried out on a Stoe IPDS (Imaging Plate Diffractometer System) in collaboration with Dr. Rudolf Wartchow at the Institute of Inorganic

Chemistry, University of Hanover.

3.2.2 Electron Microscopy

For characterization of materials dominated by particles with sizes in the nanometer range, electron beam methods are indispensable analytic tools. In this study, two kinds of methods have been involved: scanning electron microscopy and transmission electron microscopy.

3.2.2.1 Scanning Electron Microscopy (SEM)

Scanning electron microscopy is the best-known and most-widely-used surface analytical technique. SEM, accompanied by Energy Dispersive X-ray Spectroscopy (EDXS), is considered a relatively rapid, inexpensive, and basically non-destructive approach to surface analysis. In this study, SEM was the primary tool employed for the characterization of samples.

a) Working principle

A SEM consists of a column, electronics and a number of detectors. Primary monochromatic electrons are emitted from an electron gun and accelerated down the evacuated column. After being de-magnified and focused with the aid of electro- and magnetostatic lenses and constricted by condenser apertures, the electrons are formed into a probe that is scanned on the sample surface. Simultaneously, secondary electrons and backscattered electrons are emitted from the sample and then detected by appropriate detectors. When the primary electron is scanned in a regular pattern covering a rectangular area, the signal output onto the detector gives a map of signal intensity coming from the sample, leading to the SEM image [1,2].

The beam electrons interact with atoms in the specimen by inelastic and/or elastic scattering when they bombard a point on the surface of the specimen. The signals resulting from these interactions (e.g., electrons and protons) escape from different depths within the sample due to their unique physical properties and energies. Secondary electrons, backscattered electrons and characteristic X-rays are the most widely utilized signals in a SEM [1,2].

Secondary electrons (sample depth: nm range) are low-energy (2 to 5 eV) electrons ejected from outer shells of the sample atoms after inelastic interactions. The term “secondary” thus

refers to the fact that this signal is not a scattered portion of the probe, but a signal generated within the specimen due to the transfer of energy from the beam to the specimen [1]. Secondary electron intensity is a function of the surface orientation with respect to the beam and the detector and thus produces a topographic image of the specimen.

Backscattered electrons (sample depth: several tens of nm to 100 nm) are electrons from the incident probe that undergo elastic interactions with the sample, while elastic interactions are defined by a change in trajectory of the beam electrons without loss of energy. They make up the majority of electrons emitted from the specimen at high beam voltage, and their average energy is much higher than that of the secondary electrons. The intensity of backscattered electron signal is a function of the average atomic number (Z) of the specimen, with heavier elements producing more backscattered electron signals. It is thus a useful signal for generating compositional images, in which higher Z phases appear brighter than lower Z phases.

Characteristic X-rays (sample depth: in the μm range) are generated by inelastic interactions of the probe electrons with specimen atoms. During inelastic interactions, inner shell electrons of specimen atoms are ejected, with the result that vacancies are formed at their original positions. Afterwards, outer shell electrons move to the vacancies and their excessive energies are emitted in the form of X-rays characteristic for individual elements of the specimen atoms. By analysing the characteristic X-rays, the elements that constitute the specimen can be identified, and also quantitative calculation of their weight concentrations can be made. A widely used method of analysing characteristic X-rays is by the EDXS.

b) Sample preparation and operation conditions

Samples, suspended in proper solvents, were dropped directly on sample holders in order to keep the original morphology intact. Powder samples were at first dispersed in ethanol by a supersonic bath for several seconds and then dropped on a sample holder. After evaporation of the solvent, the sample is ready for SEM measurements.

Because of the poor conductivities of most of the samples, part of the irradiated electrons may be absorbed. This charge causes many errors in the observations. In general, methods such as metal coating and observations with low accelerating voltage are done to prevent a specimen

from acquiring an electrostatic charge. For the samples in this study, the latter method was adopted.

The SEM images were recorded on a JEOL JSM-6700F apparatus equipped with a cold-field emission gun (FEG). The instrument was operated at low accelerating voltages ($V_{\text{acc}} = 1$ or 2 kV) in order to minimize the charging of the specimens.

EDXS measurements were carried out in collaboration with Dr. Jürgen Köpcke on a CAMECA SX-100 Microprobe installed with the OXFORD EDX-system at the Institute of Mineralogy, University of Hanover.

3.2.2.2 Transmission Electron Microscopy (TEM)

TEM is a powerful and unique technique to reveal the internal microstructure of materials at the nanometer level. In this study, it was routinely employed to study the distribution of metal nanoparticles inside the metal oxide nanotubes.

a) Working principle

A TEM is designed for observing transmitted images, in analogy to an optical microscope. Simply speaking, in a TEM, an electron beam is irradiated on a specimen. The specimen must be thin enough to realize the transmission of the beam through it. The transmitted beam is observed after being magnified by electron lenses.

Three types of contrasts are usually contained in TEM images: diffraction absorption contrast, contrast produced by mass thickness or atomic number, and phase contrast [2]. In diffraction absorption contrast just electrons that have not been scattered by the object contribute to image formation. Diffracted electrons are absorbed by an appropriate aperture that is inserted in the back focal plane of the objective lens. Mass thickness or atomic number (Z) produces contrast. Atoms with different Z exhibit different powers of scattering. With increasing Z of the atoms in an object, their scattering cross-section increases. Phase contrast arises from the phase differences between unscattered and diffracted electrons. This interference method allows to obtain high-resolution TEM images on thin specimen that act mainly as weak-phase objects, i.e. objects that do not influence the amplitude of an electron wave but slightly the phase. This kind

of contrast is sensitive to the atom distribution in the specimen and is the basis of high resolution TEM.

Two kinds of modes are usually employed in TEM operations: image mode and diffraction mode. In the image mode, the internal structure of a thin specimen is observed. The thus-produced image has no depth profile as the electrons pass through the specimen. In the diffraction mode, either a spot pattern or a ring pattern is observed depending on the grain size and orientation of grains in the specimen within the selected area. The technique of Selected Area Electron Diffraction (SAED) is a powerful tool to identify a known phase and/or to determine the orientation of a crystal.

b) Sample preparation and operation conditions

Powder samples for transmission electron microscopy (TEM) were deposited on a holey carbon foil supported by a copper grid. The TEM images were recorded either on a Philips CM30 microscope (accelerating voltage $V_{\text{acc}} = 300$ kV, LaB₆ cathode) in collaboration with Dr. Frank Krumeich, ETH Zürich (Switzerland) or in our group on a JEOL-2100F ($V_{\text{acc}} = 200$ kV, FET cathode, point resolution 0,19 nm) in collaboration with Dr. Armin Feldhoff.

3.2.2.3 Scanning Transmission Electron Microscopy (STEM)

As its name suggests, the STEM is a combination of the SEM and the TEM. Thin specimens are viewed in transmission, while the images are formed by the scanning of an electron probe.

a) Working principle

A large annular detector is special for STEM, resulting in that each atom in the specimen scatters the incident probe in proportion to the square of the atomic number (Z), hence this kind of microscopy is also referred to as Z -contrast imaging.

The key difference between STEM and conventional TEM lies in their modes of image formation. The former provides almost perfect incoherent imaging whereas the latter provides almost perfect coherent imaging [1].

In comparison to SEM which gives a topographic image of the surface region of a bulk sample, STEM gives a transmission image through a thin region of the bulk. Backscattered

electrons in SEM give a Z-contrast image analogous to that obtained with the STEM annular detector, except at lower resolution and contrast.

b) Sample preparation and operation conditions

The STEM images of a sample of cobalt-containing SiO₂ NTs were recorded on a CM30 microscope (Philips, accelerating voltage $V_{acc} = 300$ kV, LaB₆ cathode) in collaboration with Dr. Frank Krumeich, ETH Zürich (Switzerland).

3.2.3 Thermogravimetric analysis

In this study Thermogravimetry (TG) and Differential Thermal Analysis (DTA) were employed to determine phase transformations of samples as a function of temperature.

a) Working principles

TG is defined as a technique in which the mass of a substance is measured as a function of temperature whilst the substance is subjected to a controlled temperature program [1]. An apparatus called a thermobalance is used to obtain a thermogravimetric curve.

Thermogravimetric data can be presented in two ways. The TG curve is a plot of the mass against time or temperature, with the mass loss plotted downward and mass gains plotted upward relative to a baseline. Alternatively, data can be presented as a derivative thermogravimetric (DTG) curve, which is a plot of the rate of change of mass with respect to time or temperature against time or temperature.

In DTA, the temperature difference between a substance and a reference material is measured as a function of temperature while the substance and reference material are subjected to a controlled temperature program [1]. In a DTA curve, the temperature difference should be plotted on the ordinate with endothermic reactions downward and temperature or time on the abscissa increasing from left to right.

b) Operation conditions

In this study, TG and DTA curves of samples were recorded in collaboration with Dr. Claus H. Rüscher at the institute of mineralogy, University of Hanover. The instrument is a

Setsys evolution 1650 (Setaram) simultaneous analyzer operating in the range of 20 – 800 °C with a heating rate of 5 °C/min under a helium flow of 5 mL/min. α -alumina was used as reference in a 0.3 cm³ alumina crucible.

3.2.4 Infrared Spectroscopy

a) Working principle

Infrared (IR) spectrum is tied up with the changes in the vibrational state of molecular bonds. The requirement for a vibration to be infrared active is that during the vibration there must be a change in the electric dipole of the molecule. Diatomic molecules with the same atoms, in principle, cannot be excited to vibrate, because they do not have any dipole moment. Molecules consisting of various types of atoms, however, can always interact with infrared radiation.

The basis of the IR experiment is to pass infrared radiation through a substance and measure which energies of the applied radiation are transmitted by the sample.

IR spectroscopy has become one of the most important analytical methods for preparative as well as analytical chemists. It provides a direct evidence on the constitution of an unknown sample since inherent correlations exist between the position of absorption bands and particular structural groups. From the “fingerprint region” in the range between about 1500 and 650 cm⁻¹, substances can be specifically identified by spectral comparison. Besides, each component of a mixture can be quantitatively determined from the IR spectrum, if absorption bands are unaffected.

b) Operation conditions

The IR spectrums of samples before and after thermal treatment were recorded in collaboration with Dr. Claus H. Rüscher, using a Bruker IFS 66v FTIR Spectrometer at the institute of mineralogy, University of Hanover.

3.2.5 N₂ Adsorption

a) Working principle

The adsorption isotherm is usually defined as the relationship, at constant temperature, between n , the quantity of adsorptive expressed in moles per gram of solid, and p/p^o , the relative pressure, while p^o being the saturation vapour pressure of the adsorptive [5].

N₂ adsorption at 77 K is a standard and wide used method to determine the specific surface area and pore size distribution of porous materials. The physical adsorption of N₂ by non-porous solids, in the vast majority of cases, gives rise to a Type II isotherm as shown in Figure 3.2 (dashed line). As to porous solids, their isotherms are dependent on the pore sizes. According to IUPAC (International Union of Pure and Applied Chemistry) recommendations [6], pores are classified with respect to their sizes as

micropores: width (or diameter) below 2 nm,

mesopores: width between 2 and 50 nm, and

macropores: width greater than 50 nm.

For a typical mesoporous solid, e.g. porous silica, the physical adsorption of N₂ gives rise to a Type IV isotherm as depicted in Figure 3.2 (solid line). A characteristic feature of a Type IV isotherm is its hysteresis loop.

For the interpretation of Type IV isotherm, a model proposed by Zsigmondy [7] assumed that the initial part of the isotherm (ABC in Figure 3.1), adsorption is restricted to a thin layer on the walls, until at D, the inception of the hysteresis loop, capillary condensation commences in the finest pores. As the pressure is progressively increased, wider and wider pores are filled until at the saturation pressure the entire system is full of condensate. Since a problem of nucleation arises during the condensation process of a liquid phase from the vapour and in the converse process of evaporation (FJD in Figure 3.2) this problem is avoided, the two processes do not necessarily take place as exact reverses of each other. That can account for the occurrence of hysteresis in mesoporous solids.

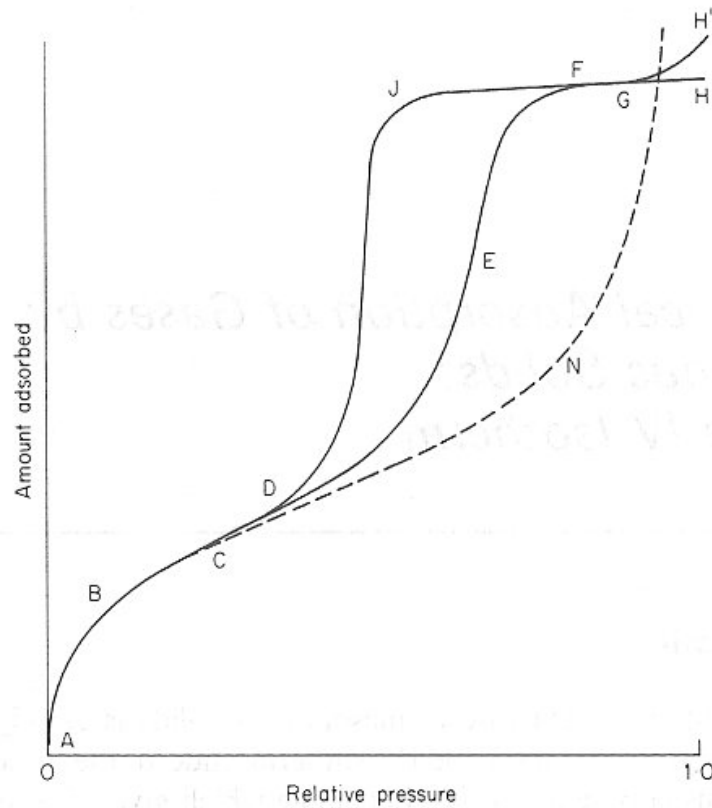


Figure 3.2 A Type II isotherm (dashed line) and a Type IV isotherm (solid line) [5].

Determination of specific surface area

To obtain specific surface areas from the adsorption isotherm, the Brunauer-Emmett-Teller (BET) method has proved remarkably successful for a non-porous material.

The BET treatment is based on a kinetic model of the adsorption process put forward by Langmuir, i.e., a state of dynamic equilibrium in which the rate at which molecules arriving from the gas phase and condensing on to bare sites is equal to the rate at which molecules evaporate from occupied sites. By adopting the Langmuir mechanism (well adapted to the adsorption of a monolayer) but introducing a number of simplifying assumptions, Brunauer, Emmett and Teller in 1938 [8] were able to construct their well-known equation for multilayer adsorption,

$$\frac{p/p^o}{n(1-p/p^o)} = \frac{1}{n_m c} + \frac{c-1}{n_m c} \frac{p}{p^o} \quad (3.3)$$

where the BET parameter c gives information regarding interactions of adsorbate (N_2 molecules) with adsorbent, and n_m is the monolayer capacity or moles of adsorbate per gram of adsorbent. The specific surface area A is defined as the surface area of 1 g of the solid and is calculated by the simple equation [5]

$$A = n_m a_m L \quad (3.4)$$

where a_m is the average area occupied by a molecule of adsorbate in the completed monolayer on the surface of the solid. In case of N_2 at 77 K, $a_m = 0.162 \text{ nm}^2$. L is the Avogadro constant.

As mentioned above, the application of BET method in determination of the specific surface area of nonporous materials is very successful, but for a solid with presence of micropores, the specific surface area derived by BET procedure will be erroneously high due to its distorted isotherm in the low-pressure region.

Standard isotherm and t -plot

For a given gas adsorbed on a series of nonporous substances differing in total area but similar in properties (such as metal oxides), the different isotherms were found to be superposable by mere adjustment of the scale of units of adsorption. Therefore, a single curve can represent the isotherms of a group of nonporous solids, though with some scatter, and it is called the standard isotherm [5].

A convenient means of detecting the superposability of the isotherm under test in comparison with that of the standard is provided by the t -plot of Lippens and de Boer [9]. This t represents the statistical thickness of the film, being equal to the multiplication of the number of statistical molecular layers in the film, n/n_m , and the thickness of a single molecular layer, namely σ (3.54 Å [10] for N_2 at 77 K). Based on the t -curve, which is a plot of the standard isotherm with t as the dependent variable, the isotherm under test are then re-drawn as a t -plot, i.e. a curve of the adsorbed amount plotted against t rather than against p/p^o . The change of independent variable from p/p^o to t is affected by reference to the standard t -curve.

If micropores are introduced into a solid, corresponding to the enhanced uptake in the low-pressure region of the isotherm, its t -plot curve rise steeply at this region and then gradually level off, exhibiting linearity at higher pressures [11]. The linear part can be extrapolated to the adsorbed amount axis, and the intercept provides the amount adsorbed in micropores, which could be used to calculate the micropore volume. The slope of the linear part can be converted to the external surface area of the solid [12,13].

If both micropores and mesopores are present in the solid under study, the deviations of the t -plot from linearity can be observed in both low and high-pressure regions [11].

Determination of mesopore size distribution

For the calculation of pore size distribution of mesoporous solids, Barrett-Joyner-Halenda (BJH) method is a very useful characterization technique [14]. In this approach, the adsorption process in mesopores was considered to consist of the formation of the adsorbed layer on pore walls and subsequent condensation of the adsorbate in the interior of the pore. The desorption process was assumed to proceed in the opposite way, i.e., by capillary evaporation from the interior of the pore followed by a gradual decrease in the thickness of the adsorbed film on the pore surface. In order to develop a useful tool for the analysis of porosity, Barrett et al. assumed that the formation of the adsorbed film is essentially independent of the pore size, r^p , and used the statistical film thickness curve t for a macroporous reference adsorbent. And as a result the Kelvin equation is changed to

$$r^p \left(\frac{p}{p^o} \right) = \frac{2\gamma V_L}{RT \ln(p^o / p)} + t \left(\frac{p}{p^o} \right) \quad (3.5)$$

where V_L is the molar volume of the liquid adsorbate, γ is its surface tension, R is the universal gas constant, and T is the absolute temperature. The value of t , with a unit of nm, can be obtained from the empirical Halsey equation [11]:

$$t = 0.354 \left[-5 / \ln(p / p^o) \right]^{1/3} \quad (3.6)$$

For any point $(n_i, p_i / p^o)$ on the isotherm, the volume v^p of all the pores having r^p -values up to and including r_i^p is given by $n_i V_L$. From the curve of v^p against r^p the

size distribution curve, i.e. dv^p / dr^p against r^p is immediately obtainable.

b) Sample preparation and operation conditions

The measurements of N₂ adsorption isotherm at liquid N₂ temperature on two samples, i.e. SiO₂ NTs before and after calcination, were carried out in Heyrovsky Institute of Physical Chemistry in Prague in collaboration with Dr. J. Rathousky, using a gas sorption analyzer (Micromeritics ASAP 2010). Both samples were degassed at 200 °C for 16 h prior to the measurement. The specific surface area was calculated using the BET equation. The pore size distribution was calculated by employing the BJH method.

4 Oxide nanotubes with templates of $[\text{Pt}(\text{NH}_3)_4](\text{HCO}_3)_2$

In this section, the synthesis and characterization of oxide nanotubes (NTs), including SiO_2 and TiO_2 , are described in detail using the nanofibers of $[\text{Pt}(\text{NH}_3)_4](\text{HCO}_3)_2$ (called “**Pt salt**” for simplicity in the following) as templates and are dealt with in three separated parts. At first, the oxide NTs prepared in the general growth route are characterised by a number of methods. One characteristic of the general oxide NTs is the broad size distribution of NTs in diameters, which originates from the template fibers of the Pt salt (called “**Pt templates**” for simplicity). Secondly, the growth mechanism of Pt templates was studied and suggested. Thirdly, the enhanced oxide NTs were prepared, based on the kinetic control over the anisotropic growth of Pt templates using TEOS monomer as a capping agent.

4.1 General growth of oxide nanotubes

Following the general synthesis route with the Pt templates as introduced in Figure 1.1 in Chapter 1, i.e., at first the formation of template nanofibers, then the coating with metal alkoxides and finally the heating treatment, oxide NTs, including SiO_2 and TiO_2 , have been successfully prepared.

The general growth of oxide NTs is explained with examples of the Pt templates, SiO_2 NTs and TiO_2 NTs in order to understand the evolution of morphology. Besides electron microscopic techniques like SEM, EDX, TEM, SAED, the samples were also characterised with XRD, thermogravimetric methods and IR spectroscopy.

4.1.1 Pt templates

As the structure-directing agents, the one-dimensional (1D) Pt templates developed through solvent modification determine the morphology of final NTs. Here the solvent modification is defined as the process of adding a large amount of ethanol into the aqueous solution of Pt salt. As a consequence white precipitates of the Pt salt, i.e. the Pt templates, were obtained. To ensure the completeness of the precipitation, the ratio of ethanol to water was usually set as

10:1.

4.1.1.1 Characterization with Electron Microscopy

For comparison, SEM images of the purchased Pt salt and the Pt templates are both exhibited in Figure 4.1.

In Figure 4.1A, it is seen that the particles are larger than 5 μm . Although most of the particles are not regular, there are still some particles showing rectangular edges (arrowed parts) in the purchased salt. Generally speaking, the commercial $[\text{Pt}(\text{NH}_3)_4](\text{HCO}_3)_2$ has already exhibited a 1D morphology, although quite vaguely.

Instead, in the Pt templates prepared by dissolution and re-precipitation in Figure 4.1B, the 1D morphology of the Pt salt is obvious. The regular geometric forms displayed externally by the Pt templates indicate its internal periodicity of atomic configuration, or in other words its crystalline structure. In addition, the size distribution of the Pt templates is rather broad, roughly speaking, spanning both nanometer and micrometer regimes. The nanometer-thick fibers (NFs) range mostly between 50 - 300 nm in diameter and 1 - 6 μm in length. The micrometer-thick fibers (MFs) are mostly 1 - 2 μm in diameter. It is necessary to mention here that, in analogy to the process of crystal growth, the size distribution of the fibrous Pt templates depends on many processing parameters, like temperature, pH value etc. Hereby, this sample is quite representative in its appearance, prepared under typical conditions listed in the legend.

Moreover, bearing in mind the concepts about the relative growth rate and habit introduced in Chapter 2, it could be concluded that this kind of Pt salt intends to grow into prismatic morphology due to the relative growth rates of the prism and pinacoid faces.

Accidentally, one tubular Pt template was observed as shown in Figure 4.1C. Its outer diameter is near 100 nm. This observation reflects that template fibers with hollow interiors could exist as well as those with solid cores. In addition, starting from the aqueous solution of Pt salt, not only solid single crystals, but also hollow ones have been cultivated by vapour diffusion in C. Hippe's thesis [1]. The growth mechanism of hollow tubes is supposed to be the preferential deposition of building blocks (atoms, molecules or ions) on the circumferential edges of the seeds because these sites had relatively higher surface energies than other sites on the surface [2] or since these locations dissipate the latent heat easily [3] during the

precipitation process. However, it still remains one unsolved question about the condition of occurrence of hollow or solid fibers in one sample.

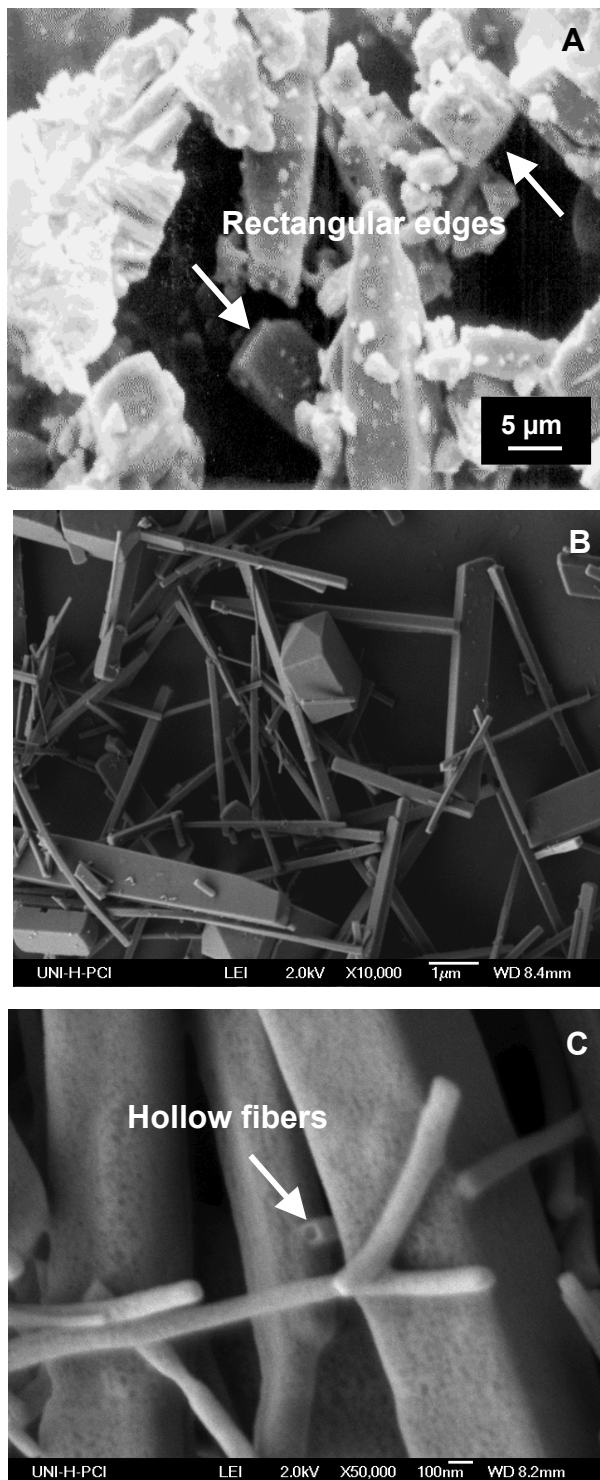


Figure 4.1 SEM images of (A) commercial $[\text{Pt}(\text{NH}_3)_4](\text{HCO}_3)_2$, (B) templates: fibers of $[\text{Pt}(\text{NH}_3)_4](\text{HCO}_3)_2$ after solvent modification (Parameters for the preparation of Pt templates were: 0.0125 M, room temperature and 1 ml ethanol/min) and (C) view of a tubular template nanofibers.

The TEM image of a fibrous template is shown in Figure 4.2. It was observed that the solid fiber, which was homogeneous at its original state, decomposed quickly under the electron beam in TEM. In the darker area the density of Pt element should be correspondingly higher. The situation should be similar to that which happens during the calcination. The Pt salt is reduced by the electrons and hence decomposed, releasing gases like H₂, N₂ and NH₃. The electron diffraction of the Pt template is therefore difficult to perform.

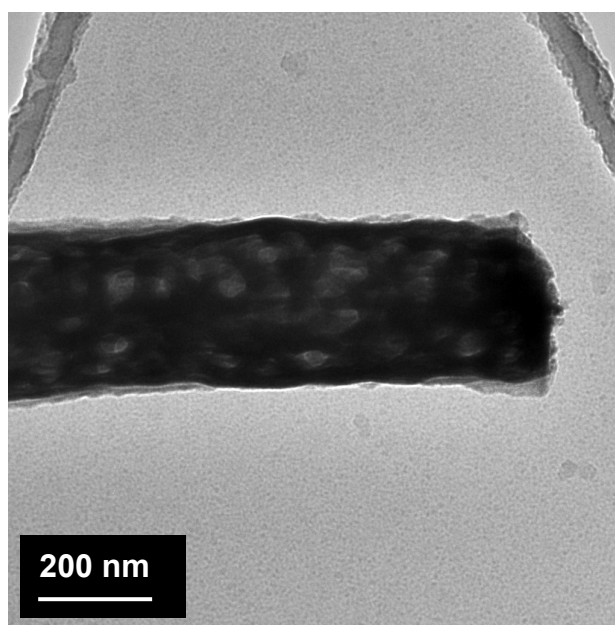


Figure 4.2 TEM image of a fibrous template.

4.1.1.2 Characterization with X-ray Diffraction

The XRD pattern of the commercial [Pt(NH₃)₄](HCO₃)₂ (pattern A) and the Pt templates (pattern B) are drawn in Figure 4.3. The relative intensity of them can be compared.

It could be learned that the peak positions of Pt templates agree very well with that of commercial salt. The peak intensities of template fibers are comparable to that of the commercial salt. It indicates that the Pt templates (50 nm – 2 μm in diameter) feature also a good crystallinity although it has obviously a relatively smaller dimension in thickness of fibers than the commercial salt (> 5 μm).

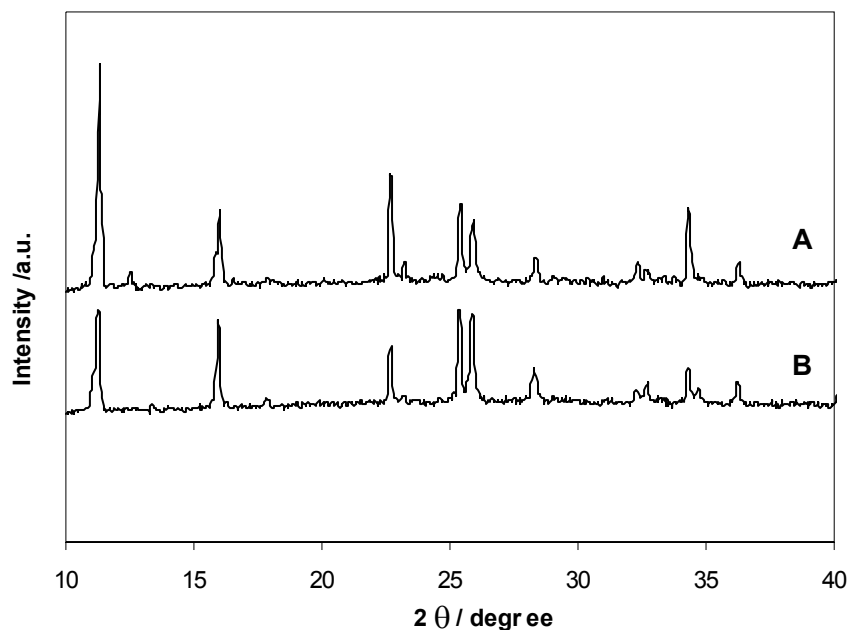


Figure 4.3 XRD powder patterns of (A) commercial salt and (B) Pt templates.

4.1.1.3 Formation of the needle-shaped Pt templates

By a rapid solvent modification, i.e. dripping ethanol into aqueous solution of the Pt salt, needle-shaped Pt templates of this salt was easily yielded, with more regular morphology and smaller size (even till 50 nm) in comparison with the 5- μm -thick commercial salt. The crystalline nature of the Pt templates is certified from both its morphology of tetragonal prism shown in SEM image (Figure 4.1) and the X-ray diffraction peaks of its powder pattern (Figure 4.3).

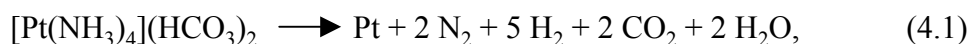
According to the theory of crystal growth in section 2.1.3, the formation of the template prisms should be divided into two processes: nucleation and growth. During the growth process, the growth rates of certain faces are relatively faster and these faces constitute the faces of prism in the final morphology of crystal. Instead, the faces with relatively slower growth rates form the faces of pinacoids. From the viewpoint of thermodynamics, the equilibrium morphology of the prismatic crystal is confined by the minimization of specific surface free energies [4].

In order to determine the relative growth rates of faces, in principle the Electron Diffraction installed in TEM is the effective tool. However, for the Pt templates, this tool is inapplicable due to the rapid decomposition of Pt templates under electron beam (as shown in Figure 4.2).

Moreover, it is also necessary to mention that a broad size distribution (100 nm to 2 μm in diameter) was characteristic for the thus-prepared Pt templates no matter what parameters of preparation were applied. The detailed study on the formation of Pt templates will be dealt with in section 4.2.

4.1.2 SiO₂ nanotubes

With TEOS acting as the coating agent, walls of SiO₂ formed around the rectangular template fibers in a sol-gel process, resulting in white template-filled SiO₂ NTs. After a heat treatment at 500 °C for 5 h in air, the Pt salt decomposed and auto-reduced to metallic Pt [5],



resulting in black Pt-containing SiO₂ NTs.

4.1.2.1 Electron Microscopy

The appearance of both the template-filled and metal-containing SiO₂ NTs were characterized with electron microscopies.

a) Scanning Electron Microscopy

In the SEM image recorded at low voltage as shown in Figure 4.4A, it could be noticed that the template-filled SiO₂ NTs exhibit clear and smooth surfaces, which indicate the complete consumption of TEOS on the surface of Pt templates in the sol-gel process. The 1D structures in this sample are observed to be the plaster cast of the Pt templates, containing fibers with diameters in regimes of both nanometer (ca. 50 - 400 nm) and micrometer (ca. 1 - 2 μm) and with lengths of ca. 1 - 6 μm . Due to the broad size distribution native to both the Pt templates and in turn the current sample, the change in thickness of individual fibres could not be observed by only comparing their SEM images.

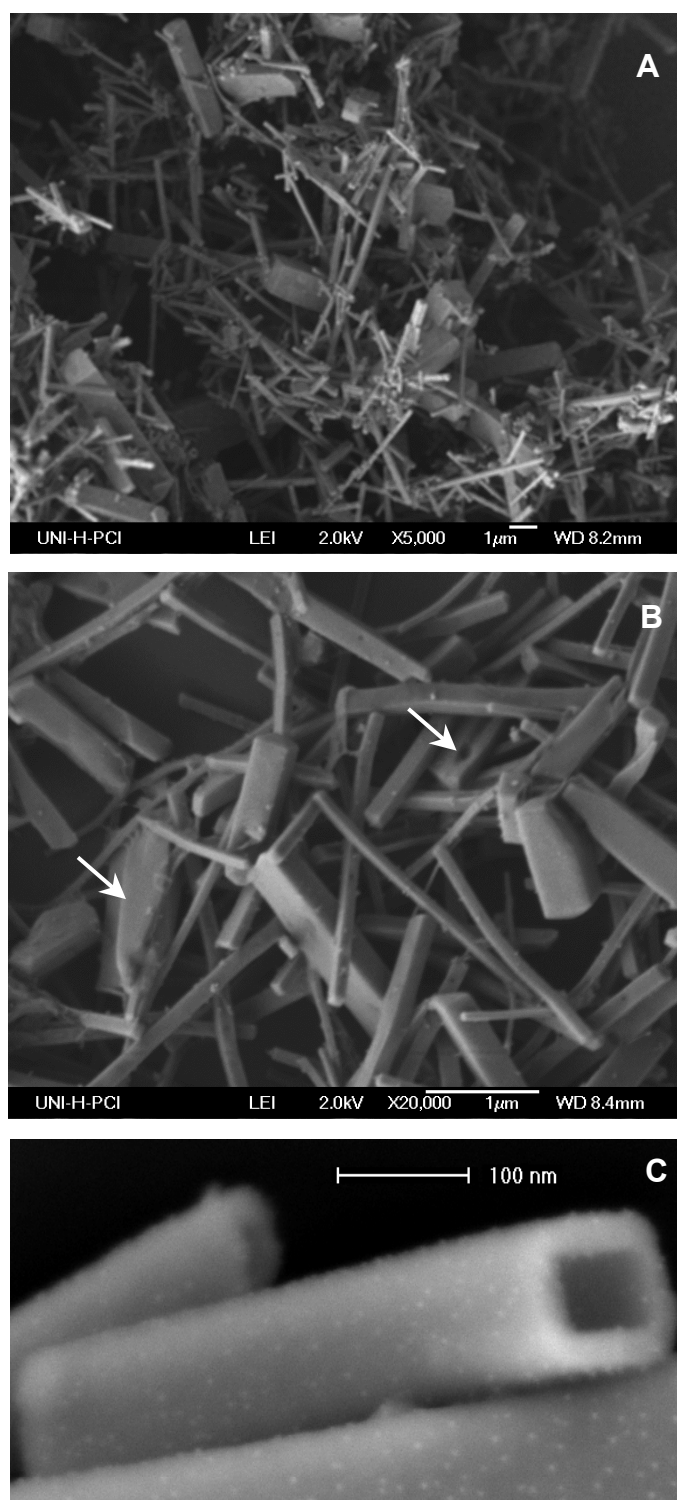


Figure 4.4 SEM images of (A) template-containing SiO₂ NTs at a low magnification and (B) at high magnification and (C) SiO₂ NTs doped with Pt metals after the heat treatment at 500 °C for 5 h. The ratio of Pt:SiO₂ is 1:10 here.

The closed ends of the salt-filled SiO₂ NTs are evidenced in Figure 4.4 B, which was recorded at a four times higher magnification than the micrograph in Figure 4.4A. Moreover, some defects or irregularities (indicated with arrows) in the morphology of this sample have been observed.

From the SEM image taken at a high voltage as shown in Figure 4.4C, rectangular SiO₂ NTs with hollow cavities could be clearly observed. The white points decorating the grey background of tube walls are ascribed to nanoparticles of metallic Pt. What happened during the heat treatment could be interpreted as at first the autoreduction of the Pt templates into Pt nanoparticles [6] and afterwards the dispersion into the SiO₂ walls due to the high thermal mobility of Pt particles. The process of autoreduction and dispersion might have happened simultaneously.

As to the change of opening state of NTs after heat treatment, a possible reason could be the mechanical abrasion happened during the sample preparation. It should be especially serious when the sample was scraped from a glass plate with a steel spoon to achieve dry powders. Other possible reasons are discussed in section 4.2.

b) Transmission Electron Microscopy and Electron Diffraction study

The hollow interior of calcined samples has been observed in TEM. Because of the high electron scattering potential of platinum, Pt particles appear with a black contrast under the selected imaging conditions (bright-field), whereas the regions containing SiO₂ are grey [7].

As shown in TEM images exhibited in Figure 4.5, the SiO₂ NTs could be classified into empty and filled tubes according to their filling states. On the one hand, for the empty tubes, they are not only open ended (Figure 4.5A) but also closed ended (Figure 4.5B). Therefore the chance that the Pt templates have escaped from the interior to the exterior of tubes would be little. On the other hand, for the filled ones, the filling degrees are different. As shown in Figure 4.5A, a tube being fully filled is indicated with an arrow, the Pt content of which is apparently higher than the other tubes.

In some cases the filling in tubes results even in continuous nanowires of Pt as shown in Figure 4.5C. Apparently, those NTs that contain continuous nanowires inside usually have inner diameters around 50 nm. The inverse conclusion must, however, certainly not be drawn, since some NTs with inner diameters around 50 nm do not contain nanowires inside. But the

chance for Pt nanowires is higher in those thinner NTs.

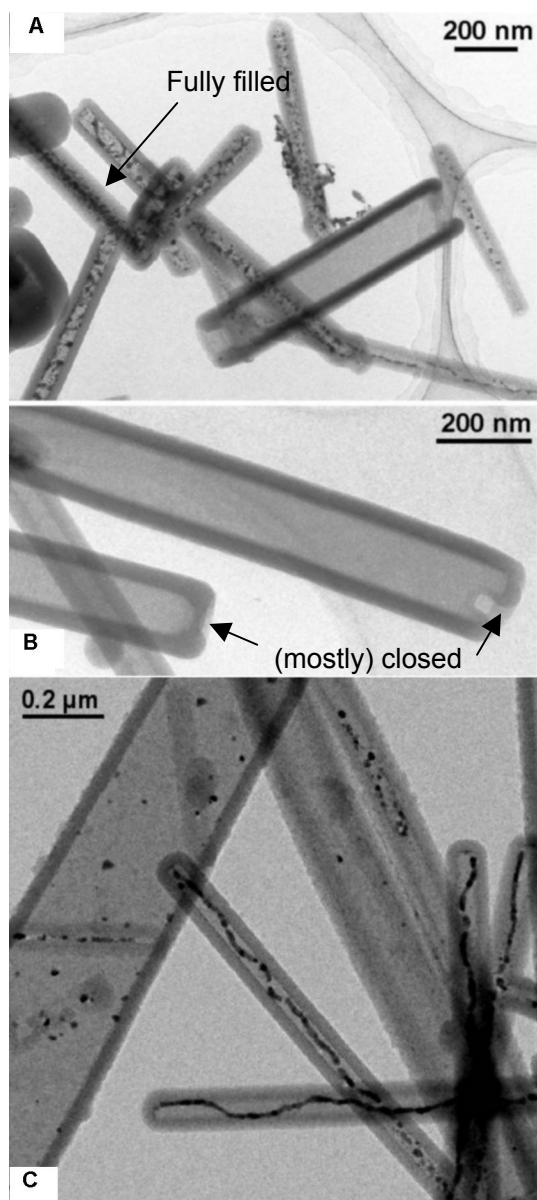


Figure 4.5 TEM images: (a) coexistence of filled and empty NTs; (b) frequent occurrence of hollow NTs; (c) continuous nanowires of Pt inside some NTs.

The reason for the unevenness in filling states could relate to the unequal states of template fibers. Possibly due to the formation of defects during the crystal growth, different phases and forms of the template fibers might have been produced. For example, single crystals of $\text{Pt}(\text{NH}_3)_4\text{CO}_3 \cdot \text{H}_2\text{O}$ were cultivated by solvent vapor diffusion in C. Hippe's work [1], which has a completely different diffraction pattern from the commercial salt, $[\text{Pt}(\text{NH}_3)_4](\text{HCO}_3)_2$. Different phases of templates have different densities, which lead to the different filling states of tubes. Moreover, hollow fibers of the metal salt (Figure 4.1C) have been observed beside solid ones, and hence the formation of empty NTs is explainable. Note that some empty NTs are close-ended, so the solid Pt templates for them must have a low density, which diffuse evenly into the SiO_2 walls and/or immigrate through the porous SiO_2 walls during the calcination.

From the selected area electron diffraction pattern shown in Figure 4.6, the crystallinity of the Pt particles is confirmed while the SiO_2 is proven to be amorphous. The observed reflections agree perfectly with those of face-centered cubic platinum metal. The ring pattern comprising weak spots indicates that the grain size of Pt particles is in the nanometer range or below.

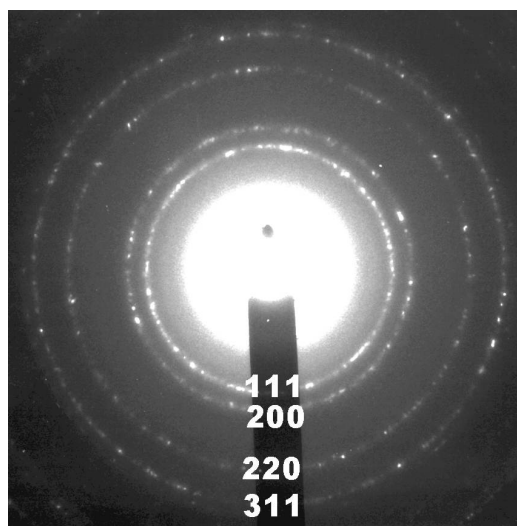


Figure 4.6 Selected area electron diffraction (SAED) pattern of Pt-containing SiO_2 NTs. The reflections are generated by nanocrystalline Pt and are indexed accordingly. The measured d-values ($d_{111} = 2.28 \text{ \AA}$; $d_{200} = 1.95 \text{ \AA}$; $d_{220} = 1.37 \text{ \AA}$; $d_{311} = 1.18 \text{ \AA}$) agree well with the theoretical ones for fcc Pt ($a = 3.944 \text{ \AA}$, PDF 4-836).

The crystallinity and distribution of Pt particles are further exhibited with the HRTEM investigation of a tube wall as shown in Figure 4.7. The single-crystalline characteristic of a randomly chosen Pt particle is indicated by the presence of lattice fringes depicted in the inset, which corresponds to planes of the type $\{111\}$ [7]. From the interior of tube to the exterior, both the concentration and the grain size of Pt particles are decreasing. Close to the inner surface of the NT, rather large Pt particles with diameters of approximately 5 - 15 nm appear. Smaller Pt particles with diameters of approximately 1 - 2 nm are embedded in the silica matrix and distributed in the whole tube wall. Pt particles on the outer surface of SiO_2 NTs have been scarcely observed. The indications are that the Pt particles are rather mobile during the calcination process and also the SiO_2 walls are porous materials.

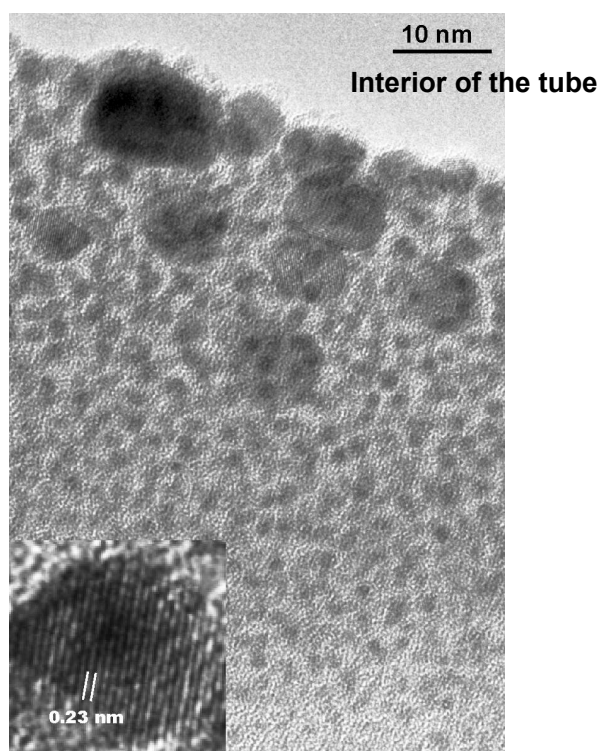


Figure 4.7 HRTEM image of a tube wall. Small Pt particles appear not only at the inner surface (top) but also inside the wall. The inset shows a further magnified Pt particle, with the lattice fringes corresponding to planes of the type $\{111\}$.

4.1.2.2 X-ray Diffraction

The XRD patterns of three different samples, including the Pt templates, template-filled SiO₂ NTs and Pt-containing SiO₂ NTs, are shown together in Figure 4.8 for comparison.

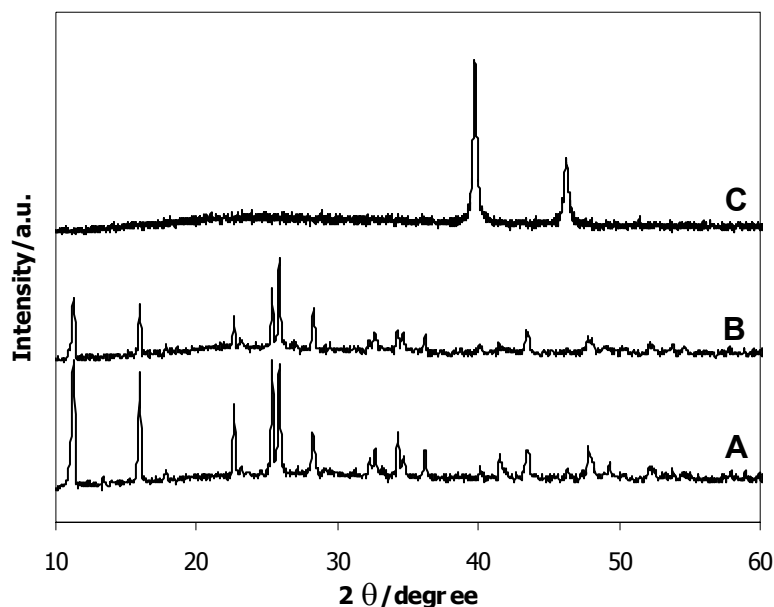


Figure 4.8 XRD pattern of (A) Pt templates; (B) SiO₂ NTs filled with Pt templates; (C) Pt-containing SiO₂ NTs after the calcination at 500 °C for 5 h.

After the coating with amorphous SiO₂ walls, the diffraction pattern of Pt salt (pattern B) is found to decrease slightly in its intensity in comparison with that of the pure sample (pattern A). The reason of this decrease of intensity comes from the decrease of relative amount of the crystalline of Pt salt from 100 wt.% in the former sample to 64.2 wt.% in the latter.

Albeit the presence of amorphous SiO₂ walls in the sample as confirmed by the previous studies with electron microscopy, it is noteworthy that the broad peak in the range of 20 - 30° (2θ), characteristic for amorphous materials (amorphous SiO₂ [8]), is not apparent for the sample of SiO₂ NTs filled with Pt templates. From the XRD investigation previously reported in section 4.1.1.2, it is known that the pure Pt templates exhibit a good crystallinity. Possibly due to the strong diffraction from the crystals of Pt salt, the broad peak of amorphous SiO₂ is rather insignificant with a low relative intensity. Instead, pure SiO₂ NTs synthesized with the

templates of $V_3O_7 \cdot H_2O$, possessing similar dimension of 50 - 300 nm in diameter as our sample but exhibiting less diffraction intensity, showed out this broad peak clearly in the powder pattern [9].

Comparatively, the same sample after heat treatment at 500 °C shows the identical diffractogram of metallic Pt (pattern C), where the broad peak of amorphous SiO_2 in the region of 20 - 30° is highly suppressed by the strong diffraction peaks of Pt. The broad X-ray diffraction peaks are in consistent with the small sizes of metallic Pt particles in the low range of nanometer. As pronounced by the HRTEM image of an individual tube wall (Figure 4.7), Pt nanoparticles were highly dispersed inside silica matrix after the heat treatment.

From the powder pattern, the Pt particles are around 16 nm as calculated with Scherrer equation. But the size distribution of Pt particles in this sample was approximately counted as 2 – 30 nm in TEM [5]. Here the application of Scherrer equation is limited due to the big size distribution of Pt particles.

4.1.2.3 Thermogravimetric analysis and Infrared spectroscopy

The behaviour of thermal decomposition of the SiO_2 NTs filled with Pt templates has been studied by TG and DTA analysis as shown in Figure 4.9 (black line). The heating rate was designed as 5 °C/min in order to be close to the situation of calcination. For comparison, the corresponding behaviour of the commercial Pt salt is listed together (grey line).

In general, the TG curve of the sample of SiO_2 NTs in Figure 4.9A has four steps at 50 – 500 °C. The slope of the curve is highest between 150 - 200 °C. Concretely speaking, the weight loss started at 50 °C, happened most acutely in the range of 150 - 200 °C and slowed down in the range of 200 - 300 °C. Afterwards there is a slowly but lasting weight loss till the temperature approaches 500 °C. In the first run of heat treatment, the weight loss is about 23%. Another three runs of heat treatment till 800 °C were carried out, without causing any significant weight loss. The indication is that the decomposition of the template-filled SiO_2 NTs under the heat treatment till 500 °C has been mostly completed.

By analysing the TG curve of the commercial Pt salt, weight loss happened in two steps: 37% at 190 – 255 °C and 12% at 255 – 310 °C, which should be corresponding to the following reactions in sequence:

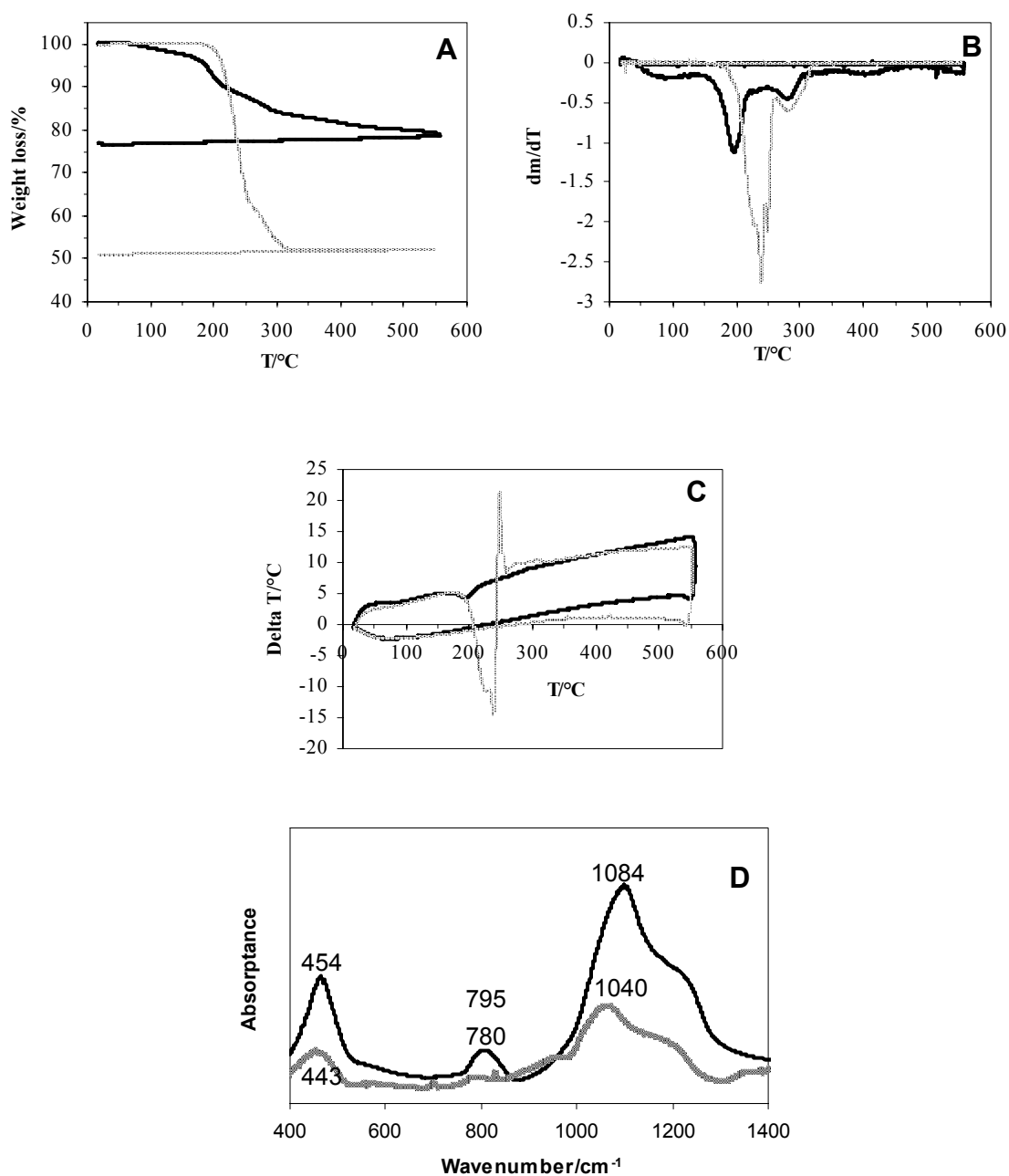
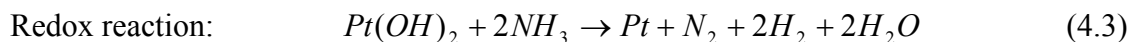
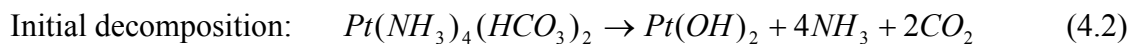


Figure 4.9 (A) TG curve, (B) DTG curve and (C) DTA curve of the template-filled SiO₂ NTs (black line) and the commercial Pt salt as a contrast (grey line). (D) IR spectrums of the sample of SiO₂ NTs before (grey line) and after (black line) heat treatment in its thermal analysis. The annotations are corresponding to the wavenumbers of peak positions.



By comparing the two TG curves, it can be learned above all that the low amount of weight loss after 300 °C should come from the SiO₂ coating, perhaps due to the residual water or solvent molecules in the micropores and the dehydration of Si-OH groups around 400 °C.

From the DTG curve of the sample in Figure 4.9B, its weight loss is clearly observed to have four processes in the range of 50 - 120 °C, 140 - 250 °C, 250 - 310 °C and 370 - 450 °C, centered at 93 °C, 198 °C, 290 °C and 410 °C in sequence. The two processes in the middle should come from the Pt templates. Interestingly, compared with the commercial Pt salt, the peak centered at 238 °C (initial decomposition) of the SiO₂ NTs has an obvious shift of 40 °C to lower temperature. Instead, for the other peak of commercial Pt salt at 290 °C (redox reaction), no shift is observed. The reason behind this shift is attributed to the nanometer size and in turn the large surface area of the Pt templates in the SiO₂ NTs, whereas the commercial Pt salt contains particles in the micrometer regime. This size effect has influence on the initial decomposition, but no apparent effect on the redox process.

In the DTA curve of the sample in Figure 4.8C, a weak and broad endothermic band is observed in correspondence with the thermogravimetric effect in the range of 50 - 300 °C. This band is composed of a broad peak positioned near 200 °C (related to the initial decomposition of the Pt templates) and two shoulders on both sides of it. No thermal effect above 300 °C is obvious. Consistent with the DTG curves, there is a shift to low temperature for the SiO₂ NTs compared with that of the pure commercial Pt salt as well.

Furthermore, the sample was subjected to IR measurements. The IR spectra before and after the heat treatment are plotted as grey line and black line in Figure 4.9D respectively. The three highlighted positions are characteristic peaks for amorphous SiO₂. The peaks near 1100, 800 and 450 cm⁻¹ are assigned to the asymmetric stretching of SiO₄ tetrahedron, the symmetric stretching of SiO₄ tetrahedron and the Si-O-Si bending respectively [10]. It can be observed that the SiO₂ absorption peaks of the template-filled sample have an obvious shift to lower energies (especially the asymmetric stretching of SiO₄ tetrahedron being up to 44 cm⁻¹) relative to the metal-containing sample. Besides, for the SiO₂ NTs filled with Pt templates, there are an absorption band resulting from deformation vibration in a water molecule at 1595

cm^{-1} and an absorption band of carbonate at 1378 cm^{-1} . After the heat treatment in the thermogravimetric analysis, both absorption peaks disappeared.

The interaction between the templates and the SiO_2 walls, i.e. the hydrogen bonding and/or the electrostatic interaction formed between $[\text{Pt}(\text{NH}_3)_4]^{2+}$ and silanol groups on the wall surface, could account for the shift of the characteristic IR absorption peaks of amorphous SiO_2 . In the sample after the heat treatment, the templates have been reduced into metallic Pt particles dispersing in the SiO_2 matrix and hence this interaction does not exist anymore. The dehydration of Si-OH groups during the heat treatment could also contribute to the shift, but with a much less pronounced effect. On the other side, from this shift of IR absorption peaks, it can be deduced that the interaction between the template and the SiO_2 wall should be to a great extent some specific forces other than the van der Waals forces, since the latter exist ubiquitously and make no difference of valent states and kinds of compounds. Further discussions about the interaction will be given in the next section.

4.1.2.4 Coating process

In order to interpret the coating mechanism of TEOS on the surface of the template, understanding of the fundamentals of the adsorption process and sol-gel chemistry are required.

At first, the structure-directing effect of the Pt templates has been examined with a blank test, whereby the same prescription procedure was followed as the general route except for an absence of the templates. It was observed that the blank test sample was still transparent and colourless after 12 h stirring. Observed under SEM, it looks like cracked membrane deposited on the sample holder. The amorphous product, compared with the regular morphology of 1D nanostructures, could be ascribed to the sols formed following the hydrolysis and condensation of TEOS, since the reaction time, 12 h, was relatively short to form a gel (a global rate of condensation, k_c , is $10^{-4} \text{ M}^{-1} \text{ s}^{-1}$ for TEOS [11]). Based on the experimental facts, a preliminary conclusion could be made that the amine group in the Pt templates can increase the condensation rates of metal alkoxides, acting as a catalyst.

As discussed in section 2.2.4, the stability of silica sol does not obey DLVO theory since it is apparently stabilized by a layer of adsorbed water that prevents coagulations even at the isoelectric point. The presence of non-hydrolyzed cations can reduce the degree of hydration

through ion exchange between the cation and the hydrated SiOH. Due to this assertion, it seems that the sample composition of the templates, i.e. aminoplatinum complex, favoured the coating of silica sols on it. Actually, the composition of the template is not a crucial factor since, for synthesis of SiO₂ NTs, many other feasible templates including Ag nanowires [12,13], peptides [14], V₃O₇ • H₂O [9], possess entirely different compositions and properties. A common feature for all those template methods is the lyophilic surface of the templates, specifically hydrophilic for sols of SiO₂ polymers. The hydrophilic template tends to adsorb molecules existing in the solvent by mainly two kinds of interactions: universal interactions of the London dispersion forces (formerly called van der Waals forces) and specific interactions, including electrostatic and electron donor-acceptor interaction (called hydrogen bonding with water molecules as the medium) [15].

According to the IR observation in section 4.1.2.3, the specific interactions contribute more to the coating of silica sols on the templates than general van der Waals forces. Under the basic condition the silanol anion could act as an electron donor to form hydrogen bonding with the coordinative amine of the central Pt²⁺. On the other hand, an electrostatic interaction between the silanol anion and the complex cation, [Pt(NH₃)₄]²⁺, could also form [5]. Owing to these interactions with the templates, the repulsive electrical double layers on the silanol surfaces are disturbed, thus it could be imagined that a layer of silanol species is formed, being adsorbed on the surface of the templates. The follow-up adsorbates, i.e. silanol species, deposit on the first layer due to their reduced double layers and the -Si-O-Si- bonds are formed by rapid condensations. In this way, the condensation rate of silica sols is increased, that results in the formation of silica walls around the templates.

Attention should also be given to the short-range nature of the specific interactions, i.e. the hydrogen bonding and electrostatic interaction. The intensity of the interactions decreases sharply along with the distance (up to 50 nm according to the wall thickness) to the surface of the template, while the relative contribution of the van der Waals forces increases. Because of the weak forces, flabby walls of silica have been observed around the template when the ratio of TEOS to Pt is as high as 40:1 [6].

4.1.3 TiO₂ nanotubes

Attempts have also succeeded in applying this template method to the preparation of TiO₂ NTs. In this section, firstly a thorough characterization of the as-synthesized TiO₂ NTs is exhibited. Then several factors influencing the synthesis of TiO₂ NTs are introduced and discussed. At last, there are comprehensive discussions about the coating process and the crystallinity of the TiO₂ NTs.

4.1.3.1 Microstructures of TiO₂ nanotubes

The as-synthesized TiO₂ NTs were thoroughly characterized by employing a variety of techniques such as SEM, TEM, EDXS and XRD.

a) Electron Microscopy

The 1D morphology of the sample after drying and calcination was firstly observed by SEM. From the SEM images in Figure 4.10, the tubular structures with rather uniform diameters throughout the sample are evident. In Figure 4.10A, it can be seen that the sample which features 2 – 5 μm in length and 300 - 400 nm in outer diameter. In comparison to the prismatic morphology of SiO₂ NTs (Figure 4.4), the TiO₂ NTs look like round columns. For the two open tubes in image D, the wall thickness is observed to be about 100 - 120 nm, i.e. thicker with respect to the hollow interior than for SiO₂ NTs. Although the interior is rectangular for both open tubes, the outer morphology is round instead, owing to the incompact coating of TiO₂. In addition, the coating process around the template was quite ubiquitous since the sample has a high yield of TiO₂ NTs, without significant by-products.

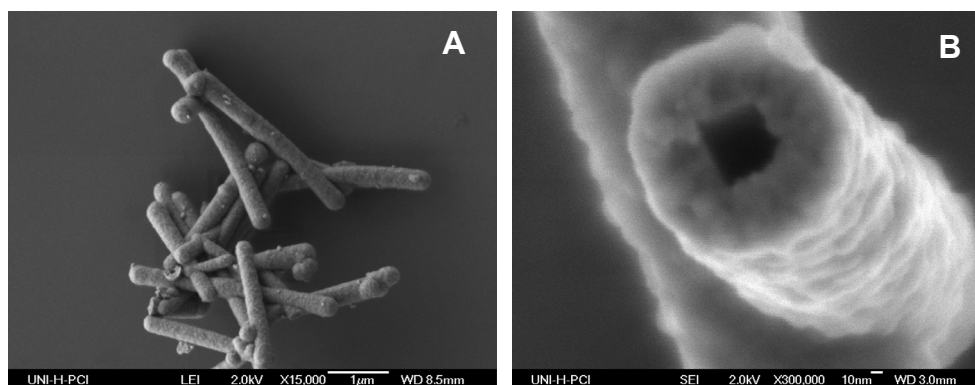


Figure 4.10 SEM images: A) an overview; B) a close observation at a high magnification.

The sample has been further observed by TEM. In Figure 4.11, the tube wall has a thickness about 100 - 150 nm (darker regions), consistent with the observation in Figure 4.10B. The tube length is up to 6 μm . Compared with that of SiO_2 NTs (Figure 4.4), the TEM image of TiO_2 NTs is different in two aspects. One is the darker wall of tube, which is related to the higher electron scattering potential of TiO_2 compared with that of SiO_2 . The other is the absence of black Pt particles being observed repeatedly in the SiO_2 sample. With this TEM image, it is restrained to determine whether the Pt particles are present or not inside the tubes. In Figure 4.11B, the close-up of the wall of a TiO_2 tube is shown. The black points correspond to the Pt nanoparticles with sizes of approximately 3 nm. It is very rare to observe particles as large as 100 nm. Since they are highly dispersed inside the TiO_2 matrix, the Pt nanoparticles are not observable in Figure 4.11A.

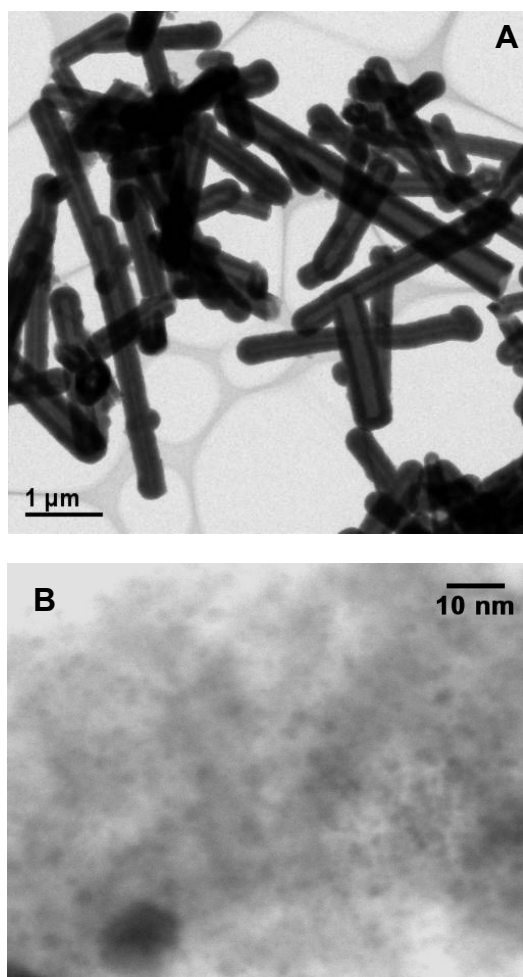


Figure 4.11 TEM images of (A) an overview of the TiO_2 NTs calcined at 500 $^\circ\text{C}$; (B) A close-up of the wall of a TiO_2 tube.

b) Element analysis with Energy Dispersive X-ray Spectroscopy

The presence of Pt element is ensured with the EDXS result shown in Table 4.1. The measured percentage of Pt in weight, 28.885%, is slightly lower than the calculated value, 32.773%, with a corresponding deviation of 11.9%.

The discrepancy could be ascribed to either the experimental error from the measurement of 22 μl TBOT with a pipette having the lowest measure limit as 10 μl during the synthesis, or an uneven distribution of Pt element throughout the sample, or both of them.

Table 4.1 Element analysis of TiO₂ NT (Pt/TBOT=1:5, calcined at 500 °C) with EDXS

Spectrum No.	C wt. %	O wt. %	Ti wt. %	Pt wt. %
Spectrum 1	6.09	30.94	33.33	29.64
Spectrum 2	6.37	33.26	32.24	28.13
Average	6.23	32.1	32.785	28.885

c) X-ray diffraction

The XRD powder pattern A shown in Figure 4.12 tells us that the fresh product directly after the sol-gel process is amorphous with essentially no diffraction peaks. The possible reason will be elaborated in the discussion part of section 4.1.3.3.

The sample obtained after the calcination at 500 °C (pattern B) can be assigned to rutile phase of TiO₂. The size distribution of polycrystalline rutile is around 5 nm according to Scherrer equation mentioned in Section 3.2.2.1 of Chapter 3. This result is consistent with previously reported observation of TEM, whereby Pt nanoparticles of 1 – 3 nm are highly dispersed in this sample. The particles are too small to give reflections. The state of Pt in the current sample calcined at 500 °C is regarded as being amorphous.

When the calcination temperature is further increased up to 700 °C (pattern C), the diffraction peaks of rutile TiO₂ (annotated as *) are narrower and stronger, indicating the increase of both the amount and the size (ca. 10 nm, according to Scherrer equation) of rutile nanoparticles in the sample. What attracts more attention is the appearance of additional strong peaks annotated as •, which agree well with the diffractogram of crystalline Pt. Therefore the previous Pt nanoparticles (1 – 3 nm, counted in TEM) has aggregated and crystallized into bigger particles (ca. 20 nm, according to Scherrer equation) during the

calcination at 700 °C.

Based on the results of powder XRD, it is clear that the crystallization of Pt in the TiO₂ sample is more difficult than that in the SiO₂ sample. Further elaboration will be carried out in the part of discussion (section 4.1.3.3).

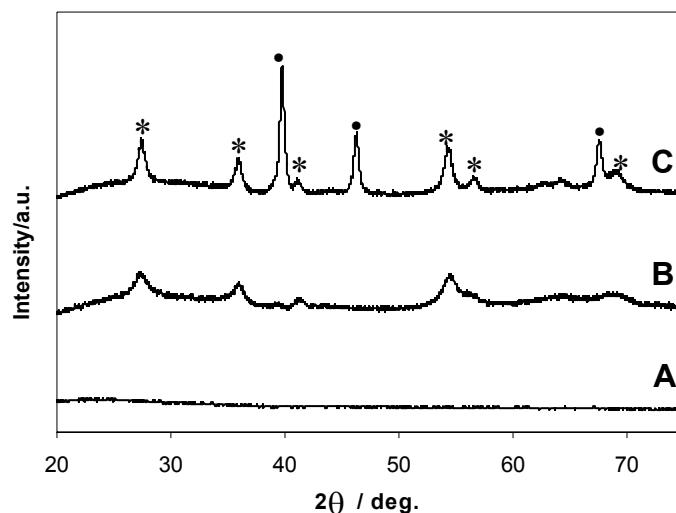


Figure 4.12 XRD patterns of TiO₂ NTs: A) as-synthesized; B) 500 °C for 5 h in air; C) 700 °C for 5 h in air. On the patterns peaks annotated with * belong to Rutile and those with • belong to Pt.

4.1.3.2 Influences of reaction parameters

In comparison with the case of SiO₂ NTs, the coating with TBOT on the template surface appeared much more difficult than TEOS, due to the much faster hydrolysis and condensation speed of TBOT at the presence of the template and the large quantity of water. Although as demonstrated above the synthesis of TiO₂ NTs has been successfully achieved, the demand of painstaking control over the synthesis procedures caused a lower reproducibility of complete coatings of TBOT on the template than for TEOS. Several parameters are very sensitive for the synthesis of TiO₂ NTs, such as temperature, pH value, and the addition of Diethylene Glycol (DEG). With illustrations of SEM investigations, the roles of these parameters will be discussed below.

a) Role of cooling

From viewpoints of reaction kinetics, in order to decrease the reaction rates of TBOT, measures like decreasing the reaction temperature and the concentration of reactant are

generally employed. In a typical synthesis, TBOT was diluted with ethanol to ca. 0.025 mol/L. On the other hand, the temperature was decreased to $-70\text{ }^{\circ}\text{C}$ [1].

While keeping other parameters constant, the mixing of the template suspension, the TBOT solution and the consequent sol-gel process were carried out at different temperatures. As shown in Figure 4.13, the image A, B and C were samples prepared at $-70 \pm 5\text{ }^{\circ}\text{C}$, $-30 \pm 5\text{ }^{\circ}\text{C}$ and $0\text{ }^{\circ}\text{C}$ respectively. Most of the components in sample A are 0D nanoparticles, which could be attributed to the TiO_2 particles yielded from the part of TBOT which has not been successfully coated on the templates. Instead, the sample B prepared at the relative high temperature, $-30 \pm 5\text{ }^{\circ}\text{C}$, comprises only 1D nanostructures. The sample C prepared at $0\text{ }^{\circ}\text{C}$ has a lower yield of 1D nanostructures than the case of $-70 \pm 5\text{ }^{\circ}\text{C}$.

From these comparisons, the effect of cooling on the coating of TBOT is obvious: too much cooling could lead to a too slow deposition rate of TBOT on the template. Before the complete coating is achieved, the forthcoming warm-up in air might accelerate the condensation among TBOT monomers and thus result in the formation of particles. On the other hand with an insufficient cooling (sample C prepared at $0\text{ }^{\circ}\text{C}$), at first the hydrolysis of TBOT and then the condensation among TBOT monomers might have been reached before any significant deposition on the surface of the template. The experimental facts show that a 3-hours-long cooling at $-30 \pm 5\text{ }^{\circ}\text{C}$ is adequate for the sufficient coating, hence it is chosen as a constant in the following experiments.

b) Role of DEG / TBOT molar ratio

From Figure 4.13, the effect of adding diethylene glycol (DEG) to the TBOT/ethanol solution can also be observed by comparing the case with DEG in image C and the case without DEG in image D. Apparently, the yield of TiO_2 NTs is much higher in the sample C than in the sample D. It must be pointed out that, although sometimes a complete yield of TiO_2 NTs could also been achieved without DEG, this chance is much less than the case with DEG. Therefore, the presence of DEG is advantageous for the synthesis of TiO_2 NTs.

Glycol is usually employed as a stabilizer to greatly reduce the hydrolysis rate of titanium alkoxides [16, 17]. The working mechanism is mainly about formations of glycolates or mixed alkoxide/glycolate derivatives as shown in the reactions below (with ethylene glycol as an example):

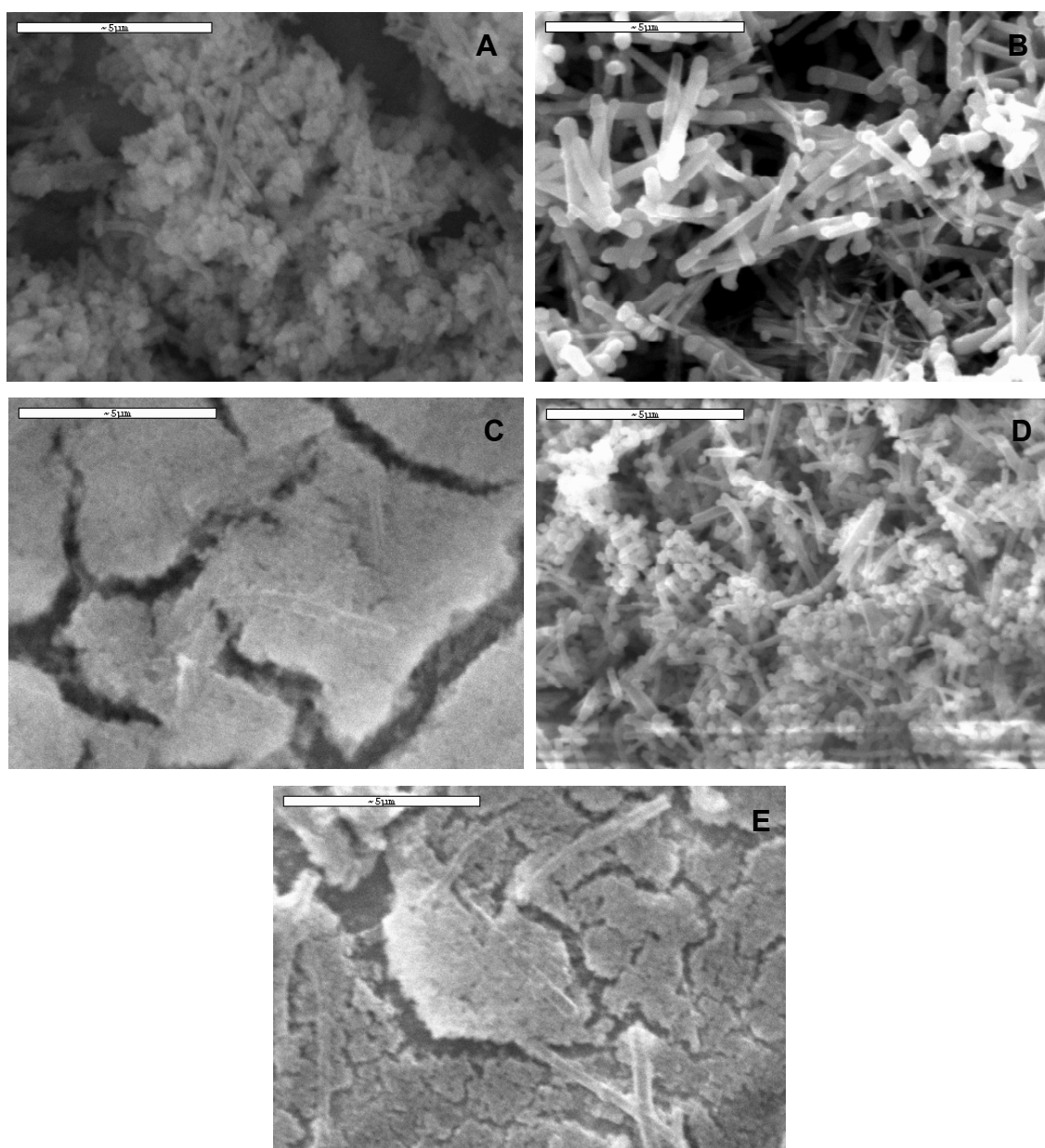


Figure 4.13 SEM images of samples prepared at different parameters listed in the sequence of temperature, ratio of DEG/TBOT, pH value: A) -70 ± 5 °C, 7:1, 10.40; B) -30 ± 5 °C, 7:1, 10.40; C) 0 °C, 7:1, 10.40; D) -30 ± 5 °C, 0, 10.40; E) -30 ± 5 °C, 7:1, 10.00. The bar in every image is 5 μ m.



It has been reported that the glycolated precursors are more resistant to hydrolysis than titanium alkoxides, and could be kept in air for several months without observing any precipitation from the solution [18].

Moreover, it is necessary to mention that an increase of tube thickness of TiO₂ NT is obvious when DEG is added (300 – 400 nm) in comparison with the case without DEG (ca. 100 nm). The presence of residual DEG in the tube wall after the coating should be responsible to that increase. Further efforts will be engaged in BET measurements to calculate the specific surface area of TiO₂ NTs with and without the addition of DEG.

c) Role of the pH value of ammonia solution

Another parameter meaningful for the complete deposition of TBOT on the template is the pH value of ammonia solution. From the comparison of sample C (pH = 10.40) with sample E (pH = 10) in Figure 4.13, it could be concluded that the pH value of ammonia solution has an influence on the yield of TiO₂ NTs: 100% in sample C and ca. 10 % in sample E. Reproduced experiments confirmed the influence of pH value on the coating: only trace amount of tubes were produced as the case in sample E. At a higher pH value, 10.64, the appearance of the product was similar to sample E, only with a slightly different yield of NTs. That means the optimum pH range is very narrow for the preparation of TiO₂ NTs.

A basic catalyst like ammonia solution was supposed to activate both the hydrolysis and the condensation of TBOT [19]. However, there was no specific study on this effect. Actually, it is proven here that the reaction rate of TBOT is not in direct proportion to the pH value of ammonia solution because at the lower value, i.e. 10, hydrolysis and/or condensation of TBOT should be faster than that at the higher value, i.e. 10.40, based on the lower yield of NTs in the former case.

4.1.3.3 Discussion

a) Coating of TBOT on the templates

In analogy to the coating of TEOS, a blank test was also carried out for the coating of TBOT, i.e. an experiment with the same prescription as the synthesis of TiO₂ NTs except the absence of the templates.

Compared with the case of TEOS, the blank test sample was somewhat opalescent. That is reasonable because of the several orders of magnitudes higher rates of hydrolysis and condensation of TBOT in comparison with TEOS. However, it is a stable sol, without visible precipitates even after being deposited in air for 1 day. A gel-like network could only be

observed after being deposited in air for at least 2 days.

In comparison, with the presence of the templates, the precipitation happened frequently if great care has not been taken during the synthesis of TiO₂ NTs. If kept in stillness, the resultant mixture departed as a clear solution in the upper part and a white sediment in the lower. Neither sol nor gel could be formed.

Based on these experimental facts, it is clear that the presence of Pt templates can increase the rate of coating of TBOT with the same coating mechanism as that of TEOS (section 4.1.2.4).

b) Crystallinity of the TiO₂ nanotubes

As for the crystallinity of the TiO₂ NTs, there are three points worth being discussed: the amorphous state of the template-filled TiO₂ NTs, the phase transformation temperature of TiO₂ and the elevation of the crystallization temperature of platinum.

First of all, it is surprising to observe that the Pt templates after being coated with TiO₂ have lost its crystallinity according to the XRD measurement (Figure 4.11A). Neither has the TiO₂ coating exhibited any crystallinity. In comparison, a good crystallinity has been observed for the Pt templates coated with amorphous SiO₂ (Figure 4.7B). Obviously, it is the TiO₂ coating that causes the disappearance of the crystallinity of the Pt templates.

For the amorphous state of the Pt templates coated with TiO₂, a plausible reason could be the highly dispersion of Pt templates inside the TiO₂ coating. Due to the unsaturated coordination of TiO₂ material, strong electron donor-acceptor interactions might have taken place between Ti atom and the N atom in NH₃ and/or O atom in HCO₃⁻ anion of the template, Pt(NH₃)₄(HCO₃)₂. Hence, the Pt templates could have been brought into the TiO₂ matrix as soon as the coating is achieved. Alternatively it could also happen during drying of the powder product due to the increased surface area and free vacancies in the TiO₂ wall after the evaporation of solvent molecules. Both assumptions are in accord with the experimental facts although they are not yet testified.

Secondly, it is noticeable that, after the calcination at 500 °C, a pure rutile phase has been formed (Figure 4.11B) instead of anatase or mixture of them. It is well known that TiO₂ exists in two tetragonal crystalline modifications, a metastable phase, anatase, and a stable phase, rutile. The transformation temperature from anatase to rutile phase of the conventional

polycrystalline or single crystalline titania materials is $>800\text{ }^{\circ}\text{C}$ [20,21]. Evidently, the sample in the current study crystallizes into rutile at a much lower temperature without the formation of anatase.

The size effect of nanomaterials could account for this phenomenon. Due to the decrease in the size of TiO_2 particles, the amount of atoms on the surface increases. Hence when the sample is subjected to the same heat treatment, more stable phase, i.e. rutile phase, is easier to be formed. On the other hand, it could be assumed that the presence of Pt might promote the phase transformation since this process is reported to be very sensitive to dopants, e.g. silicon [22].

Thirdly, when subjected to the same 5-hours-long calcination at $500\text{ }^{\circ}\text{C}$, the Pt templates coated with TiO_2 does not crystallize to metallic Pt (Figure 4.11B), whereas metallic Pt nanoparticles have been detected for the case of SiO_2 (Figure 4.7C). Moreover, when the sample was instead calcined at $700\text{ }^{\circ}\text{C}$ (Figure 4.11C), the X-ray diffraction peaks of metallic Pt appear. Therefore, it could be concluded that the TiO_2 walls have significantly inhibited the crystallization of Pt metal in contrast to the SiO_2 walls. Bearing in mind that the content of Pt inside the NTs is as high as 19.6wt.%, it is amazing that Pt could keep its amorphous state without aggregation and crystallization.

Two reasons can account for this inhibiting effect of TiO_2 walls on the crystallization of Pt metal. Firstly it could be explained by the encapsulation of the Pt metal particles by a reduced TiO_x overlayer [23]. The encapsulation layer is reported to have two atomic layers of a Ti-O film on top of Pt clusters, which is highly strained and forms a dislocated network [24]. Hence, the Pt clusters are highly dispersed instead of being aggregated to form observable crystals. Secondly, although no charge transfer occurs on stoichiometric TiO_2 , $\text{Ti}^{3+} \rightarrow \text{Pt}$ local charge transfer is observed on defective TiO_2 [25]. Since the amorphous TiO_2 wall prepared in our study is highly defective, the dispersion of Pt clusters inside the TiO_2 matrix could have been effectively stabilized by this charge transfer. However, at elevated temperature, i.e. $700\text{ }^{\circ}\text{C}$, the thermal mobility of Pt clusters is strongly enhanced, leading to the aggregation of Pt clusters and the further crystallization.

In summary, the unsaturated coordination of TiO_2 might be the origin for the occurrence of all three aspects discussed above on the crystallinity of the TiO_2 NTs.

It is well known that Pt-doped TiO₂ often shows a high photocatalytic activity for various oxidation reactions [26-29]. Platinum deposits on TiO₂ trap photo-generated electrons and subsequently increase the photo-induced electron transfer rate at the interface. On the other hand, they also provide catalytic sites where different mechanistic pathways from those on the naked TiO₂ are enabled [27-29]. For the prepared TiO₂ NTs doped with a large amount of Pt, special applications in photocatalysis are expected.

4.2 Growth mechanism of templates of $[\text{Pt}(\text{NH}_3)_4](\text{HCO}_3)_2$

In this section, attentions have been focused on the detailed observation of the morphology of the template and the possible formation mechanism, by varying several parameters including the temperature, rate of ethanol addition, concentration of the mother solution (the aqueous solution of the Pt salt) and ratio of ethanol (added in order to precipitate the template NFs) to water. The experimentally established formation mechanism of the templates does contribute to and meanwhile is proven by the controlled growth of silica NTs. In combination with knowledge in fields of the sol-gel technique and the crystal growth, the experimental facts were discussed reasonably. Scanning Electron Microscopy (SEM) was the main tool for the sample characterization in this study.

4.2.1 Influences of different parameters on the morphology

In this part, the template formation is thoroughly investigated by varying related parameters at the step of precipitation. Hereby the morphology of the template is defined not only as the geometric form of the template but also its size distribution. The goal is to obtain Pt templates comprising of pure NFs with a narrow distribution in diameter.

4.2.1.1 Temperature and rate of ethanol addition

From all images shown in Figure 4.14, one common feature is the preferred 1D morphology of the template, independent of the size distribution. By a simple process of solvent modification, i.e. the adding of ethanol into aqueous solution, the tetraaminoplatinum compound naturally grows into 1D structures, this habit is supposed to be determined by the highly anisotropic bonding in the crystallographic structure [5] similar to asbestos and chrysolite [30]. The crystallinity of the templates has been confirmed by X-ray powder diffraction (section 4.1.1.2), which agrees very well with the pattern of the commercial $[\text{Pt}(\text{NH}_3)_4](\text{HCO}_3)_2$.

The size distribution of the templates depends on the temperature of precipitation to a certain extent. If the two cases shown in Figure 4.14A and 4.14B are compared, it is obvious that the distribution in thickness of the fibers prepared at 0 °C (0.1 - 1.5 μm) is narrower than that

prepared at room temperature (RT) (0.1 - 3 μm), while the length of the nanometer-thick fibers (NFs, thickness in 50 – 1000 nm) is shortened from $>10 \mu\text{m}$ at RT to ca. 5 μm at 0 $^{\circ}\text{C}$.

The narrower distribution in thickness can mainly be ascribed to the downsizing of the micrometer-thick fibers (MFs, thickness in 1 – 3 μm) with the decreasing temperature. This downsizing fact could normally be a result of smaller sizes of nuclei at lower temperature. However, less aggregation of NFs seems to be more responsible (section 4.2.2). The relative decrease in length could be ascribed to an increase in the number of nuclei at 0 $^{\circ}\text{C}$ than at RT because, with the same precipitating rate, more nuclei would be generated at a lower temperature. Additionally, in both pictures, the rectangular cross-section of the templates could be observed, at this scale of course mainly those MFs.

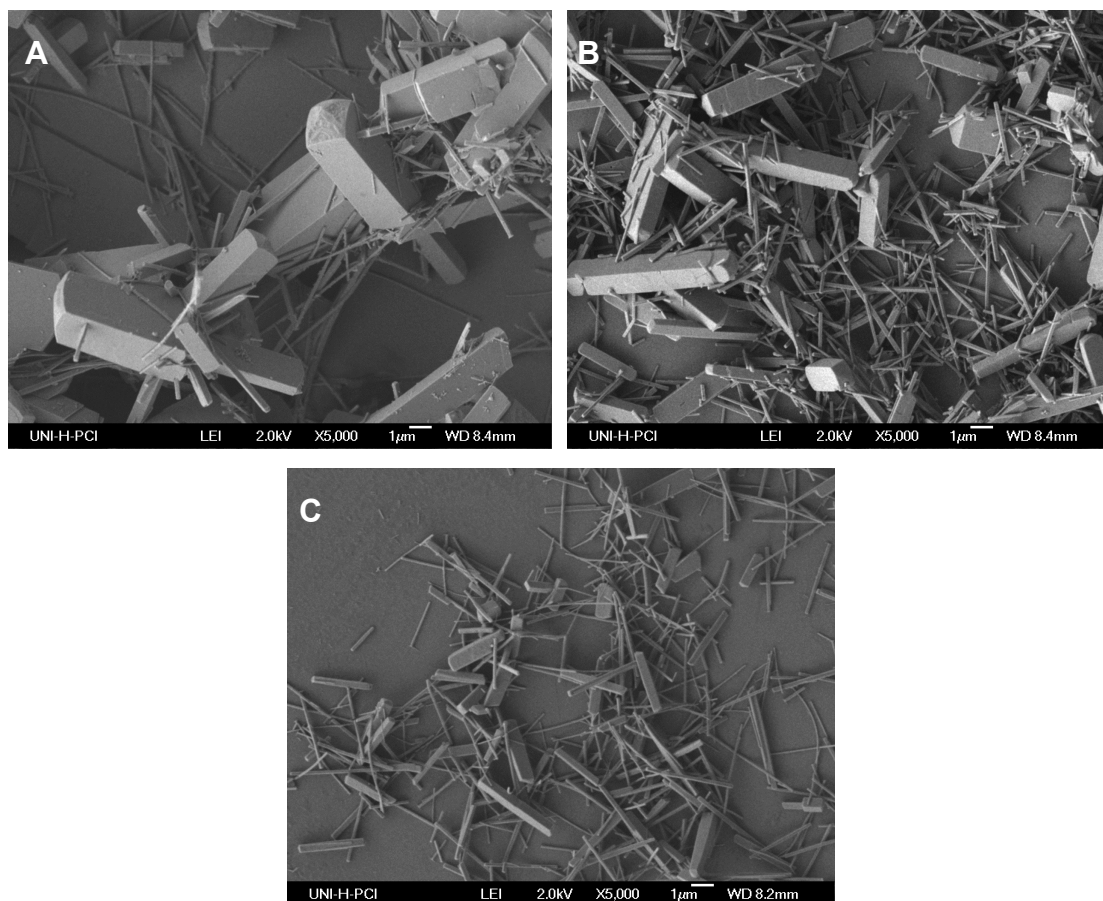


Figure 4.14 Templates prepared at different temperatures and rates of ethanol addition. Parameters listed in sequence were temperature, rate of ethanol addition, Pt concentration of mother solution and ratio of ethanol to water. (A) RT, 0.5 mL/min, 0.0125 M, 10:1; (B) 0 $^{\circ}\text{C}$, 0.5 mL/min, 0.0125 M, 10:1; (C) 0 $^{\circ}\text{C}$, 10 mL/min, 0.0125 M, 10:1.

Even though the drastic effect of the temperature on the size distribution of the templates, it is still infeasible to obtain uniform NFs by further cooling the system, because the aqueous solution system would be frozen not far below 0 °C.

Another effective factor to the size distribution of the templates is the rate of ethanol addition. If other factors are kept constant and the rate of ethanol addition is increased from 0.5 to 10 mL/min, the μm -thick fibers in the template mixture (Figure 4.14B) are replaced by the submicrometer-thick fibers (Figure 4.14C). A plausible reason for that observation will be discussed in section 4.2.2. However, in spite of the further increase of rate of ethanol addition to 1000 mL/min, a broad size distribution, i.e. 50 - 1000 nm in thickness, is still present in the templates, the case of which is similar to Figure 4.14C. Therefore, a different method must be developed in order to obtain uniform template NFs.

4.2.1.2 Morphology dependence on the salt concentration in the mother solution

The study on the morphology of a sample through varying the concentration of the mother solution is intended to prepare templates with a narrow distribution in thickness. For the observation of the sample prepared with the Pt concentration at 0.001 M, the presence of TEOS is a prerequisite to keep the original form of the template, since the pure template prepared at such a low concentration is subjected to a severe deformation in its morphology during the evaporation of solvent on the surface of SEM holder. Therefore, in all cases samples exhibited here are with addition of TEOS in order to make the comparison reasonable.

When the Pt concentration decreased from 0.0125 M (Figure 4.15A) to 0.003 M (Figure 4.15B), the relative amount of NFs in template mixture decreased too, while both the relative amount and the size of MFs increased (the reason will be discussed in section 4.2.2). In addition, trace amounts of 20 - 30 nm particles were observed in both two samples, which could be attributed to Pt/silica clusters formed by rapid condensations of silica sols at the presence of trace amount of electrolyte, i.e. $[\text{Pt}(\text{NH}_3)_4]^{2+}$ and HCO_3^- [31].

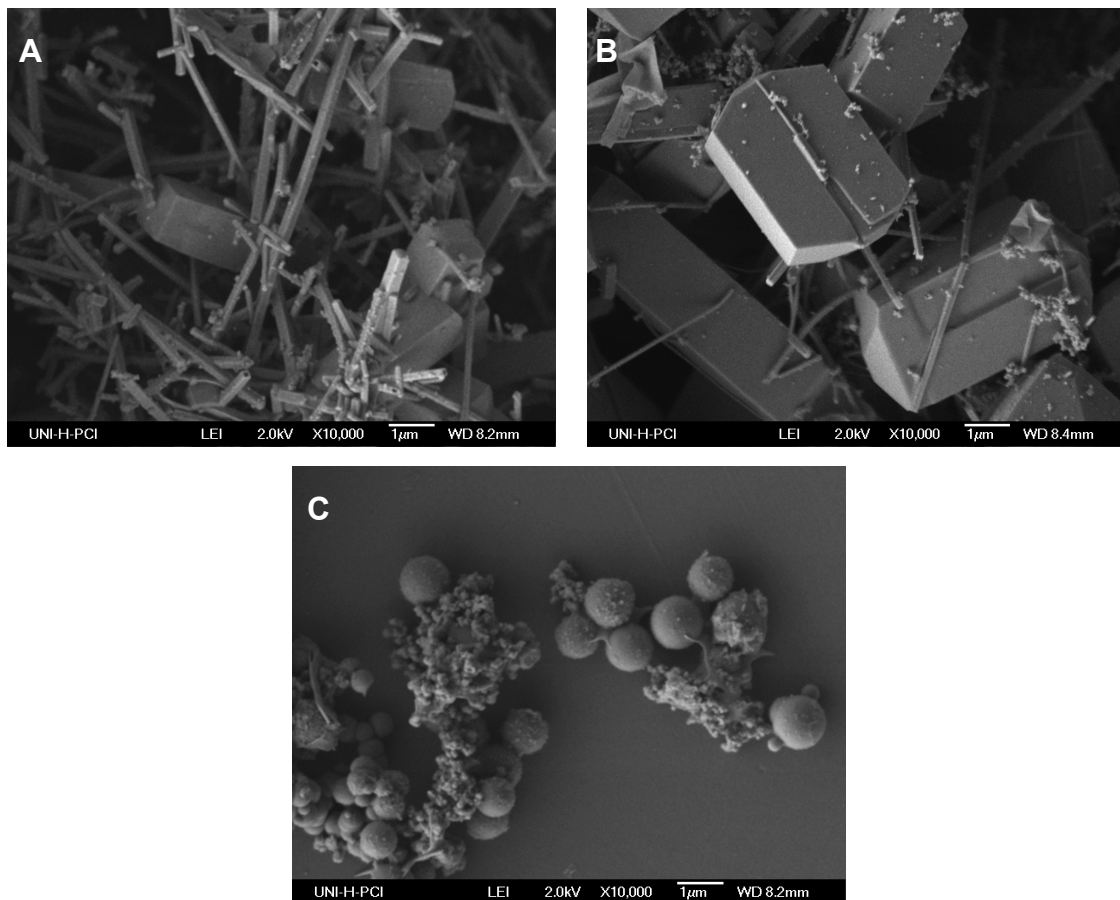


Figure 4.15 Samples prepared with different salt concentrations in the mother solution. Parameters in sequence were temperature, rate of ethanol addition, salt concentration in the mother solution and ratio of ethanol to water. (A) 0 °C, 0.5 mL/min, 0.0125 M, 10:1; (B) 0 °C, 0.5 mL/min, 0.003 M, 10:1; (C) 0°C, 0.5 mL/min, 0.001 M, 10:1.

When the Pt concentration is as low as 0.001 M, the 1D fibers disappear completely (Figure 4.15C), and spheres of silica (0.3 - 1.0 µm in diameter) appear instead, the formation might follow the rule of SFB silica spheres developed by Stöber et al [32]. Hence 0.003 M is a critical value of the concentration in the mother solution, below which 1D fibers of the templates are not obtainable.

Moreover, the amount of small Pt/SiO₂ clusters increased with the decreasing concentration from image A to C in Figure 4.15, because the ratio of dissolved ions increases with the amount of water.

From this part of study, a preliminary conclusion could be made that during the precipitation

the MFs should be formed prior to the preferred NFs, but here it is too arbitrary to argue that there is a clear temporal separation between them. Although the problem, i.e. the broad size distribution of the templates, has not been solved through varying the concentration of the mother solution, relatively higher value of concentration seems to be advantageous to the formation of NFs. In the subsequent study, a salt concentration of 0.0125 M was usually adopted.

4.2.1.3 Bundles of NFs observed at ethanol/water of 1:1

The focus is hereafter put on the formation mechanism of MFs contained in the templates, which could not be removed by varying parameters such as the temperature, rate of ethanol addition or Pt concentration of the mother solution. Attention has been paid to the temporal occurrence of MFs owing to the previously established conclusion about its precedence over that of NFs. Two possibilities could exist, the anisotropic growth of micrometer-thick nuclei or the lateral aggregation of NFs.

The usual procedure to prepare the templates through the solvent diffusion is by adding 10 mL ethanol dropwise but continuously into 1 mL ammonia solution of the Pt salt (the mother solution). The samples of the templates in Figure 4.14 were all prepared after 10 mL ethanol were added, from which only completed morphology of the templates could be observed. In order to catch the moment in-situ during the formation of the templates, the continuous addition of ethanol was interrupted at 1 mL ethanol. Several drops of the precipitate were collected on a sample holder of SEM. It was necessary to blow away the solvent with a dry airflow for the sake of obtaining the original appearance. The break of adding was compelled since, as to the limited amount of precipitates at this low rate of ethanol to water, it took several times of collection till an adequate amount of precipitate was retained on the sample holder.

As shown in Figure 4.16, here again NFs is not the only morphology, instead they are accompanied by bundles of NFs due to the lateral aggregation. These bundles, having a lateral size of 1 - 3 μm , could be classified as the precursors of the investigated MFs. In a close observation in Figure 4.16B, the big bundles have already smooth sides but rather rugged ends. When 10 mL ethanol are added, the rugged ends are smoothed as shown in Figure 4.16C. Referring to the obvious increase in size of MFs as precipitating speed decreases (comparison of

Figure 4.14B and 4.14C), the larger size of MFs in Figure 4.16C than those in Figure 4.14B could be attributed to a delay of precipitation during the interrupted sampling. Moreover, in Figure 4.16C the relative amount of NFs appears to be less than that in Figure 4.14B, very probably due to the consumption of NFs of the formation of bundles.

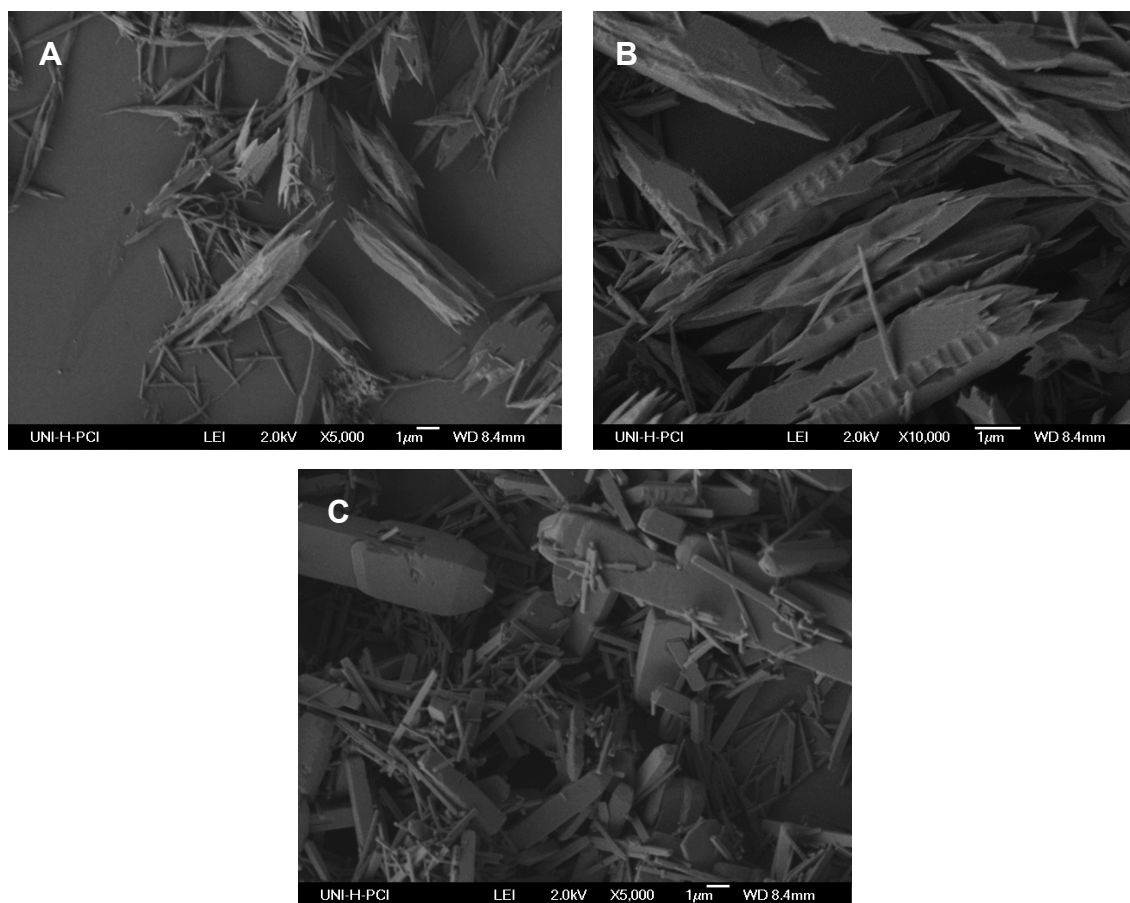


Figure 4.16 Observation of bundles of the template NFs. Temperature was 0 °C. Rate of ethanol addition was 0.5 mL/min. Pt concentration in mother solution was 0.0125 M. (A) Template prepared by interrupting the precipitation and (B) that at higher magnification when the ratio of ethanol to water was 1:1. (C) The same template when the ratio of ethanol to water was 10:1.

4.2.2 Discussion of the formation mechanism of Pt templates

As the template formation mechanism, an illustration is given in Figure 4.17 on the basis of the observations.

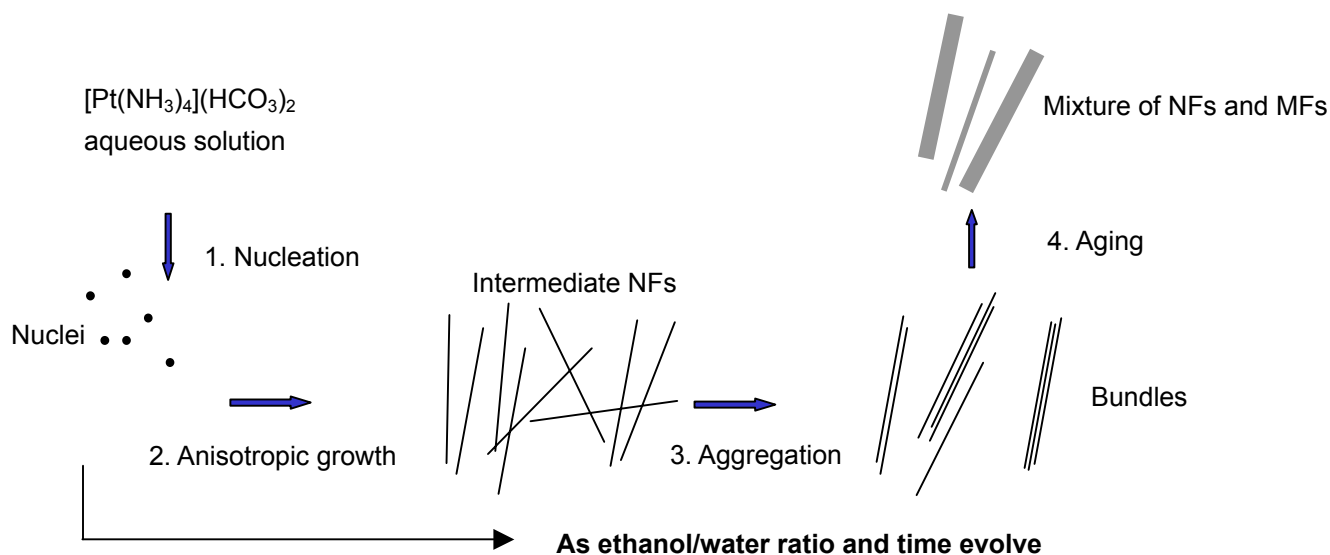


Figure 4.17 Illustration of the formation of Pt templates as time and ethanol volume evolve.

The formation of the Pt templates follows the routine procedures of nucleation and growth. Along with the dropwise addition of ethanol, the aqueous solution is consequently concentrated and further comes to a state of supersaturation due to the insolubility or sparing solubility of the Pt salt in ethanol. Once the concentration of building blocks (ions) becomes sufficiently high, they aggregate into small clusters (nuclei) through a homogeneous nucleation. With the continuous providing of building blocks, the nuclei serve as seeds for further anisotropic growth to form intermediate NFs (50 – 100 nm). However, the intermediate NFs grown at the initial stage do not keep their independency from each other, but feature a strong tendency to aggregate into bundles (being discussed in following paragraphs), resulting in a broader size distribution of the templates (0.1 - 3 μm , approx.). Hereafter, as ethanol/water ratio and time evolve, the rugged ends of bundles disappear at the aging process.

According to the formation mechanism in Figure 4.17, determinative steps are that of nucleation and aggregation in order to obtain monodisperse NFs, whereas for achieving NFs with

high aspect ratios the steps of anisotropic growth and again aggregation are of utmost importance. In combination with the above-given experimental observations, these two aspects will be discussed respectively.

Monodispersity

First as to the topic of being monodisperse, a single burst of nucleation that consumes the excess solute can achieve a single particle size; if new nuclei form during the growth period then a range of sizes results (theory built up by LaMer and Dinegar [33]). Therefore, the size distribution of the templates precipitated at a rate of 10 mL/min (Figure 4.14C) was narrower than that of 0.5 mL/min (fig. 4.14B) owing to the faster nucleation in the former case. Whereas it was still by no means monodisperse since new nuclei could have formed during the further “too fast” growth.

In contrast, slow growth instead lead to another specific problem, i.e. the aggregation of NFs, which resulted in the frequently occurring MFs. Note that the aggregation became more severe (larger size) and frequent (relatively higher content) in the case of Figure 4.16 when there was a temporal delay of precipitation. Therefore, it could be inferred that the adding of ethanol could stabilize the intermediate NFs, or in other words prevent them from the aggregation. Moreover, the case of lower concentration in the mother solution as shown by comparing Figure 4.15A and 4.15B was equivalent to a retarding of the rate of ethanol addition and hence resulted in larger MFs with a higher frequency. Besides the rate of ethanol addition, a lower temperature can also limit the aggregation of NFs as demonstrated in Figure 4.14A and 4.14B.

Bearing in mind all those features of the intermediate NFs, a mechanism accounting for the aggregation of NFs could be deduced. At the transitional stage of ethanol/water ratio 1:1, the surfaces of intermediate NFs were highly hydrated with a large amount of adsorbed water molecules. Accordingly, the system had a high surface free energy that favoured from the view of thermodynamics the minimization of surface area through either the dissolution or, more probable and often observed, the aggregation of NFs once they encountered each other occasionally side by side in the stirred medium. When more ethanol, which replaces water molecules at the surface, was added, the system became stable. In addition, the aging, during which the surfaces of bundles were smoothed or flat-shaped, could also have been driven by such

a thermodynamic force.

High aspect ratio

There are two relevant steps influencing the aspect ratio of NFs: the anisotropic growth and aggregation. In Xia's group, silver nanowires with aspect-ratios up to ~1000 were achieved on the one hand with the presence of poly(vinyl pyrrolidone) (PVP), which possibly adsorbed on the surfaces of silver nanoparticles and prevented them from aggregations, and on the other hand through the slow dissolution of silver particles into the solution [12, 13]. Correspondingly, in our case at room temperature a slow rate of ethanol addition (Figure 4.14A) led to NFs with significantly higher aspect ratios. However, at 0 °C (Figure 4.14B and 4.14C) this effect of the rate of ethanol addition on aspect ratios was not that significant. This indicates that, with respect to the solubility of the Pt salt, the decrease in temperature is equivalent to an increase in the rate of ethanol addition. In both cases, the building blocks were supplied much rapidly and as a result new nuclei could be generated for the growth of new NFs. That is the reason for the formation of NFs with lower aspect ratios in the case of a lower temperature and a faster precipitation.

Although the anisotropic growth was favoured through reducing the rate of ethanol addition, the aggregation of NFs, a negative factor for getting a high aspect ratio, was promoted at a low rate of ethanol addition instead. That aggregation could not be effectively inhibited by varying the concentration as demonstrated in section 4.2.1.2. Other methods like an addition of special adsorbates in order to prevent the aggregation and in turn obtain NFs with high aspect ratios should be tested while keeping a low rate of ethanol addition.

At the end of this part, we can conclude that, for the template fibers prepared from this particular Pt salt by a rapid solvent diffusion, it might be impossible to yield monodisperse ones with high aspect ratios through varying above-mentioned parameters mainly due to the severe aggregation of intermediate NFs. According to the assumed formation mechanism of templates, the experimental observations have been clarified and, furthermore, it showed the pending difficulty to solve.

4.3 Controlled growth of Pt-containing oxide nanotubes

In the controlled growth of Pt-containing oxide NTs, the metal alkoxides were ingeniously employed as both the stabilizers for the anisotropic growths of the Pt templates, and the coating agents to form the tube walls. Monodispersed (100 - 200 nm) SiO₂ NTs with high aspect ratios (100 - 400) have been successfully prepared. For the case of TiO₂, thin (40 - 100 nm) tubes were synthesized with improved aspect ratios (up to 100) in spite of a decreased productivity.

4.3.1 SiO₂ nanotubes with high aspect-ratios

4.3.1.1 Strategy for the controlled growth

The strategy for the controlled synthesis was developed as follows: TEOS was added into the mother solution before the formation of the Pt templates, allowed to undergo a short period of intensive hydrolysis. Afterwards, at an extremely rapid stirring rate (e.g. 1000 rpm) a pulse of ethanol was injected into the already saturated solution. A homogeneous nucleation was induced that lasts also a short period for a “focusing” process [22] of nuclei. Then the stirring rate was decreased to the typical one (e.g. 300 rpm) and a large amount of ethanol was pumped with a rather slow rate of adding into the nuclei-abundant suspension, for the purpose of providing a well-controlled slowly supply of building blocks for the anisotropic growths of template NFs. Because of the presence of hydrolysed TEOS in the suspension, the aggregation of NFs has been prohibited.

4.3.1.2 Monodisperse SiO₂ nanotubes with high aspect ratios

a) Morphology characterization with Electron Microscopy

Reproduced syntheses proved the applicability of this strategy with quality-improved products. After primary optimisation of various parameters, neat product of template-filled SiO₂ NTs, featuring high aspect ratios (Figure 4.18A, 100 - 400) and narrow size distributions (80 - 150 nm in the outer diameters from Figure 4.18B), were obtained.

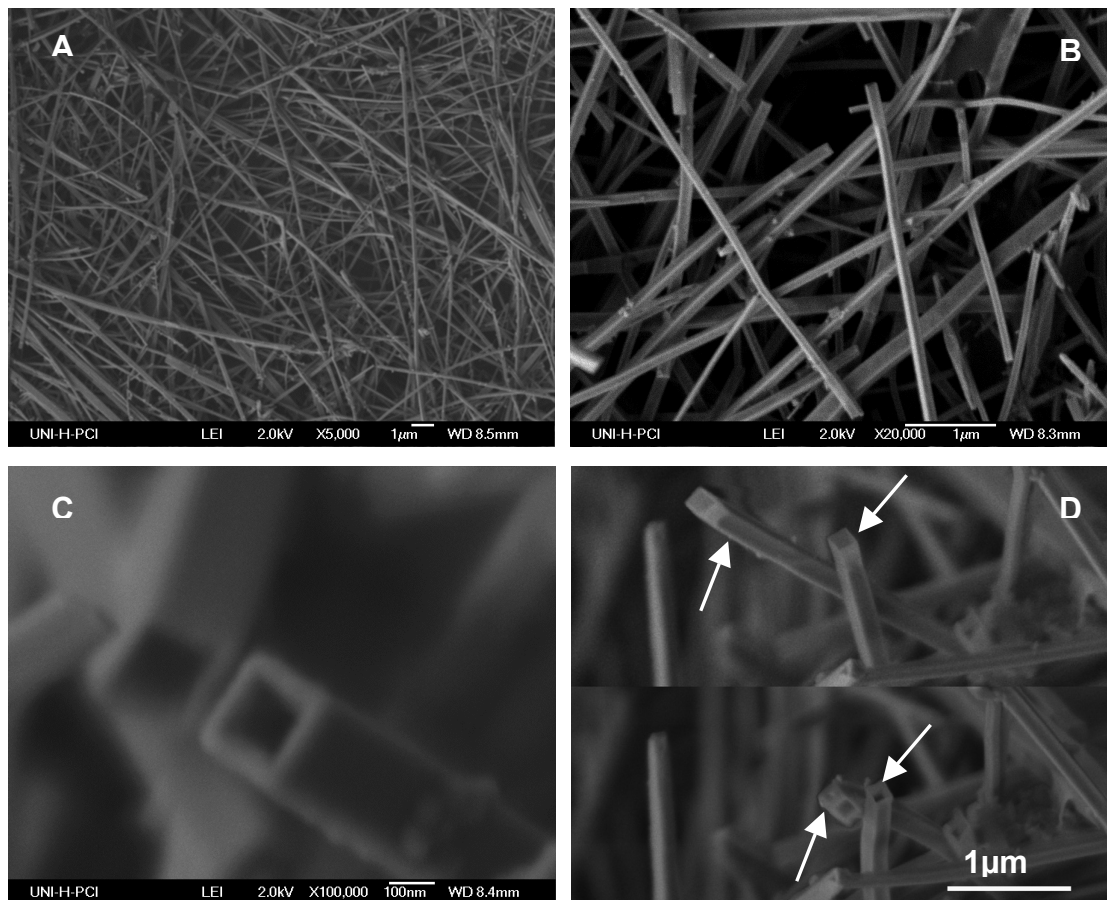


Figure 4.18 SEM of SiO₂ NTs: (A) image showing high aspect ratios at a low magnification; (B) image showing monodispersity at a high magnification; (C) view of open rectangular cross-sections of two NTs; (D) view of a bending process of one open NT under the electron beam.

Surprisingly, compared with the SiO₂ NTs prepared through the normal route (section 4.1.2), the sample is on the contrary comprised of mostly open-ended NTs with rectangular passages when observed at a high magnification as shown in Figure 4.18C. This characteristic morphology possibly originates from the capping effect of TEOS on the specific facets of the template NFs under the well-controlled growth and will be discussed in detail in section 4.3.1.4.

During the SEM measurements, a series of images were made accidentally of the bending of NTs under the electron beam as shown in Figure 4.18D, from which we could conservatively conclude that this kind of amorphous hollow silica material possess certain elasticity even though that is difficult to be quantified.

After the calcination at 500 °C for 5 h in air, the structure-directing Pt templates was reduced and at the end Pt-containing SiO₂ NT was resulted as shown by a typical TEM image in Figure 4.19. Except the reduction in diameter, the inner morphology of this sample is similar to that prepared with the general route. In some cases continuous Pt nanowires could be observed inside the thin NTs bearing an analogy to the former observation (Figure 4.4C). The short length of NTs (1 - 2 μm) might result from a mechanical abrasion during the sample preparation for the TEM measurement.

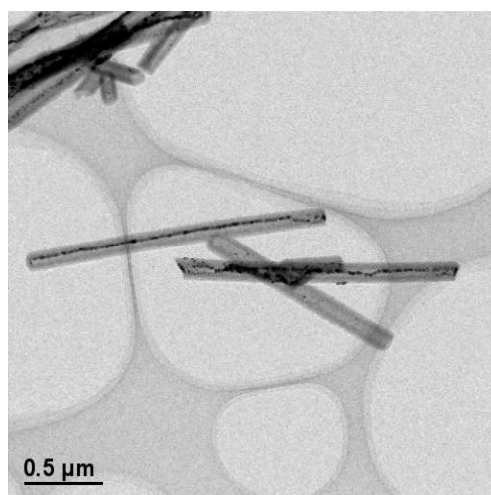


Figure 4.19 A typical TEM image of metal-containing SiO₂ NTs after calcination.

Moreover, the observation of a bundle of open SiO₂ NTs as depicted in Figure 4.20 confirms the authenticity of the formation mechanism of Pt templates illustrated in Figure 4.17. It is the presence of the SiO₂ walls that makes the aggregation of intermediate NFs observable. The relative amount of bundles of NTs in one sample could be varied greatly by changing the pre-hydrolysis time of the capping agent, TEOS. The optimised pre-hydrolysis time was 2 min at 0 °C without significant observations of bundles. When the pre-hydrolysis time was set to 1 min, the amount of bundles was about 50%. The shorter the pre-hydrolysis time, the higher the relative amount of bundles. Further specific studies on this aspect will be carried out in section 4.3.1.3.

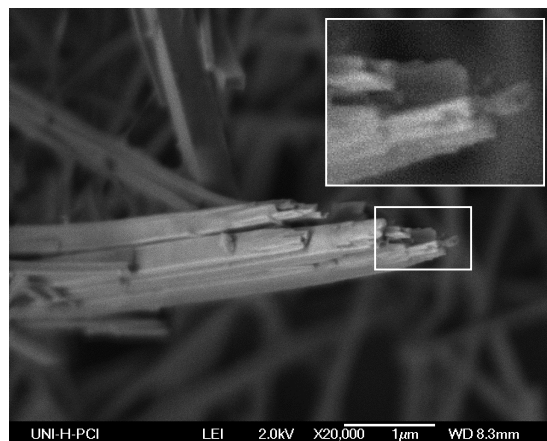


Figure 4.20 SEM image of a bundle of open silica NTs.

b) Specific surface area and pore size distribution by N₂ adsorption

As shown in Figure 4.21A, the N₂ adsorption isotherms on the degassed SiO₂ NTs (200 °C for 16 h, solid circles) and calcined SiO₂ NTs (350 °C for 5 h, hollow circles) are characteristic for mesoporous materials with the presence of hysteresis loops. It can be seen that there is an obvious increase in the pore volume due to the heat treatment. By applying BET equation to the adsorption isotherms, the specific surface area of the degassed sample was calculated to be 48 m²/g and that of the calcined sample was 116 m²/g.

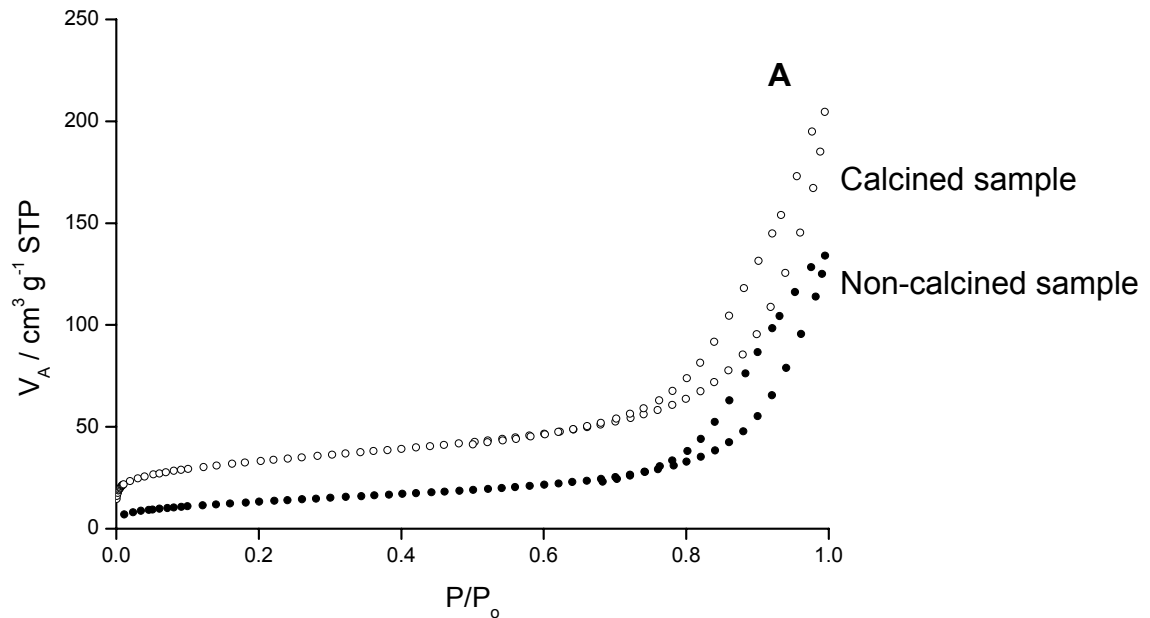
Since the two samples have been degassed at 200 °C for 16 h before the N₂ adsorption, they both have turned from white to black, which indicates that the templates have decomposed and reduced partly during the degassing treatment. Therefore, the increased pore volume and specific surface area of the sample after the calcination at 350 °C for 5 h should be attributed to the further decomposition of the residual Pt templates, the evaporation of water or solvent molecules in the pores of SiO₂ walls and also the dehydration of Si-OH groups. This observation is also consistent with the TG curves in Figure 4.8A, where the weight loss above 300 °C comes from the SiO₂ walls.

From the t-plots in Figure 4.21B, it is clear that there are micropores in the calcined sample (hollow circle), but not in the sample without calcination (solid square). So that the micropores were induced during the calcination at 350 °C through the removal of residual water or solvent

molecules from SiO₂ walls.

To this mesoporous solid, the BJH method can be applied to yield a reliable estimate of the pore size distribution. The pore size distribution of the calcined sample is shown in Figure 4.21C. It is seen that the pores in this material are mostly distributed in the range of 5 - 25 nm, centered at 12.2 nm. The pore size distribution of the sample without calcination (unshown result) is similar to that of the calcined sample. The calculated values should be attributed to the mesopores on the walls of NTs. The hollow cavities of NTs with diameters in 100 - 200 nm act like macropores, which are beyond the applicability to the N₂ adsorption and the BJH method. In order to determine macropores, Hg porosimetry, which is not available in our institute, must be applied.

In summary, there are micropores, mesopores and macropores inside the sample after calcination at 350 °C.



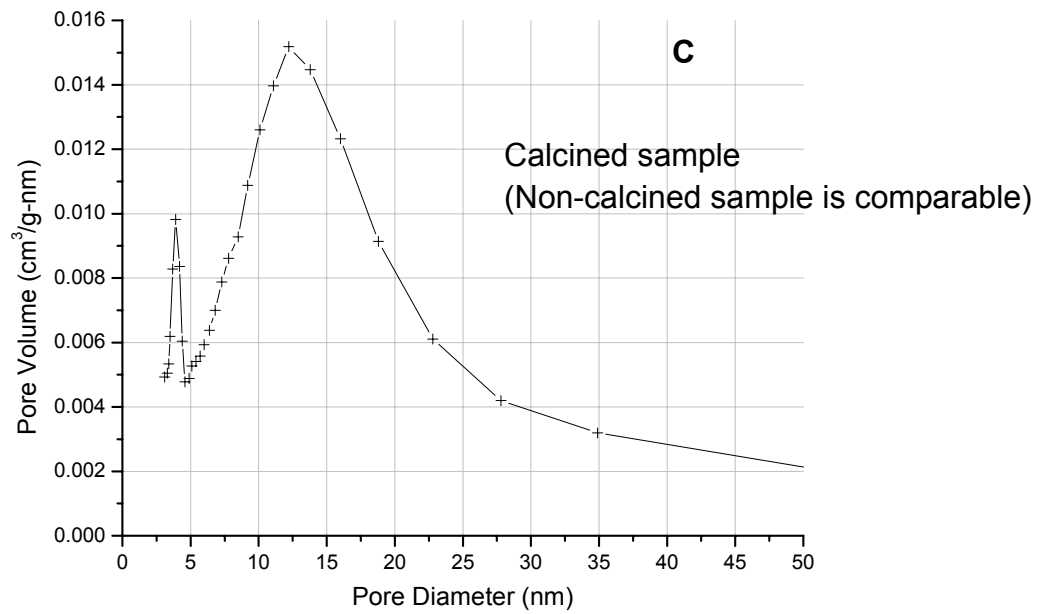
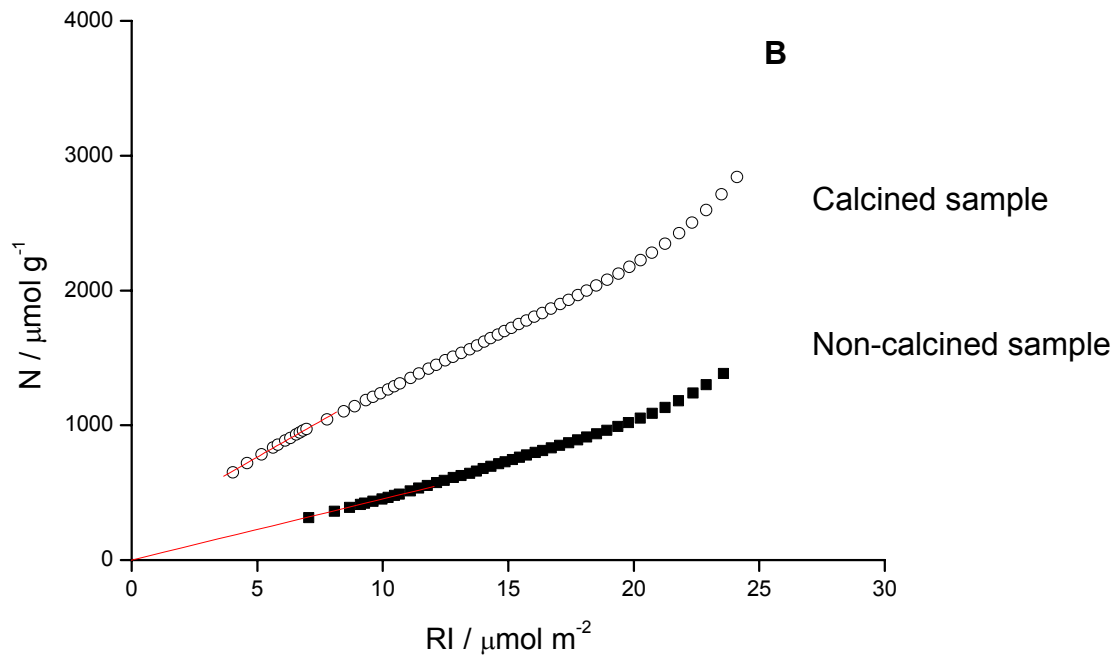


Figure 4.21 (A) N_2 Adsorption isotherms at 77 K, (B) t-plots and (C) pore size distribution of the SiO_2 NTs with controlled growth.

4.3.1.3 Factors influencing the morphology

It was found that the rapid injection of a pulse of ethanol (0.1 mL ethanol) for a homogeneous nucleation was playing a significant role on the morphology of the product. Besides, the morphology of the product also depended greatly on the adding rate of ethanol after the rapid injection.

Two groups of samples were prepared as shown in Figure 4.22. The samples in Group A were prepared with the rapid injection process, while those in Group B were prepared without that process. The subscripts indicate the corresponding rate of ethanol addition (mL/min).

From the SEM images, a great amount of information about the morphology of the product can be collected. Firstly, the three samples in Group A are compared. Apparently, the fibers in sample **A_{0.5}** are most uniform (100 - 200 nm) and rather long (15 - 20 μm), without detectable bundles. Prepared at a lower rate of ethanol addition, sample **A_{0.25}** are composed of fibers up to 40 μm in length and with a cross-section size distribution of 50 - 400 nm. Bundles of NTs can be observed. The sample **A₂**, which was prepared at a faster rate of ethanol addition, has even more bundles inside. So that the optimal rate of ethanol addition is 0.5 mL/min.

The Group B is quite different from Group A. The fibers in sample **B_{0.5}** are also very uniform in diameter, whereas they are greatly reduced in length (5 - 10 μm). The case at a lower rate of ethanol addition, sample **B_{0.25}**, contains also a large amount of bundles. However, there is no observation of bundles in the case of sample **B₂**, being different from sample **A₂**.

In order to make a clear comparison, these results are summarized in Table 4.2. Three parameters are employed to describe the morphology of the product: the distribution of NTs in diameter, length of NTs and relative amount of bundles. From Table 4.2, it can be concluded that the sample has a narrowest size distribution when the rate of ethanol addition is 0.5 mL/min. The length of NTs increases when the adding rate of ethanol decreases. The rapid nucleation process is also advantageous to grow longer tubes. Both the rate of ethanol addition and the rapid nucleation process influence the formation of tube bundles. In order to produce uniform NTs without the formation of bundles, an adequate adding rate of ethanol should be adopted, i.e. 0.5 mL/min, together with the rapid nucleation process.

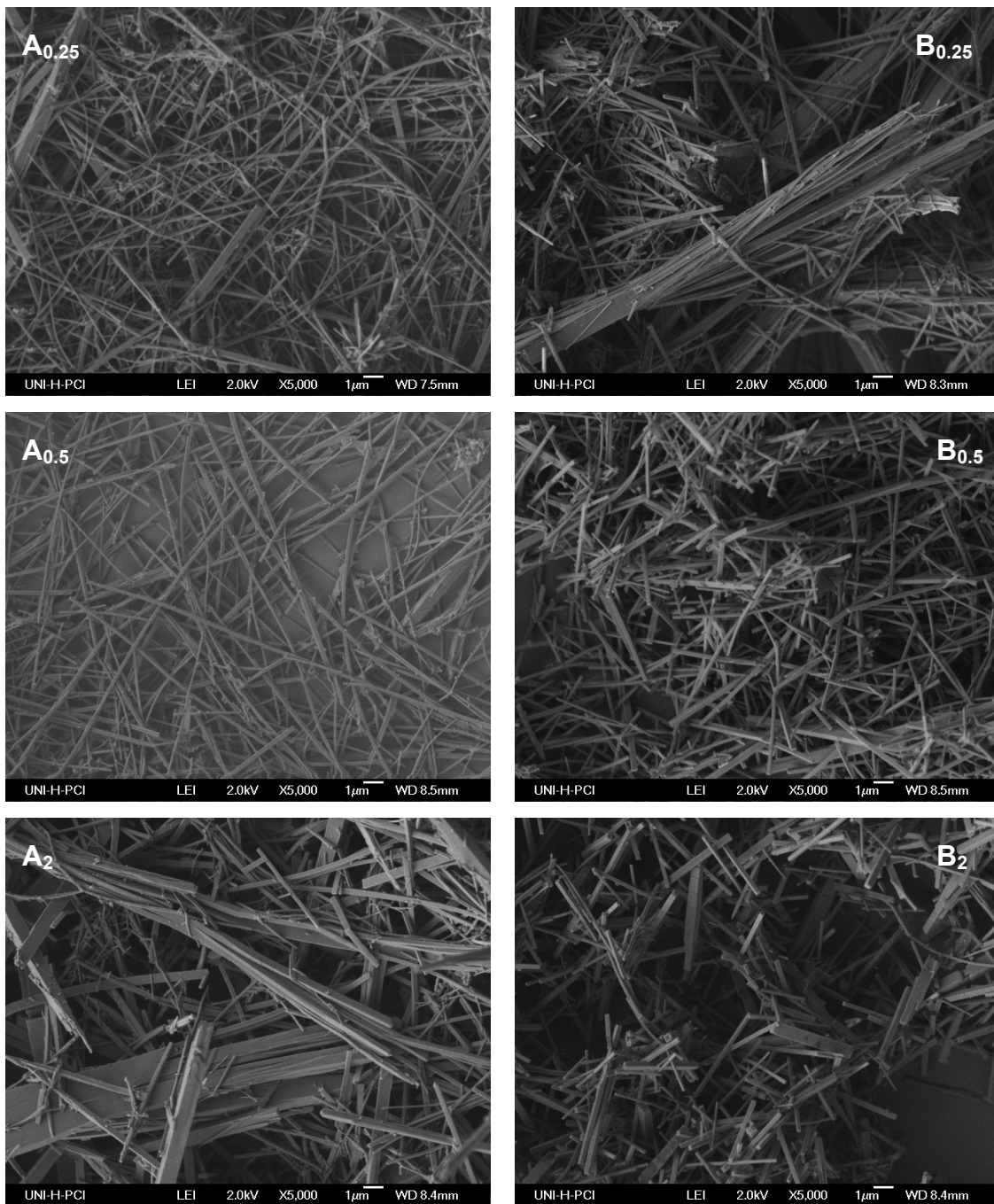


Figure 4.22 SEM images of the as-synthesized SiO₂ NTs. The samples in Group A were prepared with the rapid injection process, while those in Group B were prepared without that process. The subscripts indicate the correspondent adding rate of ethanol in the unit of milliliter per minute (mL/min).

Table 4.2 Influencing factors on the morphology of the product

Sample	Size distribution	Length	Tube bundles
A _{0.25}	50 - 400 nm	40 μm	some
A _{0.5}	100 - 200 nm	15 - 20 μm	Nearly zero
A ₂	100 - 500 nm	10 - 20 μm	many
B _{0.25}	50 - 400 nm	20 - 40 μm	many
B _{0.5}	100 - 200 nm	5 - 10 μm	Nearly zero
B ₂	100 - 500 nm, 1 – 2 μm	5 - 7 μm	Nearly zero

4.3.1.4 Discussion

a) The mechanism for the controlled growth of SiO₂ nanotubes

Also mentioned previously, the employment of capping agents in artificial 1D nanostructures is very popular and successful, as the case of silver nanowires by PVP [12, 13], and CdSe nanorods [34] and Co nanorods [35] by trioctyl phosphine oxide (TOPO). The supposed function of capping agents was to kinetically control the growth rate of various faces by interacting with these faces through adsorption and desorption [12, 13, 34, 35]. Although this hypothesis is still an empirical one, it worked well with experimental observations and was frequently used. In the present system, hydrolysed TEOS was used as a capping agent and succeeded not only in limiting the aggregation among intermediate NFs but also in promoting the anisotropic growth of Pt-containing SiO₂ NTs with high aspect ratios up to 400.

The shapeliness of the new product is obliged to the effective capping effect of TEOS. Upon the pre-adding, TEOS would undergo a rapid hydrolysis in the environment of ammonia solution, water and ethanol, producing a large amount of silanol monomers in a form of (RO)_{4-x}Si(OH)_x (x varies from 1 to 4). The silanol would be deprotonated at the basic condition and therefore mutually repulsive and relatively stable according to the DLVO theory [31]. However, the duration for the hydrolysis should be controlled on the one hand because at pH = 10 (20 °C) the condensation between silanol monomers is very fast and should be avoided to the best, on the other the double layer repulsion is greatly reduced with the presence of electrolyte, i.e. [Pt(NH₃)₄](HCO₃)₂.

When nuclei appear upon the injection of ethanol, the deprotonated silanol molecules (monomers or small polymers) are adsorbed to a larger extent than water and ethanol molecules (inferred from Lundelius's rule [15], which claimed that the extent of adsorption is usually higher from solvents in which the adsorptive is less soluble) on the specific facets of nuclei. The interactions between the silanol species and the nuclei were assumed to be electron donor-acceptor interaction (hydrogen bonding) and/or electrostatic force [1]. In this way, the aggregation of NFs, possibly due to the adsorptive layer of water molecules, is effectively prohibited.

With a suitable supply of building blocks by adding ethanol, the nuclei would grow in the single direction without or with little adsorptive layer of silanol molecules. The adsorptive layer of silanol is simultaneously growing along the same direction as the crystalline. In addition, there is also lateral growth, whereby the silanol layer is becoming thicker and thicker by further condensation of silanol on it. However, bearing in mind that these forces are short-range ones, the adsorptive force would decrease along the thickening process. Hence, the tube wall became irregular when too much TEOS was added [5]. Gradually, with the 1D growth on the one hand, and the lateral layer growth on the other, the final template-containing SiO₂ NTs are resulted.

To a certain extent, the capping effect of TEOS was comparable with its coating effect that has been very often employed to coat any pre-formed morphologies, but what has been demonstrated here was its "selective coating" in this particular system of 1D growth of the nanostructures. In the modified growth route, the two functions of TEOS were elegantly combined together to yield the shapely product. Compared with using conventional surfactants [12, 13, 34, 35], the ingenious employment of reactant itself (TEOS) as a capping agent in our method avoided the introduction of additional substances to the reaction system and thus simplified the cleaning procedure.

b) The reason for open-ended nanotubes

The open state of tube ends observed in Figure 4C-D could be explained based on the above-discussed capping mechanism. For silanol species it is difficult to deposit on the ends not only for the thermodynamic reason, for that the capping happened, but also for the kinetic barrier

since the corresponding facet is kept growing in a well-controlled manner and always active on deposition of building blocks. However, whether the hollow appearance of open-ended NTs comes from a loss of the templates is still not clear, since tubular template has also been observed as described in section 4.1.1.1. Nevertheless, the encouraging side of the matter is the free access of possible functional molecules into the inner part of the open NTs.

c) Rapid nucleation process

Based on the theory of LaMer and Dinegar [33], which has been described in section 2.2.5, a single particle size can be achieved if the nucleation happens in a single burst of nuclei, whereas a range of sizes results if new nuclei form during the growth period. This theory has been popularly and successfully applied to prepare monodispersed nanoparticles, e.g. CdSe [34], Co [35] nanocrystals.

For the controlled growth of SiO₂ NTs in our study, the extremely rapid nucleation process has succeeded in promoting the length of NTs, although it has no obvious influence on the distribution of NTs in diameter possibly due to the slower growing rates in comparison with the two cases mentioned above.

d) The morphology of the product during the controlled growth

In the following, the relationship between the three parameters of the morphology of the product and the influencing factors are discussed on the basis of controlled growth.

Length

It was concluded that the length of the NTs tends to increase with the decrease of the providing rate of building blocks, i.e. [Pt(NH₃)₄](HCO₃)₂. This conclusion is reasonable since a slowly providing of building blocks could avoid the formation of new nuclei and thus promote the anisotropic growth of crystalline fibers. Besides, the reason that the rapid nucleation is advantageous to the anisotropic growth is also the same.

Distribution in diameter

As demonstrated in section 4.3.1.3, the providing rate of building blocks is closely connected with the size distribution of the NTs. Here, the formation of bundles is not under consideration.

The theory of the focusing and defocusing processes [34], which were popularly suggested for the kinetic control of growth of monodisperse nanoparticles, is employed here to interpret the mechanism in combination with the capping effect.

When the providing rate is suitable so that the concentration of building blocks is higher than the solubilities of all the particles (nuclei) present, all particles grow, regardless of size. Amongst them, the smaller particles grow faster than the larger ones, and as a result, the size distribution is focused to be nearly monodisperse.

When the providing rate is very slow so that the concentration of building blocks drops below a critical threshold, the defocusing process occurs: the smaller particles are depleted and the larger ones grow. Thus the size distribution broadens.

For the two situations discussed above, TEOS monomers have acted as capping agents to avoid the aggregation and realise the kinetic control of size distribution. However, when the providing rate of building blocks is too fast, there is not enough time to allow the effective adsorption of capping agents on the new surface of particles after the deposition of building blocks. Therefore, aggregation among particles happens, leading to a broad size distribution.

Bundles

The flocculation of dispersions is a consequence of attractive forces holding particles together when they collide [35]. The formation of bundles of NTs could be regarded as the flocculation of dispersions of NTs. Besides, the fundamental reason for the formation of bundles of NTs should be attributed to the residual attractive forces, i.e. possibly also electrostatic forces and/or hydrogen bonding, among the template fibers of $[\text{Pt}(\text{NH}_3)_4](\text{HCO}_3)_2$ in spite of the shield of SiO_2 walls. The thinner the SiO_2 walls, the stronger the residual attractive forces. That is the reason for the observation of bundles with a fast adding rate of ethanol (**A**₂).

The chance for the formation of bundles is higher when the length increases, since longer fibers are easier to meet each other from the view of chances and more difficult to depart from each other due to the larger area in contact. Thus both cases with a slow adding rate of ethanol (**A**_{0.25} and **B**_{0.25}) contained bundles. Besides, the absence of bundles in sample **B**₂ could be explained from the view of the short length of NTs.

4.3.2 Controlled growth of TiO₂ nanotubes with high aspect ratios

The strategy for the controlled growth of SiO₂ NTs was also applied to the synthesis of TiO₂ NTs. However, due to the acute reaction of TBOT with moisture, the strategy has been modified: the TBOT ethanol solution was employed as both the precipitating agent and the capping agent. The as-synthesized sample was dropped on the SEM sample holder and then calcined at 500 °C for 5 h.

4.3.2.1 Morphology

The SEM images of the calcined sample were shown in Figure 4.23. First of all, the yield of TiO₂ NTs is not 100 %. In image A, besides two cross-linked NTs (one of them is mechanically broken at the cross point), some amount of 0D particles can also be observed. A 6- μ m-long NT with some particles decorated on part of its wall is shown in image B. From an open TiO₂ tube image C, it is learned that the NT owns a rectangular cross-section in not only its interior but also its exterior. The NT has a diameter of 90 - 100 nm and a tube thickness of ca. 20 - 30 nm. Actually NTs as thin as 40 nm has also been observed in image D. The bump on the tube wall should consist of TiO₂ nanoparticles. In addition, broken tubes are frequently observed as those in image D. The fragmentation of NTs could be due to the shrinkage of tube walls and simultaneously the strong connection between the tube and the sample holder.

4.3.2.2 Discussion

With respect to planned conductivity measurements, the new TiO₂ NTs (40 - 100 nm in diameter, up to 6 μ m in length) are much more applicable than the conventional ones (section 4.1.3, 300 - 400 nm in diameter and 3 - 4 μ m in length) since more effective contact could be realized between the electrode and thin NT below 100 nm in diameter.

By adding TBOT ethanol solution to precipitate the template fibers, the aspect ratios of the NTs have been greatly improved from the original 10 to the present 100, although at the same time the amount of by-products, i.e. nanoparticles, has also increased. The produce of nanoparticles should result from the acute hydrolysis and condensation of TBOT when it was exposed to the great amount of moisture in the aqueous solution of [Pt(NH₃)₄](HCO₃)₂.

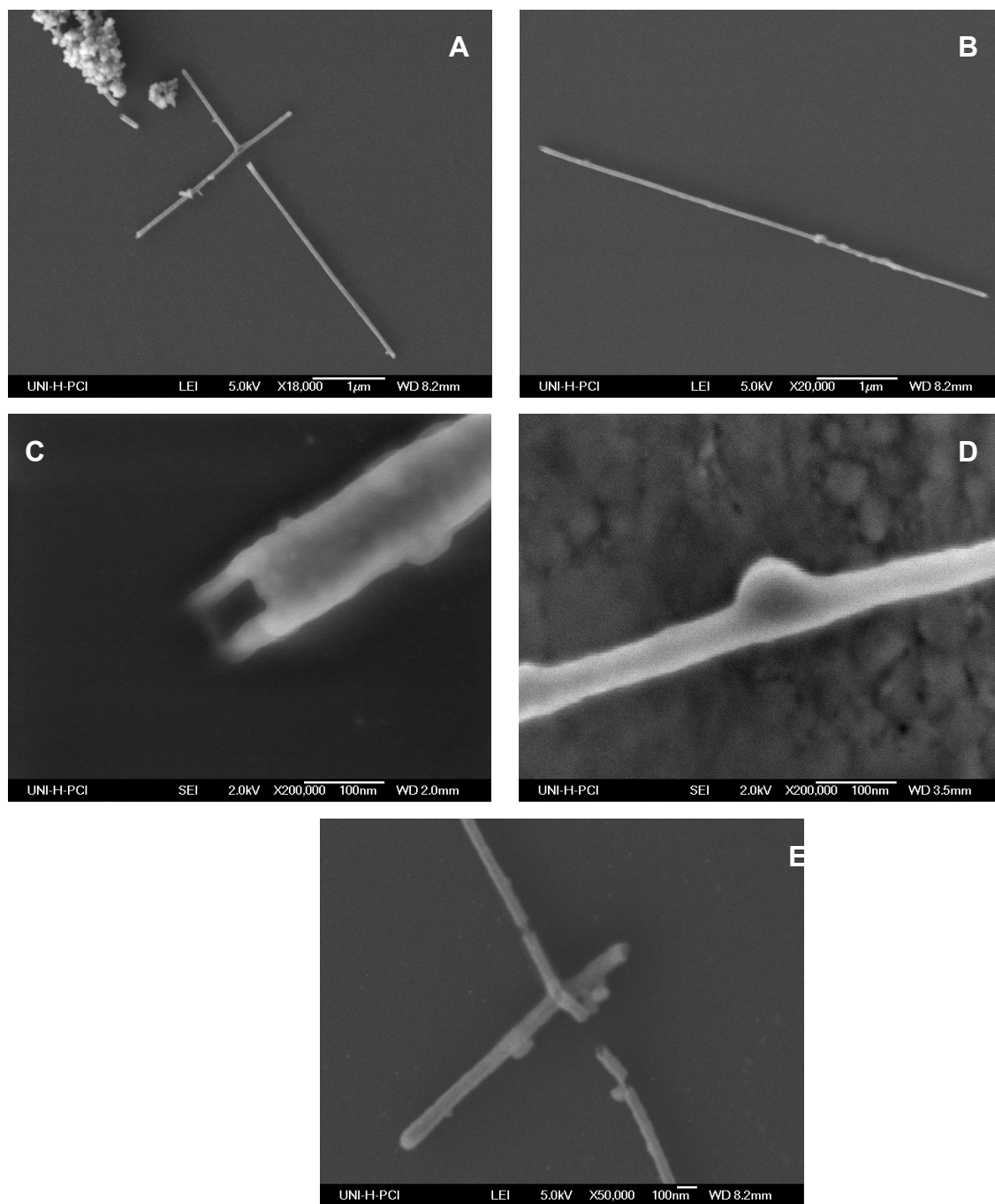


Figure 4.23 SEM images of the TiO₂ NTs prepared in the controlled route.

4.4 Summary

Based on the results, the following conclusions can be made about the synthesis of oxide NTs with the Pt templates.

- $[\text{Pt}(\text{NH}_3)_4](\text{HCO}_3)_2$ grows into rectangular prisms due to its anisotropic configuration. Surprising is that hollow crystals have also been formed as well as solid ones.
- In a general synthesis route of SiO_2 and TiO_2 NTs, the precipitates of rectangular prisms were employed as templates, which were coated with metal alkoxides in a sol-gel process. The interactions between the templates and tube walls, supposed to be hydrogen bonding and/or electrostatic forces, have been confirmed by the shift of the characteristic IR absorption peaks of amorphous SiO_2 . After the calcination, the Pt templates, which have been deformed to clusters, stayed to constitute the metal-containing oxide NTs.
- The SiO_2 NTs prepared in the general route possess a broad distribution from 50 nm to 2 μm in diameter, which has been inherited from that of the Pt templates. Most of tubes are close-ended. The filling state of SiO_2 NTs with the Pt metal clusters are not uniform due to the unequal states of different template fibers. Continuous Pt nanowires are also observed inside SiO_2 NTs with diameters below 50 nm.
- In comparison with SiO_2 NTs, the synthesis of TiO_2 NTs is much more difficult due to the rapid reaction of TBOT when exposed to moisture. The successful synthesis is dependent on the pH value, efficient cooling and addition of DEG as a stabilizer.
- The TiO_2 NTs prepared in the general route have a narrow size distribution, with 300 – 400 nm in diameter and 3 - 4 μm in length. Pt clusters are highly dispersed inside the TiO_2 walls and inhibited from crystallization due probably to the TiO_2 surface encapsulation layer and/or local charge transfer phenomena. The presence of Pt clusters in the tubes has in turn promoted the formation of rutile below 500 °C.
- The broadly distributed template fibers of the Pt salt are formed due to the aggregation of intermediate NFs, which cannot be prohibited effectively by varying the preparation parameters of the templates. By employing the pre-hydrolyzed TEOS, i.e. silanol species, as

capping agents, the aggregation of NFs has been effectively prohibited.

- Through a rapid nucleation and then a slow anisotropic growth, monodispersed (100 – 200 nm) SiO₂ NTs with high aspect ratios (100 - 400) have been prepared in a well-controlled manner. Another remarkable character of the new product is the open tube end.
- From the N₂ adsorption isotherm, there are micropores, mesopores and macropores inside the SiO₂ NTs after the calcination at 350 °C. The BET specific surface area of the mesopores is relatively large, being 116.4 m²/g. The pore size distribution range is 5 - 25 nm, centered at 12.2 nm.
- During the controlled synthesis, pre-hydrolyzed TEOS was employed both as a capping agent to stabilize the intermediate NFs from aggregation, and as a coating agent to form the tube walls. The capping mechanism of hydrolysed TEOS was supposed as the selective adsorption of silanol layers on specific surfaces of the nuclei. The observation of bundles of SiO₂ NTs with distinct borders has well visualized the capping effect.
- During the controlled growth of SiO₂ NTs, both the rapid nucleation and the providing rate of building blocks influence the morphology of the product.
- The controlled growth has also succeeded in preparing TiO₂ NTs with diameters of 40 – 100 nm and lengths of up to 6 μm. Because of the rapid rates of hydrolysis and condensation of TBOT, some amount of TiO₂ nanoparticles was produced inevitably.

5 Oxide nanotubes with templates of $\text{Co}(\text{NH}_3)_6](\text{HCO}_3)(\text{CO}_3)$

Hexamincobalt hydrocarbonate acts as a template for the synthesis of SiO_2 NTs as well. The nanotubes obtained appear to be uniform in diameter (100 - 200 nm) and possess a high aspect ratio (100 – 200) with optimised preparation parameters.

It is necessary to mention here that anisotropic growth is not a specific phenomenon for hydrocarbonate salts. Instead nanofibers have also been grown by employing $\text{Pt}(\text{NH}_3)_4\text{Cl}_2$ as the template salt (unshown results).

In this chapter, the formation of this type of Co-containing SiO_2 NTs is demonstrated. At first $[\text{Co}(\text{NH}_3)_6](\text{HCO}_3)(\text{CO}_3)\cdot 2\text{H}_2\text{O}$ has been prepared into template nanofibers. Then these NFs have been coated with silica walls. Various parameters influencing the preparation and thus the morphology of the template-filled NTs were discussed.

5.1 Preparation of $[\text{Co}(\text{NH}_3)_6](\text{HCO}_3)(\text{CO}_3)\cdot 2\text{H}_2\text{O}$ via ion-exchange

The commercial $[\text{Co}(\text{NH}_3)_6]\text{Cl}_3$ was converted into $[\text{Co}(\text{NH}_3)_6](\text{HCO}_3)(\text{CO}_3)\cdot 2\text{H}_2\text{O}$ via ion exchange. The solution of $[\text{Co}(\text{NH}_3)_6](\text{HCO}_3)(\text{CO}_3)\cdot 2\text{H}_2\text{O}$ has an orange color. The powdered product was obtained by adding a large amount of ethanol to precipitate the salt from its aqueous solution.

For the characterization of this powder sample, single crystal XRD and powder XRD were carried out.

5.1.1 Single crystal X-ray Diffraction

Since the preparation process is supposed to be a simple ion exchange without detectable redox reactions, a composition of the powder of roughly $[\text{Co}(\text{NH}_3)_6](\text{HCO}_3)_3$ plus an uncertain amount of crystal water was expected. For that compound no entry has been found in the Powder Diffraction File database and the single-crystal database.

Thus, a big crystal, which is suitable for the single-crystal XRD analysis, was selected from

the powdered product. Results show that the compound has a molecular formula is $[\text{Co}(\text{NH}_3)_6](\text{HCO}_3)(\text{CO}_3)\cdot 2\text{H}_2\text{O}$ with the molecule mass as 318.17. Its structure can be described by a unit cell showing the monoclinic symmetry (space group $C1\ 2/c\ 1$, No. 15). The unit cell parameters are: $a = 1.4847\ \text{nm}$, $b = 0.8751\ \text{nm}$, $c = 1.0063\ \text{nm}$ and $\alpha = \gamma = 90^\circ$, $\beta = 112.04^\circ$. The cell volume is $1.2119\ \text{nm}^3$. The (100), (010) and (001) projected structures of the unit cell of this crystal are shown in Figure 5.1. For clarity, H atoms are not shown. By comparing the three projections, we can learn that this Co salt is highly anisotropic.

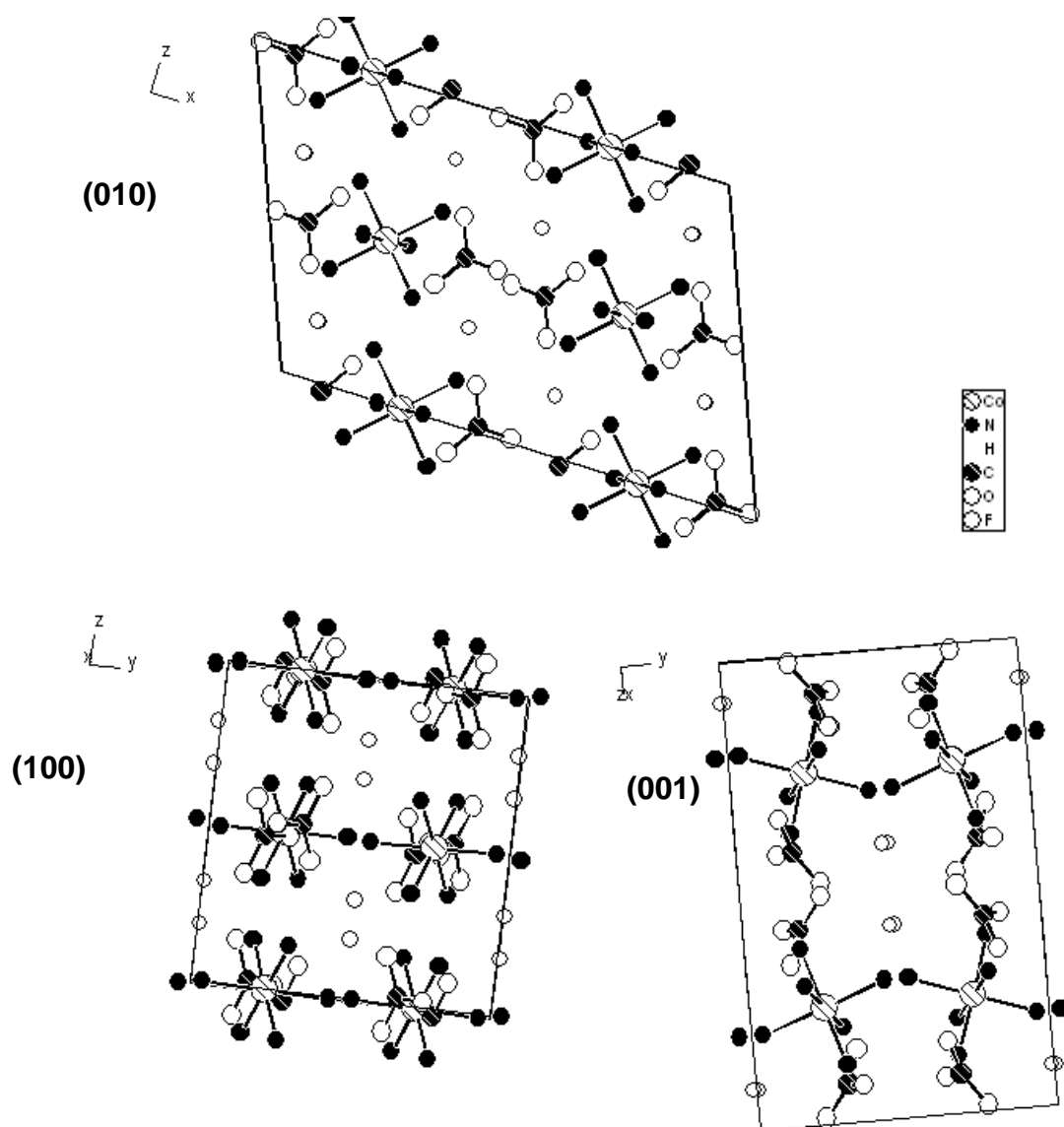


Figure 5.1 The (010), (100) and (001) projected structures of the unit cell of $[\text{Co}(\text{NH}_3)_6](\text{HCO}_3)(\text{CO}_3)\cdot 2\text{H}_2\text{O}$.

5.1.2 Powder X-ray Diffraction

In order to verify the purity of the powdered product, the experimental X-ray diffraction pattern (Figure 5.2B) was compared with a powder pattern (Figure 5.2A) calculated from the single-crystal data. The peak positions of the two patterns agree very well with each other, except that the weak peaks centred at 14.56° , 15.18° , 16.16° , 17.84° and 18.18° in pattern B are devoid in pattern A.

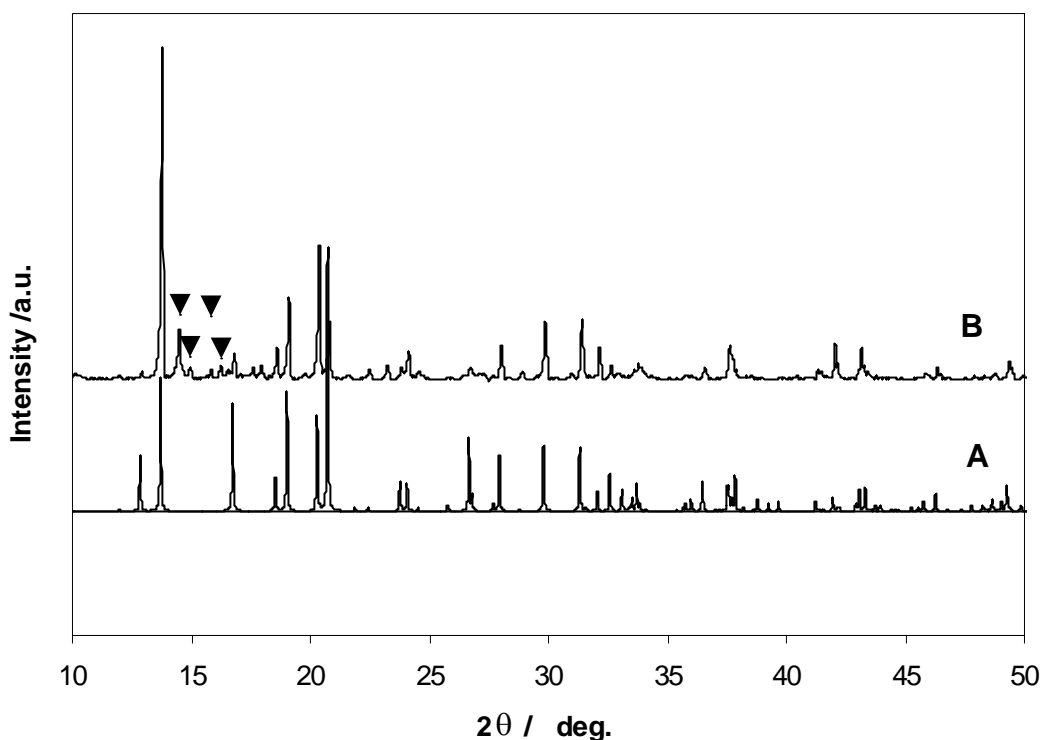


Figure 5.2 Powder diffraction patterns: (A) the calculated pattern from the single-crystal data and (B) the measured pattern of the powder product of $[\text{Co}(\text{NH}_3)_6](\text{HCO}_3)(\text{CO}_3)\cdot 2\text{H}_2\text{O}$ (the same as the Co templates).

Therefore, it could be concluded that the cobalt salt is composed of nearly only one phase, whose composition is $[\text{Co}(\text{NH}_3)_6](\text{HCO}_3)(\text{CO}_3)\cdot 2\text{H}_2\text{O}$. Concerning the slight discrepancy, a possible reason could be the presence of a trace amount of impurities in the powder product.

The impurities could be the presence of $[\text{Co}(\text{NH}_3)_6](\text{CO}_3)_{3/2}$ or $[\text{Co}(\text{NH}_3)_6](\text{HCO}_3)_3$ due to the instable state of HCO_3^- . However, as shown in the following sections, the presence of impurities would not disturb the formation of uniform nanofibers of the Co templates and in turn

the Co-filled SiO₂ NTs.

5.2 Co templates

5.2.1 Results

Adding ethanol into the aqueous solution of the [Co(NH₃)₆](HCO₃)(CO₃)·2H₂O resulted in precipitation. At a critical volume of ethanol, a fluffy orange precipitate formed. The suspension of the precipitate, i.e. Co templates, was deposited on the silicon substrate for SEM observation.

The behaviour of the Co templates (the same crystallinity as the [Co(NH₃)₆](HCO₃)(CO₃)·2H₂O) was rather different from that of the Pt templates. With the slow evaporation of the ethanol solvent, the originally formed orange precipitate disappeared as soon as it was exposed in air. That means it could not be distinguished with naked eyes from the silicon substrate anymore. Under SEM, there is consistently no observation of regular morphology of crystals.

Rapid evaporation of the ethanol from the precipitate suspension with a blow of dry air was effective to keep the original morphology of template. The template morphology of an optimised sample is shown in Figure 5.3.

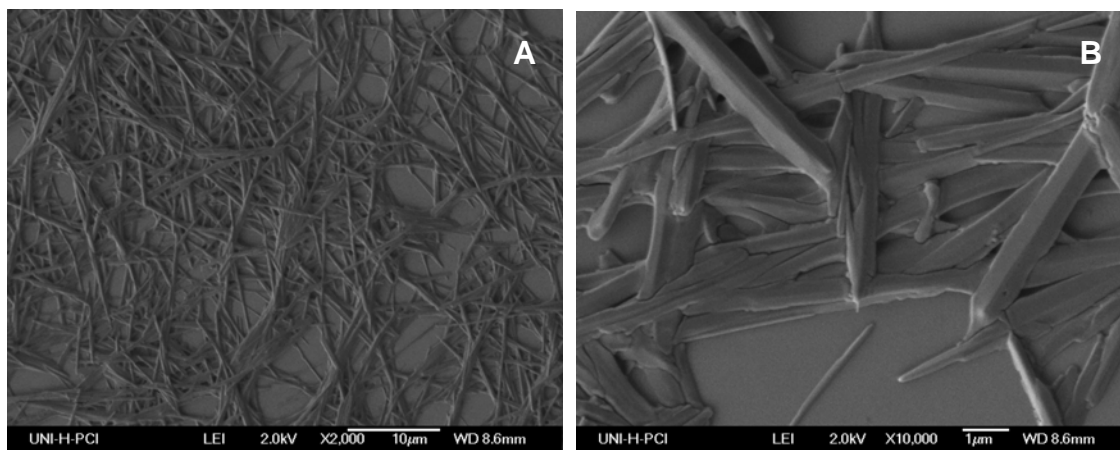


Figure 5.3 SEM images of the Co templates with optimised preparation parameters (0.0044 g [Co(NH₃)₆](HCO₃)(CO₃)·2H₂O in 2 ml ammonia (pH 10.64) is precipitated by 10 ml ethanol in 3 min).

As shown in Figure 5.3A, only one kind of a uniform fiberlike morphology is observed in the optimised sample. In a close-up (Figure 5.3B), firstly it is seen that the fibers consist of prismatic surfaces, a characteristic for ionic crystals. The lateral distribution can hardly be described because of the severe boundary deformation of individual fibers. Without clear separation between them, it looks like the fibers have fused with the others lying in their neighbourhood.

The appearance of the Co templates prepared by solvent modification is greatly dependent on the preparation parameters. The sample shown in Figure 5.4 was prepared with the same procedure except that distilled water was used instead of ammonia.

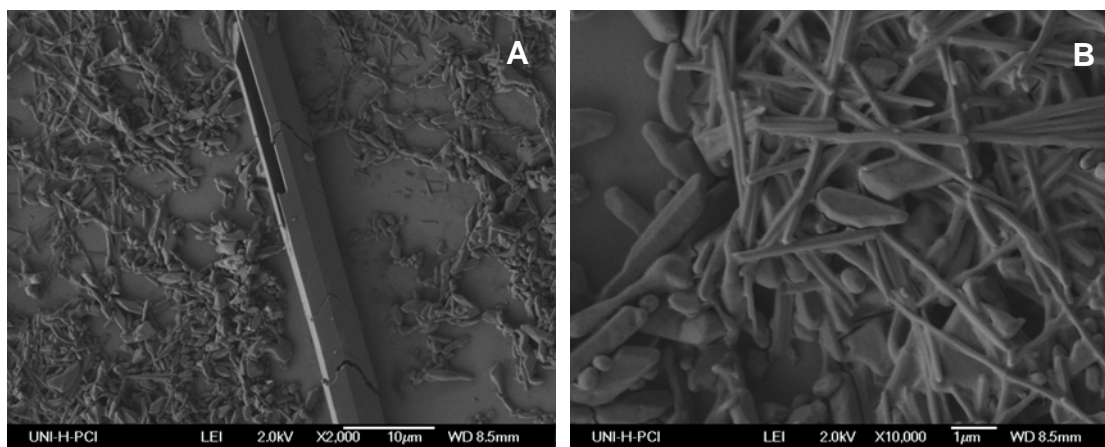


Figure 5.4 SEM images of the Co templates with the same preparation parameters as that in the optimised case except the change of pH value (0.0044 g $[\text{Co}(\text{NH}_3)_6](\text{HCO}_3)(\text{CO}_3)\cdot 2\text{H}_2\text{O}$ in 2 ml distilled water is precipitated by 10 ml ethanol in 3 min).

In Figure 5.4A it can be learned that this sample is devoid of uniformity in its morphology. There is an appearance of a 5- μm -thick and 50- μm -long crystal tube with a seemingly hexagonal symmetry. Besides, the particles in the nanometer regime seem to have no specific morphology, different from the fiberlike morphology in Figure 5.3A. At a high magnification in Figure 5.4B, the nanoparticles are composed of both 100-nanometer-thick fibers and equant rhombohedra with the shorter dimension in 500 - 800 nm approximately. Concerning the so-called equant rhombohedra particles, they have no specific size and morphology. Their formation could be attributed to either a spontaneous growth or possibly also the breaking of thick fibers upon the

exposure to air.

5.2.2 Discussion

Based on the experimental facts, it is learned that, firstly, $[\text{Co}(\text{NH}_3)_6](\text{HCO}_3)(\text{CO}_3)\cdot 2\text{H}_2\text{O}$ is only stable in solutions and would suffer a great deformation if exposed to air. One reason behind this phenomenon could be the stabilization function of ammonia and/or water molecules in the solvent to the high surface free energy of the template NFs. As soon as the compound is dried in air, the amine group in the Co salt was replaced by other ligands like OH^- or CO_3^- , thus leading to the deformation.

Secondly, the NFs in the optimised sample are uniform in diameter, the reason of that could be the geometric barriers among individual rhombic prisms, which prohibit them from aggregation and in turn avoid the broad size distribution as observed for the templates of $[\text{Pt}(\text{NH}_3)_4](\text{HCO}_3)_2$.

Thirdly, provided that the original morphology of the templates is kept until the observation under SEM, their appearance, including the size distribution and morphology, is highly dependent on the presence of ammonia in the mother solution. In fact, there are other influencing factors as will be discussed in section 5.4.

In general, in order to achieve uniformity in the final NTs, the preparation of the templates must be carefully controlled at the specific optimised conditions.

5.3 SiO_2 nanotubes with Co templates

An optimised sample of SiO_2 NTs with $[\text{Co}(\text{NH}_3)_6](\text{HCO}_3)(\text{CO}_3)\cdot 2\text{H}_2\text{O}$ nanofibers as templates is presented. The analytical tools involved are XRD, SEM, TEM, STEM and EDXS.

The preparation of this sample followed the general route of the template method as already described in Scheme 1.1 of Chapter 1. With the coating of TEOS, the original morphology of the templates is copied and transferred to the final SiO_2 NTs.

5.3.1 X-ray Diffraction

The crystallinity of the sample before and after the calcination was examined by XRD measurements.

Before the calcination, the sample is amorphous as shown in Figure 5.5B. The function of SiO_2 coating to the crystallinity of Co templates is more obvious when compare the pattern of pure Co templates (pattern A) with that of the sample (pattern B).

The disappearance of the diffraction peaks of Co templates after coated with SiO_2 walls is supposed to be due to the strong interactions between them. Inferred from the high surface free energy of the Co templates as discussed in section 5.2, the presence of SiO_2 walls must have stabilized the NFs by strong interaction forces between them. That may lead to the collapse of the crystalline Co templates inside the tubes, since the template NFs are rather thin, being 100 – 200 nm as will be observed under TEM for the inner diameters of tubes (section 5.3.2). Moreover, the shielding of SiO_2 walls might have stopped the aggregation of template NFs from each other, which would otherwise yield crystalline Co salt.

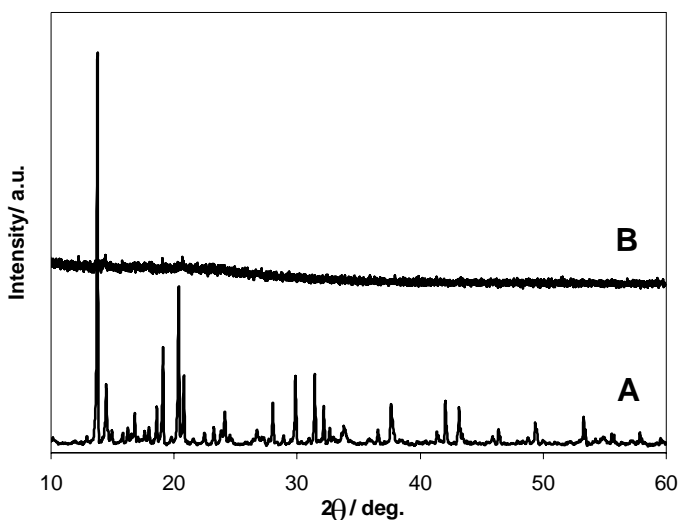


Figure 5.5 XRD patterns of (A) the Co templates exposed in air and (B) the template-filled SiO_2 NTs.

After the calcination, the sample shows different crystallinities at different heating atmospheres. If the sample is treated in air at 300 °C and 500 °C for 5 h respectively, its XRD patterns in Figure 5.6B and C show weak and broad peaks of Co_2SiO_4 (pattern A in Figure 5.6).

If the sample is treated in H_2 at 400 °C for 5 h, instead of those Co_2SiO_4 , its XRD pattern shown in Figure 5.7B appears the peaks of the hexagonal cobalt metal (Figure 5.7A). The weak and broad peaks in pattern B indicate that the sizes of the Co metal particles are in the low range of nanometers. According to Scherrer equation, the size distribution of Co particles is 7 – 15 nm. For potential applications based on magnetic properties, the calcination of the sample should be carried out in the reductive H_2 atmosphere.

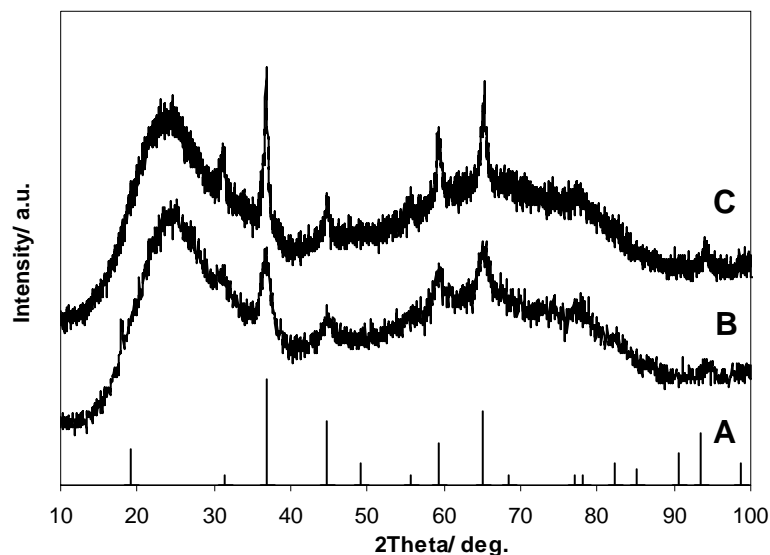


Figure 5.6 XRD patterns of (A) standard Co_2SiO_4 , (B) the template-filled SiO_2 NTs calcined in air at 300 °C for 5 h, and (C) calcined in air at 500 °C for 5 h.

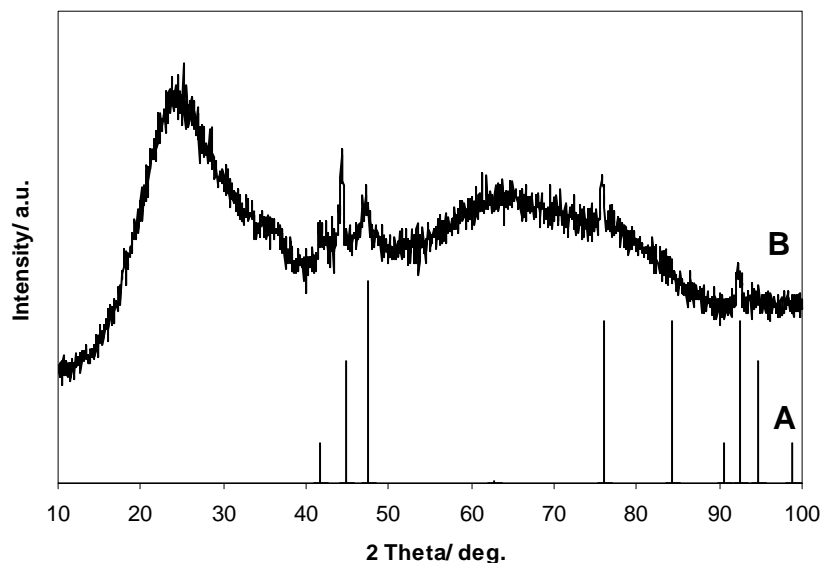


Figure 5.7 XRD patterns of (A) standard hexagonal Co and (B) the template-filled SiO₂ NTs calcined in H₂ at 400 °C for 5 h.

If one compares the XRD results in Figure 5.6 and 5.7, it is seen that for all samples calcined either in air or H₂, their XRD patterns all have a remarkably broad peak in the range of 20 - 30°, which is attributed to the amorphous SiO₂ [1]. Meanwhile the Co₂SiO₄ or metallic Co peaks are weak, especially when compared with the strong Pt peaks in the Pt-containing SiO₂ NTs (Figure 4.7C in section 4.1.2.2). The latter lacks the broad peak of amorphous SiO₂. Based on the previous analyses, it is concluded that the broad peak of amorphous SiO₂ could be covered by highly crystalline Pt particles. Instead, with the weak crystallinity of Co₂SiO₄ and metallic Co particles, the peak of amorphous SiO₂ would be detected unambiguously.

The weak crystallinity of Co₂SiO₄ and metallic Co particles should probably have nothing to do with the SiO₂ coating, but be closely related to their native properties, e.g. high lattice energies. In order to prove this assumption, pure Co salt was calcined at 500 °C for 5 h in air and the X-ray diffraction pattern of the resultant black powder is shown in Figure 5.8. The product is assigned to Co₃O₄. From the weak peaks in this pattern, it can be inferred that the phase transformation of the cobalt oxide from amorphous to crystalline during thermal treatment is also difficult to occur even in the absence of SiO₂.

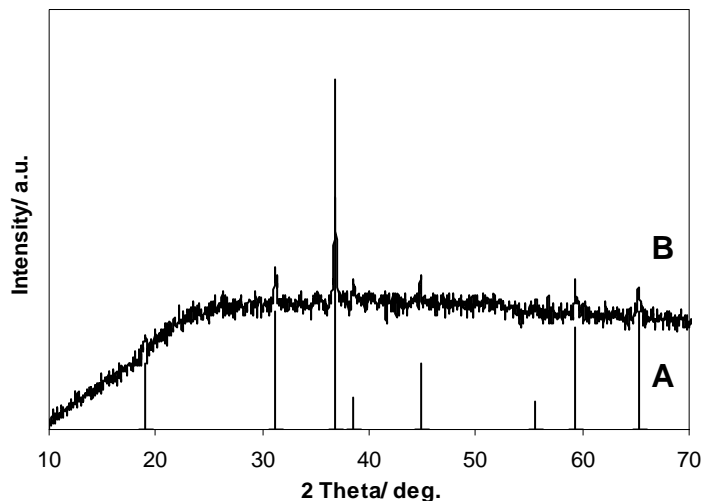


Figure 5.8 XRD patterns of (A) standard Co_3O_4 and (B) the product after $[\text{Co}(\text{NH}_3)_6]\text{HCO}_3\text{CO}_3 \cdot 2\text{H}_2\text{O}$ was calcined at $500\text{ }^\circ\text{C}$ for 5 h.

5.3.2 Electron Microscopy

5.3.2.1 Scanning Electron Microscopy

The topographical morphology of the sample is well observed by SEM (Figure 5.9). The sample was prepared for the SEM observation by dropping the suspension of the sample on the SEM sample holder directly after the sol-gel process.

As shown in Figure 5.9A, the sample contains 1D nanostructures with a narrow size distribution and lengths up to $20\text{ }\mu\text{m}$. The yield of the 1D nanostructures in this sample is very high, without detectable by-products. At a higher magnification (Figure 5.9B), it is seen that the fibers have smooth surfaces and closed ends, with diameters around $100\text{ - }200\text{ nm}$.

Being dried, the sample was collected and calcined at $400\text{ }^\circ\text{C}$ with a flow of H_2 for 5 h (flow rate: 6 L/h). The appearance of the obtained Co-containing SiO_2 NTs, as shown in Figure 5.9C and D, is in well accordance with the one before calcination. Due to the unavoidable mechanical abrasion during the sample handling, the tubular interior of some fibers can be observed through their broken cross-sections. Noteworthy, the morphology of their cross-sections is uniformly rhombohedral, different from the rectangular cross-sections of Pt-containing SiO_2 NTs in Chapter 4. Further details will be shown in the TEM image in Figure 5.10D.

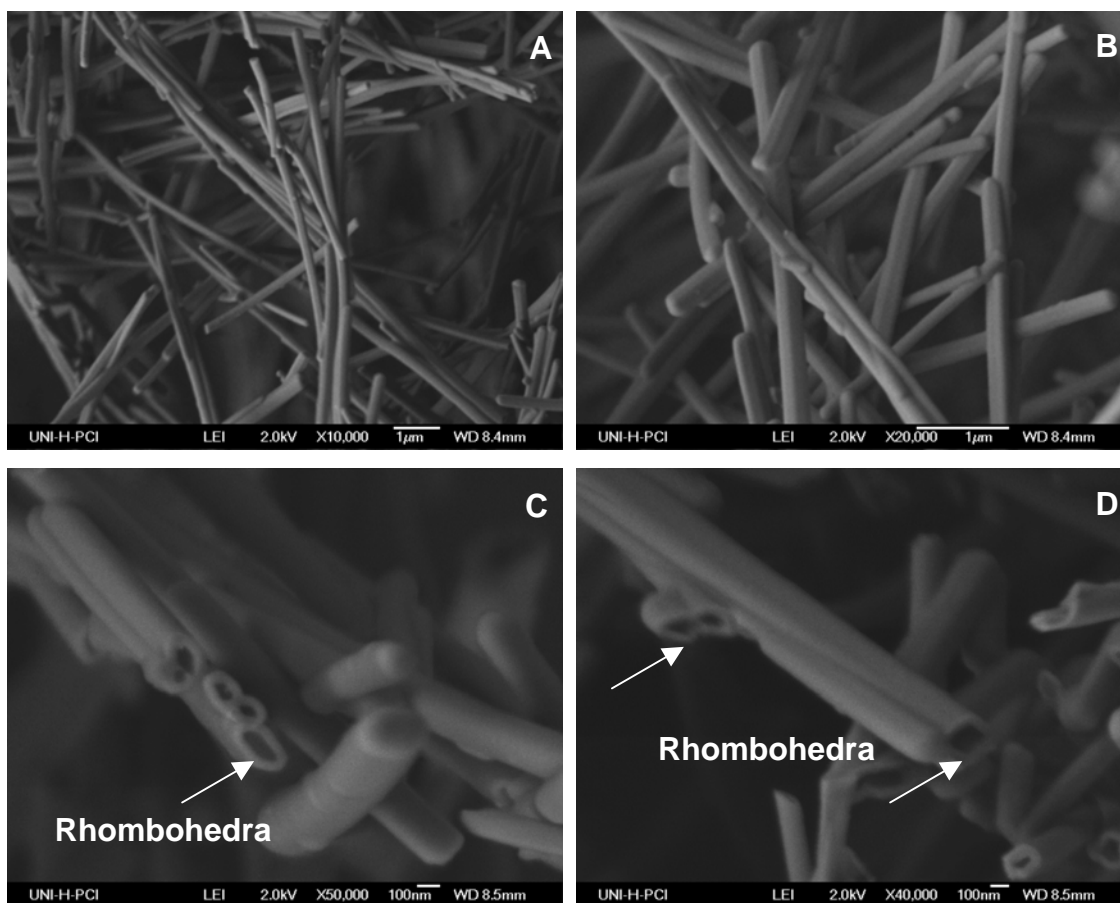


Figure 5.9 SEM images of an optimised sample. (A)(B) SiO₂ nanotubes filled with Co templates; (C)(D) the same sample calcined at 400 °C for 5 h in a blow of H₂.

5.3.2.2 Transmission Electron Microscopy

The tubular structures of the Co-containing SiO₂ NTs were observed with TEM. Co particles appear as black contrasts under the selected imaging conditions due to the high electron scattering potential of Co, whereas the regions containing SiO₂ are grey.

From the TEM images in Figure 5.10, both SiO₂ NTs filled with Co nanoparticles (image A and B) and empty SiO₂ NTs (image C) can be observed, while the latter has a much less chance to occur. The appearance of empty tubes could have two reasons: one is the escape of Co particles from the open ends of tubes, the other is based on the possible existence of the hollow template nanofibers of [Co(NH₃)₆](HCO₃)(CO₃)·2H₂O, which disperse highly into the porous SiO₂ walls, as inferred from the big hollow fiber in Figure 5.4A.

Interestingly, a single chain of Co nanoparticles is formed in the tube (inner diameter: ca. 50 nm) indicated with an arrow in Figure 5.10A. The component particles in the single chain are nearly uniform in size distribution. The formation of the single chain only occurs in tube whose inner diameter is below a certain value, i.e. roughly 100 nm, the reason is probably related to a relatively less amount of $[\text{Co}(\text{NH}_3)_6](\text{HCO}_3)(\text{CO}_3)\cdot 2\text{H}_2\text{O}$ in these thin tubes. In addition, the wall thickness of the tubes in the current sample is about 50 - 60 nm.

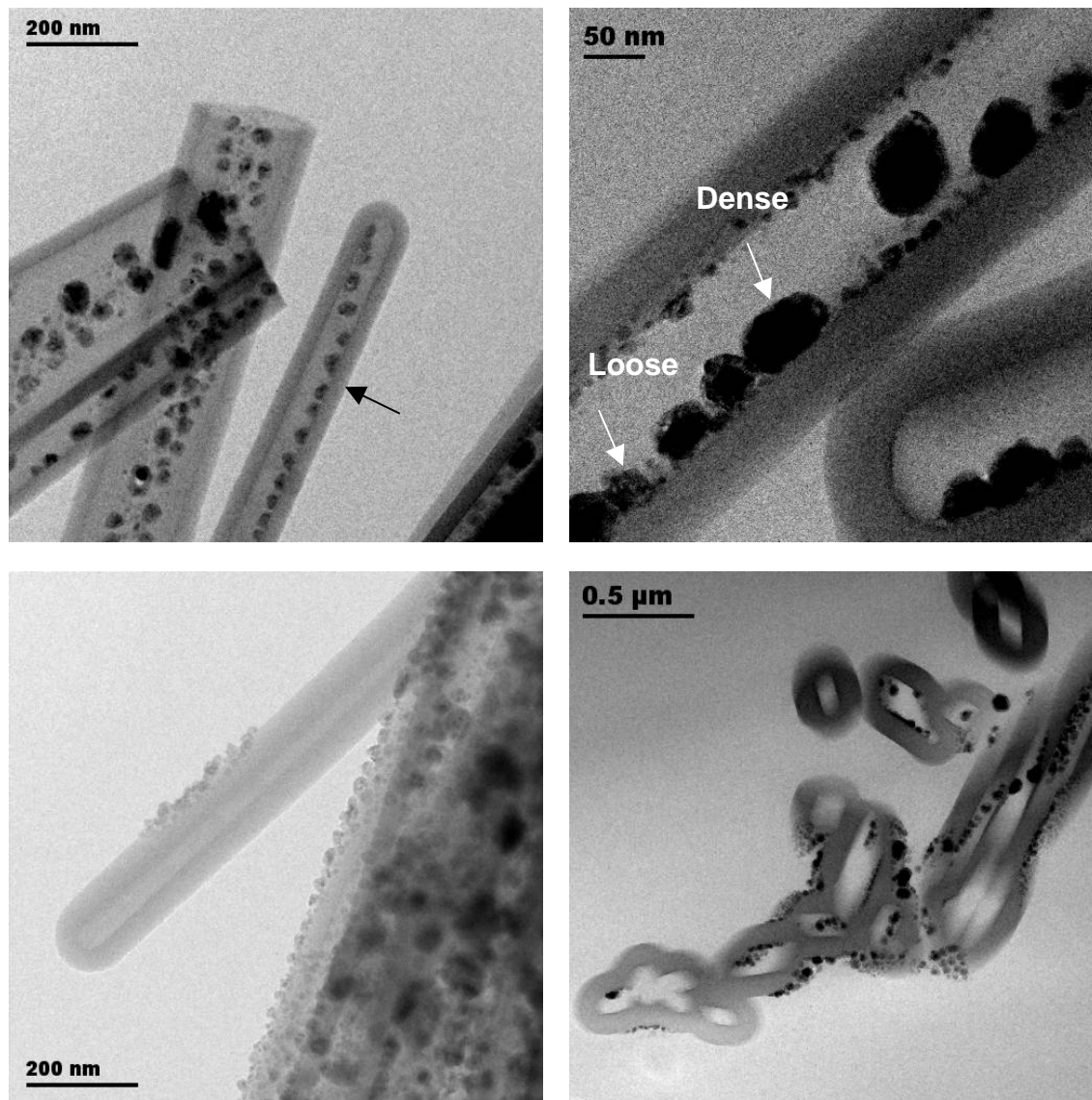


Figure 5.10 TEM images of optimised sample of Co-containing SiO_2 NTs: (A-C) the view along the tube axis; (D) the cross-sectional TEM image.

In Figure 5.10B, it is seen clearly that the size distribution of cobalt metal nanoparticles is very broad, ranging from several nm to ca. 60 nm. The calculated size from the powder XRD pattern (Figure 5.7B) is in the range of 7 - 15 nm. Apparently, the larger particles are beyond the application of the Scherrer equation. As to the larger particles, their densities could be very different. Some particles are rather dense as inferred from the equal black contrast throughout the whole area of the particles. In comparison, some particles are rather loose, having unequal contrasts throughout their whole area. Examples for both cases are indicated in the image. This phenomenon is reasonable since the big particles are grown by aggregation of small particles during the heat treatment. In addition, it could be envisaged that the separate and tiny particles would fuse into the big particles as time evolves or as temperature climbs.

In Figure 5.10C, besides the empty tube mentioned above, there is a certain amount of Co particles beyond the confinement of tubes, which could be attributed to the escape of Co from the open ends of tubes since there are a lot of tubes being left open as shown in Figure 5.10A. Another possibility is that very small Co nanoparticles diffuse through the porous SiO₂ walls and agglomerate into big particles outside the tubes.

From the cross-sectional image of the tubes in Figure 5.10D, the rhombohedral morphology is observed clearly, which confirms the SEM observations in Figure 5.9C and D. In addition, the black points, representing Co particles, appear both inside and outside the tubes.

5.3.2.3 Scanning Transmission Electron Microscopy and Electron Dispersive X-ray Spectroscopy

More information about the structure of Co-containing SiO₂ NTs is achieved with Scanning Transmission Electron Microscopy (STEM).

The STEM images are shown in Figure 5.11. In all images the area with white contrast indicates Co, while the grey area corresponds to amorphous Si.

In image A most of tubes are filled with a single chain of Co particles. In other words, the Co nanoparticles are aligned into 1D arrays inside SiO₂ NTs.

In image B several empty SiO₂ NTs are shown together with the filled NTs. There is a

distinct difference in contrast between the inner and outer wall of the empty tube indicated with arrows. The discrepancy in contrast could be attributed to the presence of very thin layer of small Co particles or even amorphous Co inside the inner wall of tube.

Image C and D were made at a higher magnification. From them, it is seen that the Co nanoparticles in the NTs are different in their sizes and shapes (image C). The crystalline particles are not totally arranged in a line (image D).

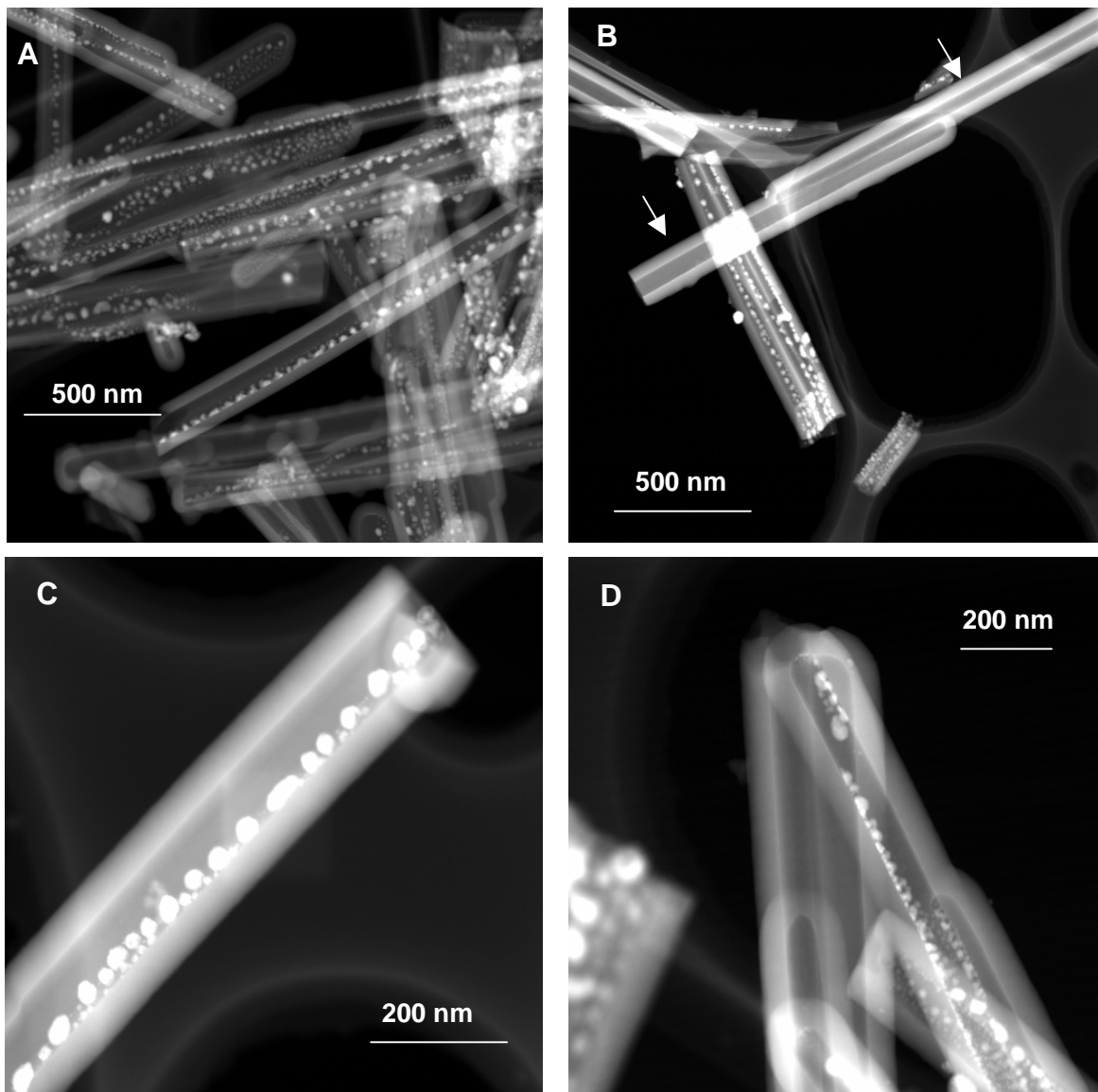


Figure 5.11 STEM dark-field images of the Co-containing SiO₂ NTs.

As shown in Figure 5.12, three points have been chosen on the STEM image for EDXS analyses. The point number one is a single big white particle outside the confinement of NTs. The number two and three are sitting on the inner part of a filled tube and an empty tube, respectively.

From the three EDX spectra, it is learned that the Co content decreases in the sequence of point number one, two and three, while the Si content increases. The point number one is actually a big Co particle attached on a SiO₂ tube. The point number two in the filled tube has reasonably Co inside. At the point number three, almost no cobalt has been detected, indicating that the tube is nearly empty.

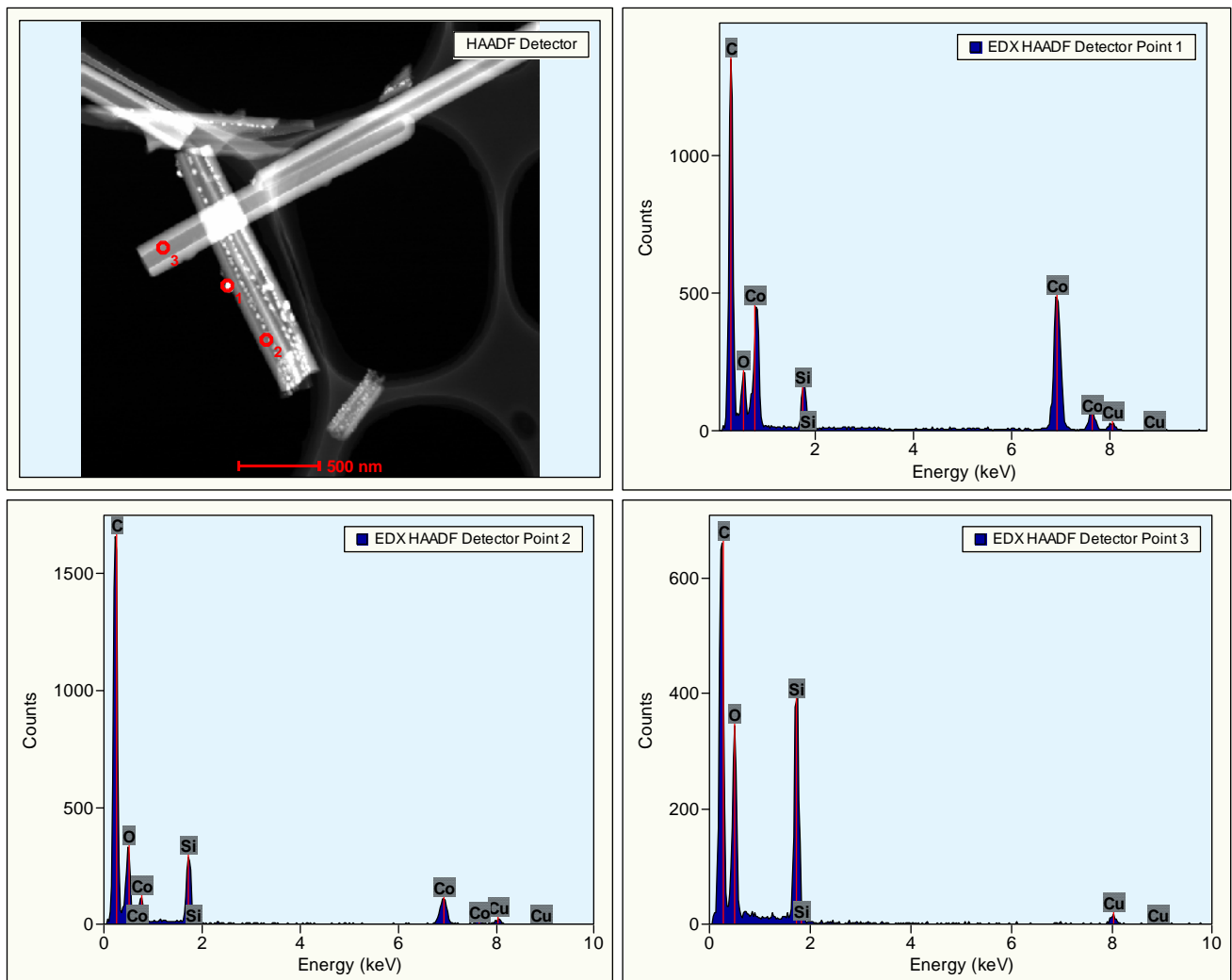


Figure 5.12 EDXS measurements of Co-containing SiO₂ NTs.

5.3.3 Thermogravimetric Analysis

Figure 5.13 (black line) shows TG, DTG and DTA curves of the sample of template-filled SiO₂ NTs. The pure [Co(NH₃)₆](HCO₃)(CO₃)·2H₂O is used as a reference (grey line).

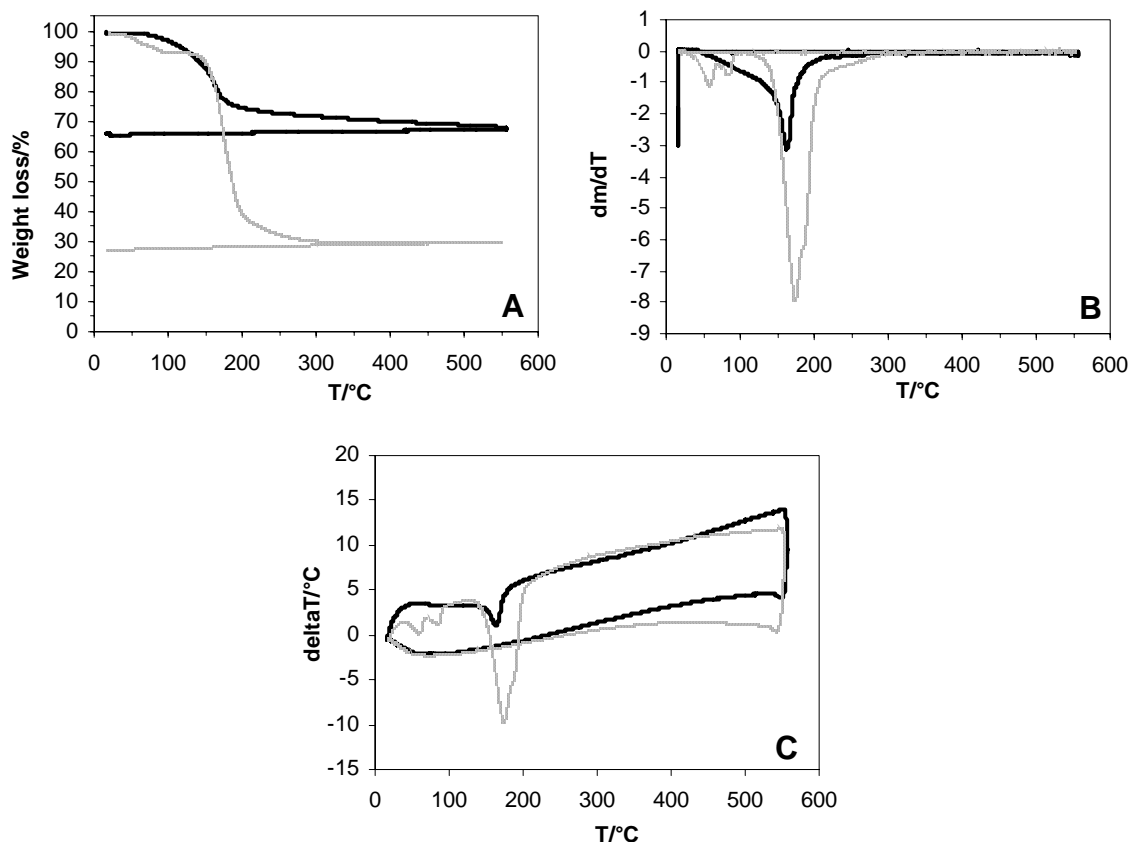


Figure 5.13 (A) TG curve, (B) DTG curve and (C) DTA curve of the template-filled SiO₂ NTs (black line) and the pure [Co(NH₃)₆](HCO₃)(CO₃)·2H₂O (grey line).

In Figure 5.13A, the weight loss of the sample is about 25%, corresponding to the decomposition of [Co(NH₃)₆](HCO₃)(CO₃)·2H₂O, the releasing of residual water or solvent molecules in the mesoporous SiO₂ wall, and also the dehydration of Si-OH groups. The latter two sources of weight loss become predominant above 300 °C. It is believed that there are still residual water or ethanol molecules in the mesoporous SiO₂ wall. From the DTG curve of the sample in Figure 5.13B, its weight loss is centered at 155 °C, 20 °C lower than the pure Co salt. This shift could be attributed to the size effect, similar to that of Pt templates discussed in section

4.1.2.3. The DTA curve of the sample in Figure 5.13C shows a broad endothermic peak ranging from 55 °C to 200 °C, which could be assigned to the decomposition of the Co salt. Thermal effects above 200 °C are not obvious. In comparison with the pure Co salt, the endothermic peak of the NT sample is weaker and also has a detectable shift to low temperature.

5.3.4 Infrared Spectroscopy

The IR spectra of the sample before and after the TG analysis are depicted as black line and grey line respectively in Figure 5.14. The three positions annotated with wavenumbers are characteristic absorption peaks for amorphous SiO₂. As also mentioned in section 4.1.2.3 of Chapter 4, the peaks near 1100, 800 and 450 cm⁻¹ are assigned to the asymmetric stretching of SiO₄ tetrahedron, the symmetric stretching of SiO₄ tetrahedron and the Si-O-Si bending respectively [2]. Similar to the case of the Pt templates (up to 44 cm⁻¹) discussed in section 4.1.2.3, the SiO₂ absorption peaks of the SiO₂ NTs filled with Co templates have a significant shift (up to 57 cm⁻¹) to lower energies in comparison with that of the Co₂SiO₄-containing SiO₂ NTs. The interaction between the Co template and the SiO₂ tube wall, as deduced from the bigger red shift, is stronger than the case of Pt.

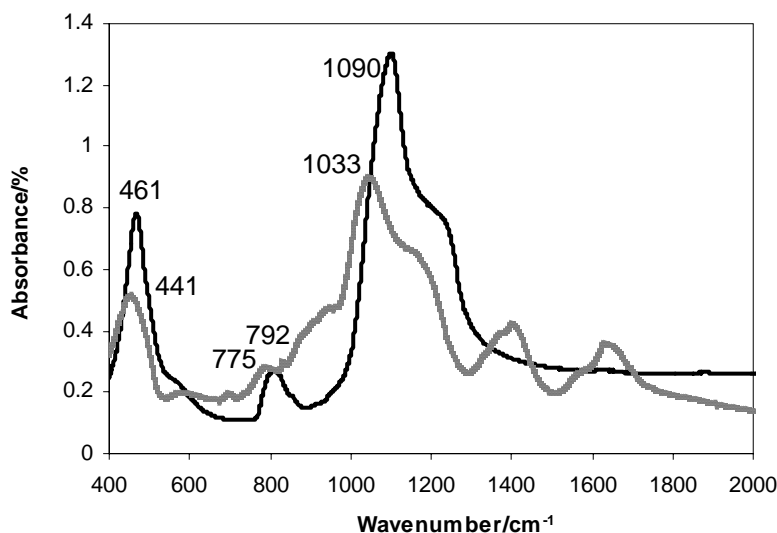


Figure 5.14 IR spectra of the sample before (grey line) and after (black line) the TG analysis.

5.4 Influences of various parameters on the morphology

The optimized sample of Co-containing SiO₂ NTs exhibited in section 5.3 appears uniform in diameter and high in aspect ratio. It is proven by experiments that parameters, such as the concentration of [Co(NH₃)₆](HCO₃)(CO₃)·2H₂O in the mother solution (including the aminocobalt compound and ammonia solution), the pH value of ammonia solution and the rate of ethanol addition, have significant effects on the morphology of the final product. Details are discussed below.

5.4.1 Results

According to the preparation methods described in section 3.1.2.3, samples A1 - A6, were synthesized to study the influences of various parameters on the product morphology. Table 5.1 gives details of preparation parameters and descriptions of morphologies for samples A1 – A6. The SEM images of the six samples are shown in Figure 5.15. TEOS was used for all the samples.

Table 5.1 Parameters of preparation and product descriptions

Sample name	Concentration of Co salt in mother solution g/mL	pH of ammonia solution 20 °C	Rate of ethanol addition mL/min	Results		
				Needle diameter, nm	Particle	Amorphous materials
A1	0.0011	10.64	1.67	200 - 700	Many	No
A2	0.0022	10.64	1.67	150 - 200	No	No
A3	0.0088	10.64	1.67	100 – 900	No	Many
A4	0.0022	10.00	1.67	< 100	No	Some
A5	0.0022	11.06	1.67	100 - 300	Some	No
A6	0.0022	10.64	0.67	100 - 500	Many	No

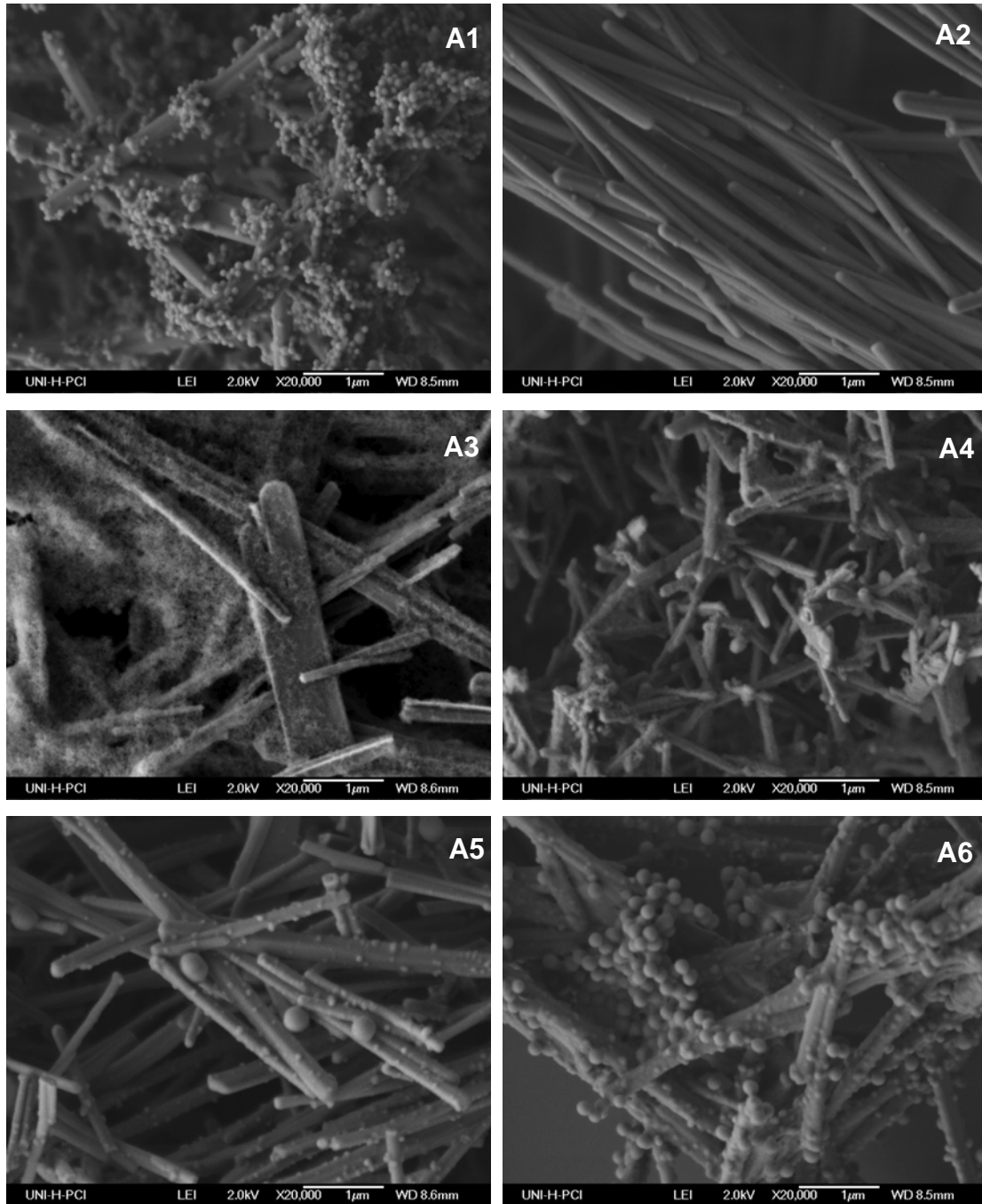


Figure 5.15 SEM images of a series of samples with different parameters of preparation. Detailed parameters of sample A1 – A6 are listed in Table 5.1.

Sample A2 is the best sample, which was prepared with optimized parameters. In the SEM image of this sample, only 1D nanostructures with uniform diameter (150 – 200 nm) are observed in a parallel alignment into several- μm -thick bundles.

In comparison, the other five samples contain one or two kinds of impurities beside the 1D nanostructures. The 1D nanostructures in these samples are broadly distributed in diameter, from which the influences of preparation parameters on the morphology of the template NFs are reflected. The impurities, including nanoparticles and amorphous materials, should be related to the unsuccessful coating of TEOS on the template NFs. Hence the influences of the three parameters on the form of product can be deduced from their influences on the size distribution of needles and the coating of TEOS.

5.4.2 Discussion

For sample A1, A2 and A3, the concentration of $[\text{Co}(\text{NH}_3)_6]\text{HCO}_3\text{CO}_3 \cdot 2\text{H}_2\text{O}$ in the mother solution increases in sequence by reducing the volume of ammonia solution. According to Figure 5.15 and Table 5.1, the needles exhibit broader size distributions in A1 and A3 than A2. As to the coating of TEOS, nanoparticles are resulted in A1 while amorphous materials are found in A3. Since the limited amount of ammonia solution in A3 would lead to a decrease in pH value of the TEOS/ethanol/water system, the hydrolysis and condensation of TEOS at the low pH value might cause the formation of the amorphous material. The case of A1 is exactly opposite to that of A3, leading to the formation of particles.

From sample A4, A2 and A5, the pH values of the mother solution increased in sequence by employing different ammonia solutions while other parameters were constant. It is observed in SEM that the needles grow both in larger diameters and lengths with the increasing pH, while the size distribution has not significantly broadened. Simultaneously, the amorphous materials in the sample A4 and the particles in the sample A5 indicate the importance of controlling the pH value control for a successful coating of TEOS on the template NFs.

From sample A2 to A6, the rate of ethanol addition decreased. It was equivalent to a decrease of the growth rate of template NFs. All other parameters were same for these two

samples. Comparing their SEM images in Figure 5.15, a great amount of particles appear in sample A6, which could not be attributed to the increase of pH value like the cases of the sample A1 and A5. A reason could be some subtle changes especially on the surface of the template NFs during the slow precipitation for preparation of the sample A6, which lead to a weakening of the interactions between the templates and TEOS. Thus SiO₂ particles are formed instead of SiO₂ coating on the template NFs. In addition, the rate of ethanol addition could be changed between 1.25 to 3.33 mL/min without producing observable impurities while all other parameters were kept same as sample A2.

Based on the results and discussions, it is concluded that the synthesis of SiO₂ NTs with the Co templates is more sensitive to the parameters of preparation than the case of Pt templates. In order to prepare pure SiO₂ NTs with a uniform size distribution, optimised conditions must be precisely controlled as that of sample A2, i.e. concentration of the Co salt in the mother solution being 0.0022 g/mL, ammonia solution with pH 10.64 and rate of ethanol addition being 1.67 mL/min. In addition, careful adjustments must be taken for a scale-up of this optimised synthesis.

5.5 Summary

Based on the results, the following conclusions can be made about the synthesis of SiO₂ NTs with the Co templates.

- The homemade Co salt, i.e. [Co(NH₃)₆](HCO₃)(CO₃)·2H₂O as confirmed by single crystal XRD analysis, is highly anisotropic and has a habit to grow into nanoprisms by the solvent modification under appropriate conditions.
- Through at first the formation of template NFs of Co salt by solvent modification and then coating of TEOS, template-filled SiO₂ NTs were obtained. Under optimised conditions, shapely SiO₂ NTs with uniform diameters (100 – 200 nm) and high aspect ratios (100 – 200) are formed.
- The sample of template-filled SiO₂ NTs was calcined at different atmospheres. When it is treated in air, the Co salt reacted with SiO₂, leading to Co₂SiO₄. When it is treated in H₂, the

Co salt was reduced to metallic cobalt.

- The cross-sections of the Co-containing NTs are rhombohedral, instead of being rectangular like the Pt-containing SiO₂ and TiO₂ NTs.
- The wall thickness of the NTs is about 50 – 60 nm. Both hollow and filled SiO₂ NTs are present in one sample. Co nanoparticles are arranged into single chains in NTs with inner diameters less than 100 nm.
- The interactions between the Co templates and the SiO₂ walls in the template-filled SiO₂ NTs are testified by the red shift of IR absorption peaks of amorphous SiO₂ compared with the Co-containing SiO₂ NTs.
- The synthesis of SiO₂ NTs with Co templates is very sensitive to the parameters of preparation, including the concentration of mother solution, pH value of the ammonia solution and the rate of adding ethanol. The optimised conditions must be exactly followed in order to obtain pure Co-containing SiO₂ NTs without by-products.

6 Conclusions and outlook

In this work, the formation of oxide NTs with inorganic salt nanofibers as templates has been extensively explored in following aspects:

Both $[\text{Pt}(\text{NH}_3)_4](\text{HCO}_3)_2$ and $[\text{Co}(\text{NH}_3)_6](\text{HCO}_3)(\text{CO}_3)\cdot 2\text{H}_2\text{O}$ grow into 1D nanofibers during the process of solvent modification, which can be successfully coated with metal alkoxides in a sol-gel process. The interactions between the templates and tube walls, supposed to be hydrogen bonding and/or electrostatic forces, have been confirmed by shifts of SiO_2 IR absorption peaks for both cases of Co and Pt.

The Pt-containing SiO_2 NTs have been prepared in the general route of this template method, i.e. at first the formation of $[\text{Pt}(\text{NH}_3)_4](\text{HCO}_3)_2$ nanofibers and the subsequent coating and calcination processes. The Pt particles formed during the calcination at $500\text{ }^\circ\text{C}$ are dispersed within the tube and inside the tube wall. Continuous Pt nanowires are observed inside SiO_2 NTs with diameters below 50 nm. The formation of the template fibers of $[\text{Pt}(\text{NH}_3)_4](\text{HCO}_3)_2$ follows steps as the nucleation, anisotropic growth, aggregation of intermediate NFs and aging. By employing TEOS as a capping agent, the aggregation of NFs have been effectively prohibited. Uniform (100 - 200 nm) and ultralong (up to 40 μm) SiO_2 NTs were achieved in a kinetically controlled growth route.

The synthesis of TiO_2 NTs (300 – 400 nm in diameter) in a high yield has been realized with the general route of this template method. The high dispersion of Pt clusters inside the TiO_2 walls, when calcined at $500\text{ }^\circ\text{C}$, is possibly due to a TiO_2 surface encapsulation layer and/or local charge transfer phenomena. With the presence of Pt clusters inside the TiO_2 wall, the amorphous TiO_2 crystallized into rutile at a much lower temperature without the formation of anatase. By adjusting the synthesis route, TiO_2 NTs with diameter below 100 nm and length above 6 μm have been obtained, which might be better contacted with electrodes for electronic conductivity measurement.

Uniform SiO_2 NTs filled with Co nanoparticles were obtained in a high yield with

nanofibers of $[\text{Co}(\text{NH}_3)_6](\text{HCO}_3)(\text{CO}_3)\cdot 2\text{H}_2\text{O}$ as templates. The cross-sections of the Co-containing NTs are rhombohedral, instead of being rectangular as the Pt-containing oxide NTs. Co nanoparticles are arranged into single chains in NTs with inner diameters less than 100 nm.

In general, the oxide NTs prepared with this template method are in the range of 50 – 200 nm in the width dimension and up to 40 μm in length. Another remarkable point is the high metal filling content inside the tube, which is achieved together with the tube formation. The metal filling renders this kind of oxide NTs potential applications in catalysis and nanoelectronics.

It is apparent that two steps are determinative for the feasibility of this template method: the formation of the NFs and the successful coating of the wall material. To further investigate the mechanism of this template method, efforts should be given to: (i) looking for other inorganic species which grow into NFs by solvent modification. This behaviour is closely related to the anisotropy of crystalline materials. Two compounds with the same metal complex species but different types of anions would have different habits of morphology. Hence, knowledge about crystal structures and morphologies gathered in this study could make up the vacancy left in the field of Crystal Chemistry. (ii) Exploring the coating mechanism of oxide on a solid surface by sol-gel chemistry. As established in this thesis, the hydrogen bonding and/or electrostatic forces between the template NFs and the silanol monomers are supposed to be crucial for the effective coating. Both the exterior influencing factors on the coating, such as pH value, solvent, temperature, and interior factors, including the chemical constitutions of the template and coating agent, should be studied extensively. This would contribute to practical applications closely related to the solution-phase coating process.

Furthermore, efforts should be made to the alignment of NTs. Since either Pt or Co nanoparticles are containing in the oxide NTs, it is possible to employ electric or magnetic field to realize the alignment.

A special property of this kind of metal-filled oxide nanotubes is the extra high content of dispersed metal particles. This may find potential applications in catalysis.

References

Chapter 1

- [1] S. Iijima, *Nature* **1991**, 354, 56.
- [2] S. Iijima, *Nature* **1993**, 363, 603.
- [3] D. S. Bethune, C. H. Kiang, M. S. De Vries, G. Gorman, R. Savoy, J. Vazques, R. Beyers, *Nature* **1993**, 363, 605.
- [4] J. Kong, N. R. Franklin, C. Zhou, M. G. Chapline, S. Peng, K. Cho, H. Dai, *Science* **2000**, 287, 622.
- [5] P. G. Collins, K. Bradley, M. Ishigami, A. Zettl, *Science* **2000**, 287, 1801.
- [6] A.G. Rinzler, J.H. Hafner, P. Nikolaev, L. Lou, S.G. Kim, D. Tomanek, P. Nordlander, D.T. Colbert, R.E. Smalley, *Science* 1995, 269, 1550.
- [7] W.A. de Heer, A. Chatelain, D. Ugarte, *Science* **1995**, 270, 1179.
- [8] Q.H. Wang, A.A. Setlur, J.M. Lauerhaas, J.Y. Dai, E.W. Seelig, R.P.H. Chang, *Appl. Phys. Lett.* **1998**, 72, 2912.
- [9] H.J. Dai, J.H. Hafner, A.G. Rinzler, D.T. Colbert, R.E. Smalley, *Nature* **1996**, 384, 147.
- [10] M.H. Devoret, H.J. Dai, A. Thess, R.E. Smalley, L.J. Gerlings, *Nature* **1997**, 386, 474.
- [11] M.M.J. Treacy, T.W. Ebbeson, J.M. Gibson, *Nature* **1996**, 381, 678.
- [12] Y. Sun, B.T. Mayers, Y. Xia, *Nano Lett.* **2002**, 2, 481.
- [13] B.T. Mayers, Y. Xia, *Adv. Mater.* 2002, 14, 279.
- [14] J.Q. Hu, Y. Bando, D. Golberg, Q.L. Liu, *Angew. Chem. Int. Ed.*, 2003, 42, 3493.
- [15] Y. Feldman, E. Wasserman, D. Srolovitz R. Tenne, *Science* **1995**, 267, 222.
- [16] G.R. Patzke, F. Krumeich, R. Nesper, *Angew. Chem. Int. Ed.* **2002**, 41, 2446.
- [17] S.L. Soled, E. Iglesia, R.A. Fiato, J.E. Baumgartner, H. Vroman, S. Miseo, *Topics in Catalysts* **2003**, 26, 101.
- [18] E. Iglesia, S.L. Soled, R.A. Fiato, *J. Cata.* 1992, 137, 212.
- [19] B.G. Johnson, C.H. Bartholomew, D.W. Goodman, *J. Cata.* **1991**, 128, 231.

- [20] S. Sun, K. Fujimoto, Y. Zhang, N. Tsubaki, *Cata. Comm.* **2003**, 4, 361.
- [21] M. Quobosheae, S. Santra, P. Zhang, W. Tan, *Analyst* **2001**, 126, 1274.
- [22] M. Zhang, E. Ciocan, Y. Bando, K. Wada, L.L. Cheng, P. Pirouz, *Appl. Phys. Lett.* **2002**, 80, 491.
- [23] M. Harada, M. Adachi, *Adv. Mater.* **2000**, 12, 839.
- [24] J.E. Meegan, A. Aggeli, N. Boden, R. Brydson, A.P. Brown, L. Carrick, A.R. Brough, A. Hussain, R.J. Ansell, *Adv. Funct. Mater.* **2004**, 14, 31.
- [25] Y. Sun, B. Gates, B. Mayers, Y. Xia, *Nano Lett.* **2002**, 12, 165.
- [26] Y. Yin, Y. Lu, Y. Sun, Y. Xia, *Nano Lett.* **2002**, 2, 427.
- [27] J. Zygmunt, F. Krumeich, R. Nesper, *Adv. Mater.* **2003**, 15, 1538.
- [28] C.R. Martin, *Science* **1994**, 266, 1961.
- [29] M. Zhang, Y. Bando, K. Wada, *J. Mater. Res.* **2000**, 15, 387.
- [30] K.I. Hadjiivanov, D.G. Klissurski, *Chem. Soc. Rev.* 1996, 25, 61.
- [31] A.P. Alivisatos, *Science* **1996**, 271, 933.
- [32] H. Weller, *Adv. Mater.* **1993**, 5, 88.
- [33] M. Schiavello, Ed. *Photocatalysis and Environment*; Kluwer Academic Publishers: Dordrecht, The Netherlands, **1988**.
- [34] D.F. Ollis, H. Al-Ekabi, Eds. *Photocatalytic Purification of Water and Air*; Elsevier: Amsterdam, **1993**.
- [35] A.L. Linsebigler, G. Lu, J.T. Yates, *Chem. Rev.* **1995**, 95, 735.
- [36] B.O. Regan, M. Gratzel, *Nature*, **1991**, 353, 737.
- [37] A.M. Azad, S.A. Akbar, S.G. Mhaisalkar, L.D. Birkefeld, and K.S. Goto, *J. Electrochem. Soc.* **1992**, 139, 3690.
- [38] S.U.M. Khan, T. Sultana, *Solar Energy Mater. Solar Cells*, **2003**, 76, 211.
- [39] D. Gong, C.A. Grimes, O.K. Varghese, W. Hu, R.S. Singh, Z. Chen, E.C. Dickey, *J. Mater. Res.* **2001**, 16, 3331.
- [40] O.K. Varghese, D. Gong, M. Paulose, K.G. Ong, E.C. Dickey, C.A. Grimes, *Adv. Mater.* **2003**, 15, 624 .

- [41] H. Imai, Y. Takei, K. Shimizu, M. Matsuda, H. Hirahima, *J. Mater. Chem.* **1999**, 9, 2971.
- [42] M. Zhang, Y. Bando, K. Wada, *J. Mater. Sci. Lett.* **2001**, 20, 167.
- [43] S.M. Liu, L.M. Gan, L.H. Liu, W.D. Zhang, H.C. Zeng, *Chem. Mater.* **2002**, 14, 1391.
- [44] P. Hoyer, *Langmuir* **1996**, 12, 1411.
- [45] J.H. Jung, H. Kobazashi, K.J.C. Van Bommel, S. Shinkai, T. Shimizu, *Chem. Mater.* **2002**, 14, 1445.
- [46] R.A. Caruso, J.H. Schattka, A. Greiner, *Adv. Mater.* **2001**, 13, 1577.
- [47] T. Kasuga, M. Hiramutsu, A. Hoson, T. Sekino, K. Niihara, *Adv. Mater.* **1999**, 11, 1307.
- [48] G.H. Du, Q. Chen, R.C. Che, Z.Y. Yuan, and L.M. Peng, *Appl. Phys. Lett.* **2001**, 79, 3702.
- [49] Y.Q. Wang, G.Q. Hu, X.F. Duan, H.L. Sun, Q.K. Xue, *Chem. Phys. Lett.* **2002**, 365, 427.
- [50] G. Grubert, J. Rathousky, G. Schulz-Ekloff, M. Wark, A. Zukal, *Microp. Mesop. Mater.* **1998**, 22, 225.
- [51] D. Ugarte, T. Stöckli, J.M. Bonard, A. Châtelain, W.A. de Heer, *Appl. Phys.* **1998**, A67, 101.
- [52] E. Dujardin, T.W. Ebbesen, H. Hiura, K. Tanigaki, *Science* **1994**, 265, 1850.
- [53] Y. Saito, K. Nishikubo, K. Kawabata, T. Matsumoto, *J. Appl. Phys.* **1996**, 80, 3062.
- [54] Y. B. Li, Y. Bando, D. Golberg, Z.W. Liu, *Appl. Phys. Lett.* **2003**, 83, 999.
- [55] C. Hippe, M. Wark, E. Lork, G. Schulz-Ekloff, *Microp. Mesop. Mater.* **1999**, 31, 235.
- [56] M. Wark, C. Hippe, G. Schulz-Ekloff, *Stud. Surf. Sci. Catal.* **2000**, 129, 475.
- [57] L. Ren, U. Melville, M. Wark, *Frontiers of Solid State Chemistry, Proceedings of the International Symposium on Solid State Chemistry*, World Scientific Publishing, Co. Ltd., Singapore, **2002**, 441.
- [58] J. Zygmunt, F. Krumeich, H.-J. Muhr, R. Nesper, L. Ren, M. Wark, *Z. Anorg. Allg. Chem.*, **2002**, 628, 2189.
- [59] E. Dias, A. T. Davies, M. D. Mantle, D. Roy, L. F. Gladden, *Chem. Eng. Sci.* **2003**, 58, 621.
- [60] S. Kim, W. Choi, *J. Phys. Chem. B* **2002**, 106, 13311.
- [61] D.W. Bahnemann, J. Mönig, R. Chapman, *J. Phys. Chem.* **1987**, 91, 3782.

- [62] V. Subramanian, E. Wolf, P.V. Kamat, *J. Phys. Chem. B* **2001**, 105, 11439.
- [63] J. Lee, H. Park, W. Choi, *Environ. Sci. Technol.* **2002**, 36, 5462.
- [64] F. Krumeich, M. Wark, L. Ren, H.-J. Muhr, R. Nesper, *Z. Anorg. Allg. Chem.* **2004**, 630, 1054-1058.
- [65] T. Miyao, T. Saika, Y. Saito, S. Naito, *J. Mater. Sci. Lett.* **2003**, 22, 543.

Chapter 2

- [1] W. Borchardt-Ott, *Crystallography*, second edition, Springer, **1993**.
- [2] I.V. Markov, *Crystal Growth for Beginners*, World Scientific, Singapore, **2003**.
- [3] R. Tleimat-Manzalji, T. Manzalji, G. M. Pajonk, *J. Non-Cryst. Solids* **1992**, 147 & 148, 744
- [4] J. Fricke, *J. Non-Cryst. Solids* **1992**, 147 & 148, 356.
- [5] C.J. Brinker, G.W. Scherer, *Sol-gel Science: The Physics and Chemistry of Sol-Gel Processing*, Academic Press, inc., New York, **1990**.
- [6] R.T. Morrison, R.N. Boyd, *Organic Chemistry*, Allyn & Bacon, Boston, **1966**.
- [7] S. Ross, I. D. Morrison, *Colloidal Systems and Interfaces*, John Wiley & Sons, Inc., **1988**.
- [8] L.H. Allen, E. Matijević, *J. Colloid and Interface Sci.* **1969**, 31, 287.
- [9] W. Stöber, A. Fink, and E. Bohn, *J. Colloid and Interface Sci.* **1968**, 26, 62.
- [10] V.K. LaMer, R. H. Dinegar, *J. Am. Chem. Soc.* **1950**, 72, 4847.
- [11] J. Livage, M. Henry, C. Sanchez, *Progress in Solid State Chemistry* **1988**, 18, 259.
- [12] G. Winter, *Oil and Colour Chemist's Association*, **1953**, 34, 30.
- [13] M.F. Bechtold, R.D. Vest, L. Plambeck, *J. Am. Chem. Soc.* **1968**, 90, 4590.
- [14] B.J. Ingebrethsen, E. Matijevic, *J. Colloid Interface Sci.* **1984**, 100, 1.
- [15] D.C. Bradley, R.C. Mehrotra, D.P. Gaur, *Metal Alkoxides*, Academic Press, London, **1978**.

Chapter 3

- [1] Elton N. Kaufmann, *Characterization of Materials*, John Wiley & Sons, Inc., New Jersey, **2003**.

- [2] Z. L. Wang, Y. Liu, Z. Zhang, Handbook of Nanophase and Nanostructured Materials, Volume II : Characterization, Kluwer Academic/Plenum Publishers, New York, **2003**.
- [3] H.P. Klug, L.E. Alexander, X-ray diffraction procedures for polycrystalline and amorphous materials, 2nd Edn, John Wiley & Sons Inc., New York, **1974**.
- [4] C. Baerlocher, L.B. McCusker, Advanced Zeolite Science and Applications, Studies in Surface Science and Catalysis, Vol. 85, 391, Elsevier Science, **1994**.
- [5] S.J. Gregg, K.S.W. Sing, Adsorption, Surface Area and Porosity, Second Edition, Academic Press, **1982**.
- [5] K.S.W. Sing, D.H. Everett, R.A.W. Haul, L. Moscou, R.A. Pierotti, J. Rouquerol, and T. Siemieniewska, Pure Appl. Chem. **1985**, 57, 603.
- [6] A. Zsigmondy, Z. Anorg. Chem. **1911**, 71, 356.
- [7] S. Brunauer, P.H. Emmett and E. Teller, J. Amer. Chem. Soc. **1938**, 60, 309.
- [8] B.C. Lippens and J.H. de Boer, J. Catalysis **1965**, 4, 319.
- [9] B.C. Lippens, B.G. Linsen and J.H. de Boer, J. Catalysis **1964**, 3, 32.
- [10] M. Kruk and M. Jaroniec, Surfaces of Nanoparticles and Porous Materials, Surfactant Science Series, Marcel Dekker, Inc. **1999**, Volume 78, 443.
- [11] A. Sayari, P. Liu, M. Kruk, and M. Jaroniec, Chem. Mater. **1997**, 9, 2499.
- [12] M. Jaroniec and K. Kaneko, Langmuir **1997**, 13, 6589.
- [13] M. Kruk, M. Jaroniec, R. K. Gilpin, and Y. W. Zhou, Langmuir **1997**, 13, 545.

Chapter 4

- [1] C. Hippe, Untersuchung von strukturdirigierenden Einflüssen im Sol-Gel-Prozeß, Shaker Verlag, PhD thesis, University of Bremen, **1999**.
- [2] G. Attolini, C. Paorici, P. Ramasamy, J. Cryst. Growth **1986**, 78, 181.
- [3] G.C. Krueger, C.W. Miller, J. Chem. Phys. **1953**, 21, 2018.
- [4] I. V. Markov, Crystal Growth for Beginners, World Scientific, Singapore, **2003**.
- [5] C. Hippe, M. Wark, E. Lork, G. Schulz-Ekloff, Microp. Mesop. Mater. **1999**, 31, 235.

- [6] M. Wark, C. Hippe, G. Schulz-Ekloff, *Stud. Surf. Sci. Catal.* **2000**, 129, 475.
- [7] F. Krumeich, M. Wark, L. Ren, H.-J. Muhr, R. Nesper, *Z. Anorg. Allg. Chem.*, **2004**, 630, 1054-1058.
- [8] C. Suryanarayana and M. Grant Norton, *X-Ray Diffraction: A Practical Approach*, **1998**, Plenum Press, New York.
- [9] J. Zygmunt, F. Krumeich, R. Nesper, *Adv. Mater.* **2003**, 15, 1538.
- [10] R.B. Laughlin, J.D. Joannopoulos, *Physical Review B*, **1977**, 16, 2942
- [11] M.F. Bechtold, R.D. Vest and L. Plambeck, *J. Am. Chem. Soc.* **1968**, 90, 4590.
- [12] Y. Sun, B. Gates, B. Mayers, Y. Xia, *Nano Lett.* **2002**, 12, 165.
- [13] Y. Yin, Y. Lu, Y. Sun, Y. Xia, *Nano Lett.* **2002**, 2, 427.
- [14] J.E. Meegan, A. Aggeli, N. Boden, R. Brydson, A.P. Brown, L. Carrick, A.R. Brough, A. Hussain, R.J. Ansell, *Adv. Funct. Mater.* **2004**, 14, 31.
- [15] S. Ross, I. D. Morrison, *Colloidal Systems and Interfaces*, John Wiley & Sons, Inc., **1988**.
- [16] R.C. Mehrotra, PhD Thesis, London University **1952**.
- [17] D.M. Puri, PhD Thesis, University of Gorakhpur **1962**.
- [18] X. Jiang, T. Herricks, and Y. Xia, *Adv. Mater.* **2003**, 15, 1205.
- [19] J. Livage, M. Henry, and C. Sanchez, *Progress in Solid State Chemistry*, **1988**, 18, 259.
- [20] T. Ohsaka, S. Yamaoka and O. Shimomura, *Solid State Commun.* **1979**, 30, 345.
- [21] T. Mitsuhashi and O.J. Klippa, *J. Amer. Ceram. Soc.* **1979**, 62, 356.
- [22] Y. Zhang, A. Reller, *Chem. Comm.* **2002**, 606.
- [23] G.L. Haller, D.E. Resasco, *Adv. Catal.* **1989**, 36, 173.
- [24] D. R. Jennison, O. Dulub, W. Hebenstreit, U. Diebold, *Surf. Sci.* **2001**, 492, L677
- [25] S. Fischer, K.-D. Schierbaum and W. Gopel. *Sensors and Actuators* **1996**, B31, 13.
- [26] C.-M. Wang, A. Heller, H. Gerischer, *J. Am. Chem. Soc.* **1992**, 114, 5230.
- [27] S. Kim, W. Choi, *J. Phys. Chem. B*, **2002**, 106, 13311.
- [28] D.W. Bahnemann, J. Mönig, R. Chapman, *J. Phys. Chem.* **1987**, 91, 3782.
- [29] J. Lee, H. Park, W. Choi, *Environ. Sci. Technol.* **2002**, 36, 5462.
- [30] W. Noll, *Z. Anorg. Chem.* **1950**, 261, 1.

- [31] C.J. Brinker, G.W. Scherer, Sol-gel Science: The Physics and Chemistry of Sol-gel Processing, **1990**, 240.
- [32] W. Stöber, A. Fink, E. Bohn, J. Colloid Interface Sci., **1968**, 26, 62.
- [33] V.K. LaMer, R.H. Dinegar, J. Colloid Interface Sci., **1980**, 76, 418.
- [34] X. Peng, L. Manna, W. Yang, J. Wickham, E. Scher, A. Kadavanich, A. P. Alivisatos, Nature **2000**, 404, 59.
- [35] V.F. Puentes, K.M. Krishnan, A.P. Alivisatos, Science **2001**, 291, 2115.

Chapter 5

- [1] C. Suryanarayana and M. Grant Norton, X-Ray Diffraction: A Practical Approach, **1998**, Plenum Press, New York.
- [2] R.B. Laughlin, J.D. Joannopoulos, Physical Review B, **1977**, 16, 2942